

ABSTRACT

Title of Document: FRACTURE BEHAVIOR AND THERMAL CONDUCTIVITY OF POLYCRYSTALLINE GRAPHENE

Andrew Fox, Doctor of Philosophy, 2014

Directed By: Associate Professor Teng Li, Department of Mechanical Engineering

This dissertation investigates the effect of grain boundaries (GBs) in polycrystalline graphene on the tensile fracture behavior and thermal conductivity of the graphene sheets. Current techniques to fabricate large-scale graphene intrinsically introduce defects, e.g., GBs, resulting in polycrystalline graphene sheets. Though GBs in graphene are expected to affect the mechanical properties of graphene, mechanistic understanding and quantitative determination of such effects are far from mature. For example, existing studies on the effect of GBs on the tensile behavior of graphene only focus on a twin GB perpendicular to the tensile loading direction. However, GBs in a polycrystalline graphene sheet under uniaxial tension could be subject to tension in any arbitrary directions, depending on the GB and grain orientation in the graphene sheet. In this dissertation, we focus on the effect of GBs on the tensile and thermal response of polycrystalline graphene. The fracture process of polycrystalline graphene sheets under uniaxial tension was studied using molecular dynamics (MD) simulations to determine how GBs affects the ultimate strength and critical failure strain of the graphene. We also study the flow of heat through polycrystalline graphene to determine the effect of GBs on the thermal conductivity of graphene. A comprehensive study including 24 GB misorientation angles ranging from

2.1° to 54.3° and the whole range of loading angle (i.e., that between a GB and in-plane tensile loading direction, ranging from 0° to 90°) was carried out to quantitatively determine the effect of GBs. Stress-strain data were generated from the MD simulations and the failure strength and critical strain were analyzed. A theoretical model combining continuum mechanics theory and disclination dipole theory was introduced to predict the failure strength of the polycrystalline graphene sheets, which was shown to be in good agreement with the MD simulation results. Various failure modes of polycrystalline graphene under tension were also analyzed. The thermal conductivity of polycrystalline graphene as a function of GB misorientation angle and thermal loading angle was also quantitatively determined through systematic simulations. The quantitative findings from this dissertation could potentially bridge the knowledge gap toward a better understanding of defects and their effects on two-dimensional materials, and also shed light on possible defect control and engineering to achieve desirable properties of graphene in applications.

FRACTURE BEHAVIOR AND THERMAL CONDUCTIVITY OF
POLYCRYSTALLINE GRAPHENE

By

Andrew Fox

Dissertation submitted to the Faculty of the Graduate School of the
University of Maryland, College Park, in partial fulfillment
of the requirements for the degree of
Doctor of Philosophy
2014

Advisory Committee:
Associate Professor Teng Li, Chair
Professor Hugh Bruck
Associate Professor Peter Chung
Professor William Fourney
Professor Yunfeng Zhang, Dean's Representative

© Copyright by
Andrew O. Fox
2014

Dedication

This dissertation is dedicated to my mother and father who have supported me throughout my education. Without their love and support this document would not have been possible.

Acknowledgements

I would like to thank Professor Teng Li who was my advisor at the University of Maryland for the past four years. I have learned many valuable insights from attending two of his classes and discussions in our group meetings and consider it to be a benefit for having spent this time with him.

I would also like to thank Professor Hugh Bruck. As director of graduate studies in Mechanical Engineering he helped to get my education at the University of Maryland started in the right direction. I have also been fortunate enough to attend one of his classes and he has helped me become a successful student.

Another person I want to thank is Professor Abhijit Dasgupta. I have had the pleasure of attending two of his classes and have learned many details in the area of nanomaterials from these classes. I made numerous trips to his office and sent many emails concerning some of this material and I am grateful for his patience and time.

Last but not least I want to thank the members of Professor Teng Li's group, Zhao Zhang, Zheng Jia, Shuze Zhu, Yinjun Huang, Jian Cheng, and others that I have been lucky enough to be a part of. I have enjoyed my time spent with them during classes, group meetings, etc. and consider it an honor to be associated with such an intelligent hard working group of individuals.

Table of Contents

Chapter 1: Introduction.....	1
1.1 Exfoliated pristine monolayer graphene.....	2
1.2 Defects in large graphene sheets grown by CVD.....	5
Chapter 2: Effect of GBs on tensile failure behavior of graphene	15
2.1 Overview	15
2.2 GB misorientation angle and loading angle	37
2.3 Structure of a twin GB.....	38
2.4 MD simulation method.....	38
2.5 MD stress and strain	39
2.6 Tensile effect from GB misorientation angle and loading angle.....	42
2.7 Continuum theory of tensile response	50
2.8 MD modeling of failure.....	58
2.8.1 GB construction.....	58
2.8.2 Triple junction	61
2.8.3 Different grain size and shapes	63
2.9 Conclusion.....	72
Chapter 3: Effect of GBs on thermal behavior of graphene	75
3.1 Overview	75

3.2	MD simulation method.....	88
3.3	Thermal effect from GB misorientation angle and loading angle.....	94
3.4	Conclusion.....	107
Chapter 4: Summary and future work		109
4.1	Summary of major findings.....	109
4.2	Scientific contributions.....	110
4.3	Future work	111

List of Figures

- Figure 1. Atomic structure of a graphene sheet. 1
- Figure 2. Exfoliated graphene sheets. (A) Photograph of a large multilayer graphene flake with thickness ~ 3 nm on top of an oxidized Si wafer. (B) Atomic force microscope (AFM) image of $2 \mu\text{m}$ by $2 \mu\text{m}$ area of this flake near its edge. Colors: dark brown, SiO_2 surface; orange, 3 nm height above the SiO_2 surface. (C) AFM image of single-layer graphene. Colors: dark brown, SiO_2 surface; brown-red (central area), 0.8 nm height; yellow-brown (bottom left), 1.2 nm; orange (top left), 2.5 nm. (D) Scanning electron microscope (SEM) image of one of the experimental devices used to measure its electronic properties. (E) Schematic view of this device in (D) [1]..... 4
- Figure 3. Images of suspended graphene sheets used to measure its mechanical properties with an indenter. (A) SEM of a large graphene flake covering an array of circular holes 1 mm and 1.5 mm in diameter. Area I shows a hole partially covered by graphene, area II is fully covered, and area III is fractured from indentation. Scale bar, 3 mm. (B) AFM image of one membrane, 1.5 mm in diameter. The solid line is a height profile along the dashed line. The step height at the edge of the membrane is about 2.5 nm. (C) Schematic of nanoindentation on the suspended graphene sheet. (D) AFM image of a fractured sheet [2]..... 5
- Figure 4. SEM images of graphene grains. The different colors within the graphene grains represents different grains of the Cu substrate, indicating that the graphene can grow continuously across Cu crystal grain boundaries [13]. 6
- Figure 5. a)-c) Growth process of graphene grains grown by CVD forming GBs. d) Raman microscope intensity map of the ‘D’ bands for two graphene grains with a single GB. The high intensity is an indication of defects in graphene [14]. ... 7
- Figure 6. 30” graphene sheet grown by CVD and transferred to a PET substrate using a roll to roll process. The 1st and 2nd labels indicate two sheets of single layer graphene were transferred onto the PET substrate [7]. 8
- Figure 7. STEM image of the atomic configuration of a GB c) Two grains of graphene (bottom left, top right) forming a GB d), The image from c) with the defects outlined as pentagons (blue), heptagons (red) and distorted hexagons (green) forming the GB. (scale bars 5\AA) [8]..... 8
- Figure 8. AFM image of a GB before and after an indentation measurement a) Indentation starts at the center of the grain as shown by the arrow. B) The sheet is torn along grain boundaries after indentation. (scale bars 200nm) [8]..... 9
- Figure 9. AFM image of a GB before and after an indentation measurement done near a GB indicated by the circle. The arrow indicates the image on the right is the image after indentation. The graphene sheet tears along the GB (scale bars 150nm) [9]..... 10
- Figure 10. AFM images of defective graphene with nanopores (a) AFM image of a graphene sheet covering a hole to be used in an indentation test. (b) High resolution AFM images of suspended graphene sheet before and (c) after

	oxygen plasma exposure of 55 s. The plasma treatment produces nanopores that are several nm in size (the dark spots in the image represent the nanopores). Scale bars (a) 1 μm , (b,c) 100 nm. [15].	10
Figure 11.	Nanomechanical testing of fracture of graphene with an initial crack. (a) SEM image showing the microdevice used to test the sheets. Movement of the nanoindenter tip (shown by the white arrow) was converted to pure tension of the specimen on the sample stage by the inclined beams. Inset is the magnified image of the boxed region showing graphene across the gap of the sample. (b,c) SEM images showing graphene before and after tensile testing, respectively. The scale bar in (b) and its inset are 5 μm and 500 nm, respectively. (d) Stress-strain curves of the cracked graphene samples (crack lengths for #3 is 1036 nm and #5 is 2512 nm) [16].	12
Figure 12.	(A) False-color Dark-field-TEM image of a suspended graphene film over a hole before indentation. The arrow indicates the indentation point. (B) Bright-field-TEM image after indentation. Black dashed lines indicate GBs. (C) Enlarged image of the red-dashed area of (B). Scale bars, 1 μm ; (C) 200 nm [10].	13
Figure 13.	Composite false color dark field-TEM images of bicrystal graphene used to determine its failure strength (e) Graphene before fracture. (f) The same sheet after fracture measurement. Scale bars are 500 nm. [11].	14
Figure 14.	Atomic structures of GBs in graphene used to analyze its failure strength and critical strain. The angles between the two grains are A) 5.5° B) 13.2° C) 21.7° D) 15.8° E) 21.4° F) 28.7° [12].	16
Figure 15.	The stress-strain curves for zigzag and armchair oriented GBs. This study shows failure strength of graphene increases with the defect density [12].	17
Figure 16.	Dimensionless stress-intensity factor versus normalized crack-spacing indicating a lower strength for higher defect density, which is in contrast to results shown in Figure 15 [12].	18
Figure 17.	Atomic structure of six GBs showing defect density increases with GB misorientation angle [17].	18
Figure 18.	Failure strength vs. GB misorientation angle (Tilt angle) showing the 16.4° and 17.9° GB misorientation angles have lower failure strength than the 13.2° GB misorientation angle. Therefore, the arrangement of the defects, not just the defect density, determines the failure strength. The two isolated points are the strengths of pristine graphene stretching in the zigzag and armchair directions, respectively [17].	19
Figure 19.	Defects forming GBs and the stress fields in graphene from MD simulations. a) A disclination dipole formed from a pentagon and heptagon ring. b), d), f), h), Normal stress contours as a result of the defects from a), c), e) and g), respectively [17].	20
Figure 20.	A partial disclination at a GB in graphene, which is defined as the point where the GB misorientation changes in a step-like manner and is located by the red	

	triangle where the periodicity, l , of the defects changes. (a) A GB in graphene without cracks. (b) A GB in graphene containing a nanocrack [21].	21
Figure 21.	GBs with a 0° and 60° misorientation angle [23].	22
Figure 22.	Atomic structures of a) matched-zigzag GBs where the left grain is held fixed in the zigzag direction and the orientation of the right grain is chosen to give several different GB misorientation angles: 4.7° , 10.9° , 14.7° , 19.1° , and 27.5° and b) matched-armchair GBs where the boundary of the left grain is along the armchair direction and the orientation of the right grain is chosen to give several different GB misorientation angles: 6.6° , 14.7° , 19.1° , 23.4° , and 27.5° [24].	22
Figure 23.	Stress-strain curves for polycrystalline graphene for different grain shapes and sizes, d . The size of the grains is determined as an average diameter for a grain assumed to be circular as indicated in d) [22].	23
Figure 24.	(a) Atomistic model for polycrystalline graphene where hexagonal grains of graphene are stitched together. (b) Stress-strain curves for polycrystalline graphene with hexagonal grains with different sizes, L , under uniaxial tension [25].	23
Figure 25.	(a) Stress concentration factor for the polycrystalline sheet with hexagonal grains and (b) stress buildup from a semi-infinite GB with length L in a graphene sheet, fitted into the logarithm scaling law. The inset shows a stress map from the top view [25].	24
Figure 26.	Experimental results of tears in graphene crossing the GB. (a) TEM image of graphene tear crossing, not following, a GB. Blue dotted lines represent tear lines in the zigzag direction. The red and yellow dotted lines represent tear lines in the armchair direction. (b) Another TEM image of a graphene tear crossing a GB and a fold in graphene [26].	25
Figure 27.	Theoretical simulations for preferred tear directions showing the direction-dependent energetics of cracks. At a given orientation of local strain with respect to graphene lattice, given by the angle χ , the lowest-energy curve represents the stable crack direction. The inset shows possible crack paths. The shortest paths normal to the applied strain (green) is favorable only in a narrow range of χ , so that armchair and zigzag-edged tears should be observed most of the time [26].	26
Figure 28.	Example of a supercell used to calculate the thermodynamic stability of graphene with GBs [27].	27
Figure 29.	Atomic structure of point vacancy, bivacancy, and Stone-Wales defects used to determine the effect of these defects on the tensile response of graphene [14].	28
Figure 30.	Stress-strain response of pristine (0%) and irradiated graphene with vacancy defects subjected to uniaxial tensile strain along the (a) armchair and (b) zigzag directions. The initial vacancy concentrations expressed as percentages of lattice sites are indicated in the figure. With the exception of the defect-free	

	case, all stress-strain curves were determined by averaging over ten initial configurations and initial conditions [31].	29
Figure 31.	Atomic structure of a rectangular and circular vacancy used to determine the effect of these defects on the tensile response of graphene [32].	30
Figure 32.	Flaw insensitive fracture of polycrystalline graphene. The image shows fracture occurs away from a large hole in the middle of the sheet [33].	31
Figure 33.	Flaw insensitive fracture of polycrystalline graphene. (a) initial atomic configuration containing a circular hole of 5 nm. (b) the onset of crack (c) Stress concentration at the hole root (d) The snapshot of graphene after failure [34].	32
Figure 34.	Flaw sensitive fracture of polycrystalline graphene. (a) initial atomic configuration of polycrystalline graphene sample containing a circular notch of 5 nm (b) the onset of crack (c) stress concentration at the hole root (d) the snapshot of graphene after failure [34].	32
Figure 35.	Snapshots of the failure process for polycrystalline graphene containing a circular hole of 20 nm [34].	33
Figure 36.	Temperature dependence of fracture obtained from the stress–strain curves of pristine graphene with uniaxial tension along the armchair direction at different temperatures from 1 K to 1800 K [35].	34
Figure 37.	Transformation of a Stone-Wales defect into two separate dislocations by using electrons from a TEM beam [37].	35
Figure 38.	MD simulation of brittle fracture for a polycrystalline graphene sheet with a pre-crack (a-c) Snapshots of crack growth process with an initial crack length $2a_0=10\text{nm}$ (d) corresponding stress-strain curve [38].	36
Figure 39.	Definition of a) GB misorientation angle, θ , and the b) loading angle, ϕ .	37
Figure 40.	Atomic structure of a) armchair GBs ranging from 2.1° - 21.8° , b) transition GBs 23.3° - 30.2° , and c) zigzag GBs 32.2° - 54.3° .	38
Figure 41.	a) Stress vs. strain plots for various graphene sheets. Snapshots of the fracture process for the b) intragranular fracture mode (inset), c) intergranular fracture mode, and d) transition fracture mode.	41
Figure 42.	Failure strength vs. loading angle for the a) armchair GBs, b) transition GBs, c) zigzag GBs, and d) pristine sheets.	43
Figure 43.	Snapshots of the critical bond breaking in the heptagon ring at the top of the disclination dipole for a) and b) $\phi = 0^\circ$ loading angle, and c) and d) $\phi = 25^\circ$ loading angle. The red line in a) and c) indicate the critical bond which is the bond that breaks first.	44
Figure 44.	Images of the a) critical bond, b) initial stress, c) stress before fracture, d) broken critical bond for the $\phi = 0^\circ$ loading angle, and e) critical bond, f) initial stress, g) stress before fracture, h) broken critical bond for the $\phi = 50^\circ$ loading angle.	45
Figure 45.	GB fracture mode map in the space of GB misorientation angle, θ , and loading angle, ϕ . Blue region is for intragranular, occurring within the grain; green is	

	transitional, occurring partly within the GB and the grain; and red is intergranular, occurring within the GB.	45
Figure 46.	Two different failure types of graphene with GBs (a) and (b) The direction of crack propagation is parallel to the GB (c) and (d) The cracks grow away from the GB. The cracks, pentagons, and heptagons are colored in green, red, and blue, respectively. The red dashed lines represent the torn edges [44].	47
Figure 47.	Contour plots of a) failure strength (GPa), and b) critical strain for the sheets of graphene with GBs for the range of all loading angles and GB misorientation angles that were analyzed.	49
Figure 48.	Atomic structure of a disclination dipole and its stress field for the x component [17].	50
Figure 49.	AC GB made of a series of periodic disclination dipoles. The points A and B indicate the location of the dipole that will have its stress field added into the initial stress calculations for the critical bond that is labeled by points C and D. S1 is the initial stress added to the critical bond from the dipole containing points A and B, and n is the normal vector defining the direction of the critical bond.	51
Figure 50.	ZZ GB made of a series of periodic disclination dipole clusters. The points A1, B1, A2 and B2 indicate the location of the dipole cluster that will have its stress field added into the initial stress calculations for the critical bond that is labeled by points C and D. S1 is the initial stress added to the critical bond from the dipole containing points A1, B1, A2 and B2, and n is the normal vector defining the direction of the critical bond.	53
Figure 51.	Comparison of GB calculations using all three stress components to only using the x component for the 0° loading angle.	55
Figure 52.	Comparison of all GB calculations with MD results from this paper for the 0° loading angle.	55
Figure 53.	Failure strength vs. GB misorientation angle for the a) 0° loading angle, and b) 25° loading angle.	56
Figure 54.	Three grains at arbitrary GB misorientation angles that are used to stitch together a polycrystalline sheet for use in the MD analysis.	59
Figure 55.	Atomic configuration of a polycrystalline sheet a) before and b) after energy minimization using LAMMPS.	60
Figure 56.	Triple junction analysis a) atomic configuration of graphene with a triple junction, b) Stress-Strain results for triple junction at different angles, θ	61
Figure 57.	Three snapshots of the usual fracture process of a triple junction showing that fracture starts at the junction.	62
Figure 58.	a) Atomic structure of a graphene sheet with an overall size of 30 nm × 20 nm with arbitrary shaped grains, b) Stress-Strain results for arbitrary shaped grain sheets with different size grains, D.	63
Figure 59.	Atomic structure for polycrystalline graphene with periodic BC's. a) top view b) side view of a 20 nm × 20 nm graphene sheet with four grains, as marked	

	by the numbered shaded areas. Lines indicate the orientations of the graphene lattice within each grain [22].	65
Figure 60.	a) Atomic structure of a graphene sheet with an overall size of 30 nm × 20 nm with hexagonal grains, b) Stress-Strain results for hexagonal grain sheets with different size grains, D.	66
Figure 61.	Atomic structure of polycrystalline graphene sheets. a) top view b) side view of a periodic 50nm × 50nm polycrystalline graphene sheet with an average grain size of 10nm consisting of 25 grains; c) top view d) side view of a periodic 20nm × 20nm polycrystalline graphene sheet with an average grain size of 1 nm including 400 grains [47].	67
Figure 62.	Deformation process of a polycrystalline graphene sheet with arbitrary grain shapes and an average grain size of 10 nm. (ϵ and ϵ_f represent current strain and failure strain, respectively). (b) Inset shows pre-existing cracks at the GBs. (c) The coalescence of existing cracks at one of the GBs. This leads to a large drop in stress-strain curve and the point where ultimate failure strength is defined [47].	69
Figure 63.	Four Fracture snapshots of the fracture of graphene with arbitrary shaped grains where the failure process starts inside the sheet at a point where the grain boundaries meet.	71
Figure 64.	Four Fracture snapshots of the fracture of graphene with arbitrary shaped grains where the failure process starts at the edge of the sheet.	71
Figure 65.	Normalized thermal conductivity of graphene as a function of various defect concentrations [30].	76
Figure 66.	(a)-(c) Graphene of different sheet lengths ($l = 25, 50, \text{ and } 125 \text{ nm}$) (d) thermal conductivity as a function of GB misorientation angle (a) 5.5° , (b) 13.2° , and (c) 21.7° [51].	77
Figure 67.	(a) Thermal conductivity, κ , of polycrystalline graphene as a function of grain size, L (b) Predicted κ , normalized by κ for pristine graphene (red dashed line is data taken from Serov et al. 2013) [52].	78
Figure 68.	Length and width dependence of graphene sheets on thermal conductivity [53].	79
Figure 69.	Thermal conductivities (κ) of graphene at room temperature as a function of the length L of graphene with widths of 1.7nm (black filled circles) and 17nm (green filled squares). The (green) solid line indicates the ballistic thermal transport limit and the (green) dot-dashed line is the macroscopic thermal conductivity[55]. The experimental data given are indicated by the (red) cross symbols. The length-dependent thermal conductivities obtained from a high-order heat transport equation are plotted by the (blue) dashed line [55].	81
Figure 70.	A sharp right-angle bend in a GNR has been shown to effect its thermal conductivity [58].	82
Figure 71.	Temperature profiles of ideal suspended (black square) and real suspended (red circle, 3 layer heat bath refers to one graphene sheet and one substrate above and one below) single-layer GNRs [59].	83

Figure 72. Thermal conductivity, G'' , vs. temperature for pristine GNR with different chiralities defined by the lattice vectors (1,4), (1,7) and (1,10), (the solid green line is for graphene with periodic boundary conditions and is not considered a GNR) [60].	84
Figure 73. Phonon transmission of graphene supported on a substrate with periodic boundary conditions. (a) Computed dispersion relation for phonon energy $\hbar\omega$ vs. wave vector q . L, T, and Z correspond to longitudinal, transverse, and out-of-plane phonon displacements. A and O labels are for acoustic and optical phonons, respectively. (b) Transmission function (i.e., number of modes per width) across pristine graphene with different chiralities. Individual chiralities are not labeled because all display the same transmission spectrum. The subset of out-of-plane ZA and ZO modes are shown separately. (c) Transmission across different GBs (g-4, g-7, g-10), revealing that transmission depends on the GB structure. LD has the worst transmission [60].	85
Figure 74. SED analysis for ZA phonons for suspended and supported graphene. (a) Normalized SED for suspended SLG (dashed line) and supported graphene with different number of layers (solid lines). Inset is for the low frequency ZA peaks. (b) SED intensity for the low frequency ZA peaks for suspended SLG (circle) and supported graphene with different layers (square) [56].	87
Figure 75. Phonon dispersion relations of a 21.78° GB misorientation angle in graphene for different applied shear strains [63].	87
Figure 76. Atomic model for the calculation of the thermal conductivity in graphene. The black atoms at the ends are fixed in their positions. The red region is determined to have a hotter temperature than the blue region. The green arrow indicates the direction of heat flux, J_x , through the sheet.	89
Figure 77. Image showing the cross sectional area that the heat flux flows through. h is the interlayer spacing in graphite.	90
Figure 78. Cumulative energy that flows along the heat transport direction in graphene as a function of time. After reaching the steady state, the constant energy per time flows as shown by the linearly fit (red dashed) line and begins here at around 10ps.	91
Figure 79. Typical steady state temperature profile for a graphene sheet. The inset shown is the temperature contour map [66].	92
Figure 80. Graphene sheet with two GBs with GB misorientation angle of 21.7° . The cold slabs on either end of the sheet and the hot slab in the middle are shown using green and red colors, respectively. The bottom figure shows a temperature profile with a distinct temperature jump at the two grain boundaries [68].	93
Figure 81. Plot of two temperature gradients for a sheet of graphene with a GB a) Atomic structure of graphene with a GB at a 45° loading angle b) Temperature profile for the graphene sheet in a) shown by the black line. The red line is temperature gradient fit to the data from the graphene region to the right and left of the GB. The green line is the temperature gradient fit to the region containing the GB.	94

Figure 82. Plot of one temperature gradient for a sheet of graphene containing a GB. All points from the temperature profile were used to get a best fit to be used as the temperature gradient (red line) using a linear fit algorithm in Matlab.	95
Figure 83. Temperature profile of a sheet of graphene and temperature gradients obtained from points in the pristine regions only [51].	96
Figure 84. Thermal Conductivity vs. Loading Angle (error bars indicate standard deviation). Thermal conductivity increases with the loading angle as an overall trend.	97
Figure 85. Graphene in series resistance from a GB.	99
Figure 86. Graphene in parallel resistance from a GB.	100
Figure 87. Graphene with a 50° loading angle. At this angle the graphene sheet is in between a series resistance and a parallel resistance and is where the thermal conductivity of the sheet starts to saturate as the loading angle is increased.	101
Figure 88. Fluctuation in the thermal conductivity vs. loading angle curves can be influenced by the number of defects in the sheets a) curve shows the thermal conductivity decreases as the loading angle is increased from 30° to 40° b) sheets show that for the 2.1° GB misorientation angle the number of defects increases from 3 to 4 as the loading angle is increased from 30° to 40°.	102
Figure 89. Thermal conductivity vs. misorientation angle for all loading angles. The graph shows the range of GB misorientation angles where the defect density is highest (~20°-30°) the thermal conductivity is lowest. This indicates that a GB with high defect density will reduce the thermal conductivity.	103
Figure 90. Thermal conductivity vs. misorientation angle for individual loading angles. For the higher loading angles the where the loading angle is parallel to the thermal transport direction the thermal conductivity does not drop as much compared to the lower loading angles. This indicates there is much less phonon-GB scattering.	104
Figure 91. The thermal conductivity for the AC GBs (Chiral angle shown is half the value of the GB misorientation angle). The thermal conductivity is reduced as the GB misorientation angle increases except for the last point. The red and blue symbols represent the pristine GNRs and GNRs with GBs, respectively. Data points with the same chiral angles means that they have the same edge roughness. The difference of thermal conductivity is derived from the GB's effects for these points [69].	105
Figure 92. The top and side views of the GNRs with different GB misorientation angles θ . (a) and (f) show no out of plane buckling, (b)-(e) show the sheet buckling out of plane in the Z direction [69].	107

Chapter 1: Introduction

The main purpose of this dissertation is to investigate the effect of grain boundaries (GBs) in polycrystalline graphene on the tensile fracture behavior and thermal conductivity of the graphene sheets. Ever since graphene was first isolated in its free standing state by mechanical exfoliation [1], there has been a significant amount of research conducted on the material because it was predicted to have an array of remarkable properties, many of which are shown to be the best material properties that have been measured experimentally. For instance it is one of the stiffest (Young's Modulus 1 TPa), strongest (Failure Strength 130 GPa) [2], can be stretched elastically 20%, more than any crystal [3], most thermally conductive (thermal conductivity 5300 W/mK) [4], most electrically conductive (carrier mobility 20,000 cm²/Vs) [5, 6], and very transparent (97.4% optical transmittance) [7]. One of the reasons that graphene has such remarkable properties is that it is one of the few materials that can be classified as being two dimensional. This is because it is composed of carbon atoms arranged in a hexagonal pattern that are bonded to form a sheet that is only one atom thick as shown in Figure 1.

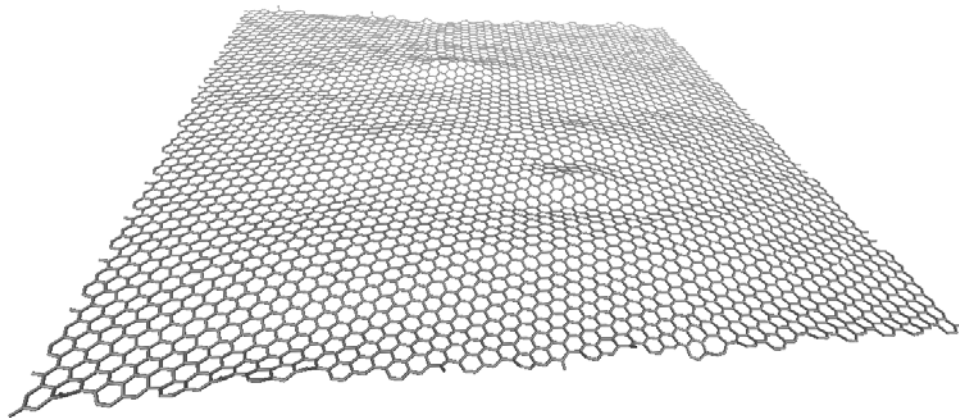


Figure 1. Atomic structure of a graphene sheet.

Pristine graphene can be produced by mechanically exfoliating the sheets from graphite, which is made of graphene layers that are bonded together by van der Waals bonds. However this method is not capable of producing the scale or quantity of sheets that are needed for many practical applications like touch or flexible screens. Chemical vapor deposition (CVD) is one method that is being developed to produce graphene that can be as long as several inches [7]. However the CVD method used to produce these sheets creates GBs in the material, which can degrade the properties of polycrystalline graphene [8-11]. One of them is the ultimate failure strength. For pristine graphene the ultimate failure strength can be as high as 130 GPa. Depending on the loading angle and GB misorientation angle this value can remain very close to the pristine failure strength [10, 11], or can be reduced to 35 GPa [9] when a GB is present. Therefore it is important to understand how defects like GBs affect the properties of graphene.

The rest of the dissertation is organized as follows. Chapter 1 provides details of the discovery and fabrication of graphene. Chapter 2 starts with an overview of previous studies from the literature on the tensile response of graphene, which is followed by a detailed description of a comprehensive study of the effect of GBs on the tensile failure of polycrystalline graphene; Chapter 3 follows a similar structure but focuses on the effect of GBs on the thermal response of polycrystalline graphene. Chapter 4 concludes the dissertation with a summary of scientific contributions, and suggestions for future work.

1.1 Exfoliated pristine monolayer graphene

In 2004, a group of researchers from the University of Manchester reported in Science [1] that they were able to produce freestanding graphene, which is a single sheet of covalently

bonded carbon atoms only one atom thick. This was done by mechanical exfoliation (repeated peeling) of small mesas of highly oriented pyrolytic graphite. Many researchers were already familiar with the composition, structure, and properties of graphene from calculations performed earlier. However, it was believed the material could not exist in a freestanding state due to thermal instability. This was the first time that graphene was actually produced and its remarkable properties proven. For instance it was shown that it had exceptional electrical properties with a room-temperature mobility of $10,000 \text{ cm}^2/\text{Vs}$. Figure 2 below shows an Atomic force microscope (AFM) image of multilayer and single layer exfoliated graphene using the method adopted in [1] and the schematic used to measure its electronic properties. This work led to an explosion in research on graphene and won the researchers from [1] a Nobel Prize in Physics in 2010.

In 2008, another paper [2] was published where elastic properties and intrinsic strength of graphene were experimentally measured. Graphene was deposited on top of a Si substrate with circular wells and an indenter was used to measure these properties. It was found that graphene has a Young's modulus of 1.0 TPa, and intrinsic strength of 130 GPa, establishing graphene as the strongest material ever measured. Figure 3 shows the experimental setup adopted for the measurement of these properties and images of the graphene sheet after it was torn by the indenter.

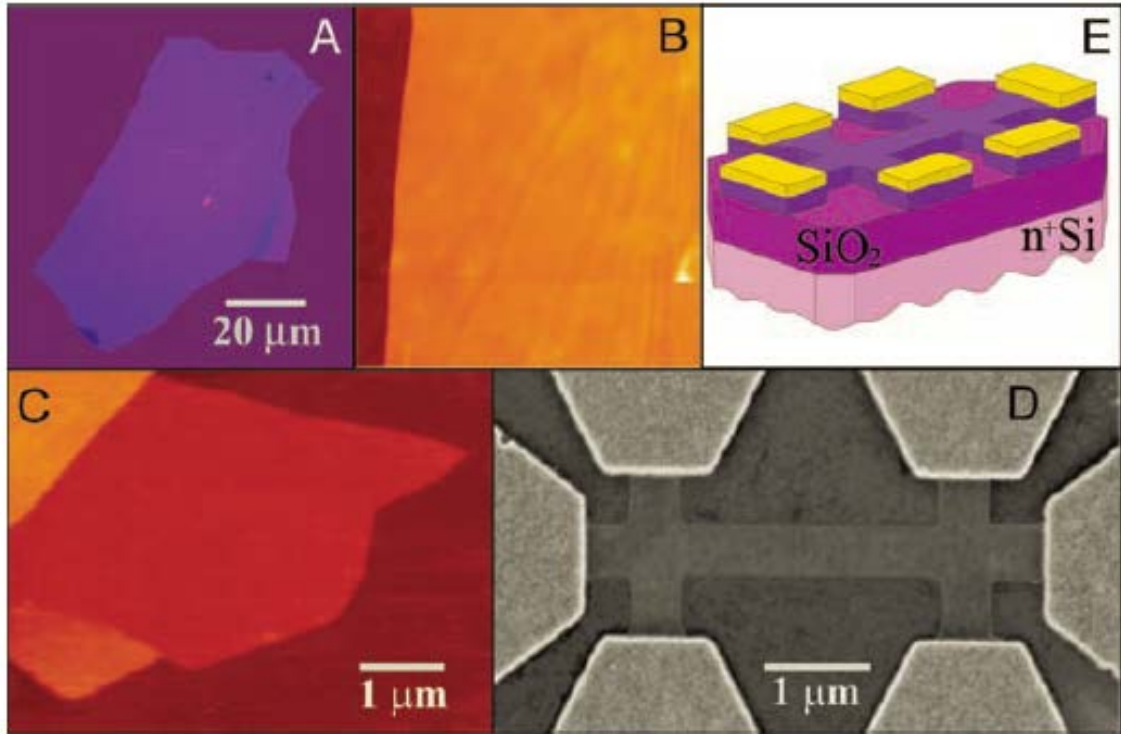


Figure 2. Exfoliated graphene sheets. (A) Photograph of a large multilayer graphene flake with thickness ~ 3 nm on top of an oxidized Si wafer. (B) Atomic force microscope (AFM) image of $2 \mu\text{m}$ by $2 \mu\text{m}$ area of this flake near its edge. Colors: dark brown, SiO_2 surface; orange, 3 nm height above the SiO_2 surface. (C) AFM image of single-layer graphene. Colors: dark brown, SiO_2 surface; brown-red (central area), 0.8 nm height; yellow-brown (bottom left), 1.2 nm; orange (top left), 2.5 nm. (D) Scanning electron microscope (SEM) image of one of the experimental devices used to measure its electronic properties. (E) Schematic view of this device in (D) [1].

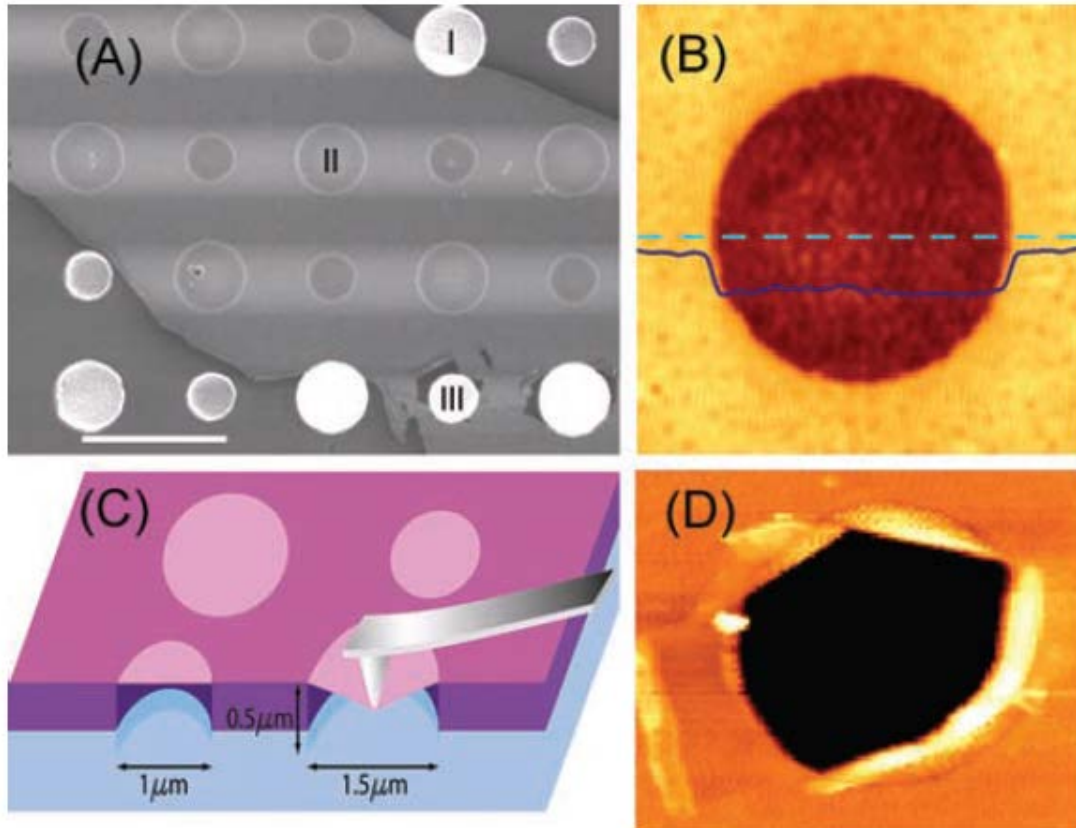


Figure 3. Images of suspended graphene sheets used to measure its mechanical properties with an indenter. (A) SEM of a large graphene flake covering an array of circular holes 1 mm and 1.5 mm in diameter. Area I shows a hole partially covered by graphene, area II is fully covered, and area III is fractured from indentation. Scale bar, 3 mm. (B) AFM image of one membrane, 1.5 mm in diameter. The solid line is a height profile along the dashed line. The step height at the edge of the membrane is about 2.5 nm. (C) Schematic of nanoindentation on the suspended graphene sheet. (D) AFM image of a fractured sheet [2].

1.2 Defects in large graphene sheets grown by CVD

The process of mechanically exfoliating graphene from graphite is easy to do but it is not a method that is capable of producing graphene in the quantity or scale that is necessary for many practical purposes. One of the widely used methods to overcome this is CVD where graphene is grown on top of some metal foil, usually copper or nickel [12]. A consequence of the CVD method is that it also produces grain boundaries in the sheets

because each grain in the metallic foil can act as a nucleation site for grains of graphene [12]. Graphene can grow over these grains [13] as shown in Figure 4, but when graphene grains grow they eventually touch to form GBs [14] as shown in Figure 5. Figure 5 also includes an image from a Raman microscope used to analyze the sheet. The high intensity areas of the image indicate defects in graphene and shows the highest intensity along the GB between the two grains and also near the middle of the grains where the grains begin to grow.

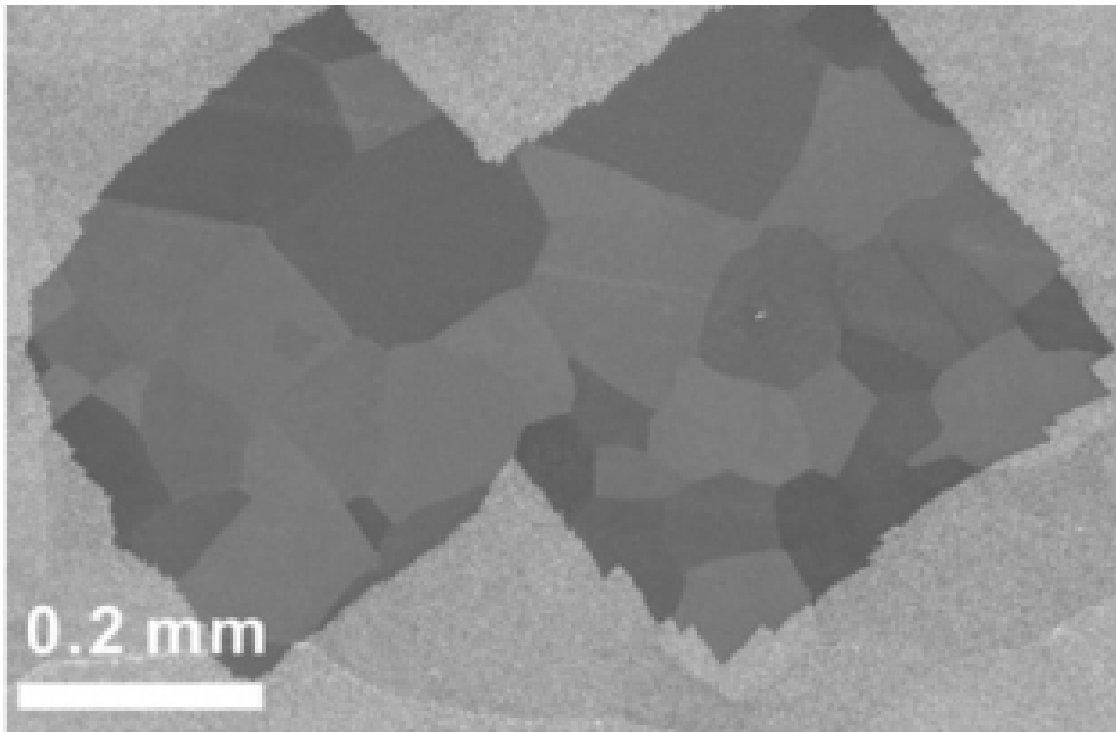


Figure 4. SEM images of graphene grains. The different colors within the graphene grains represents different grains of the Cu substrate, indicating that the graphene can grow continuously across Cu crystal grain boundaries [13].

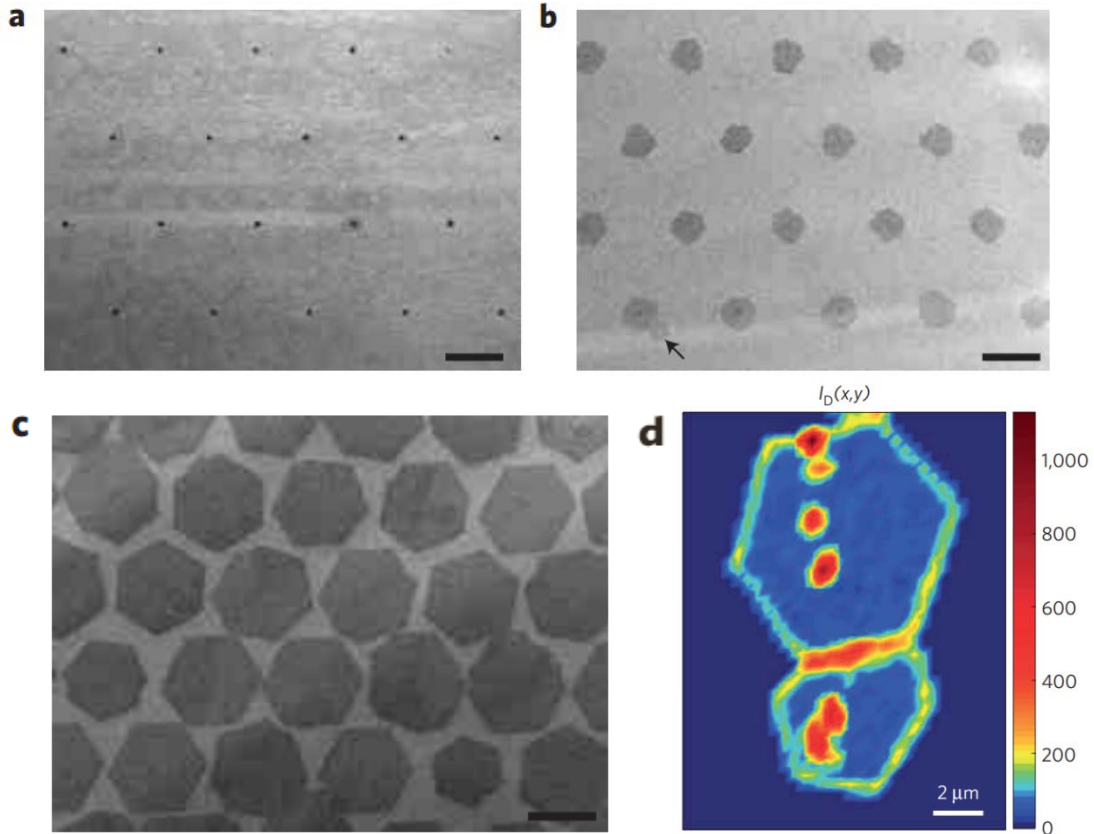


Figure 5. a)-c) Growth process of graphene grains grown by CVD forming GBs. d) Raman microscope intensity map of the ‘D’ bands for two graphene grains with a single GB. The high intensity is an indication of defects in graphene [14].

Once grown the graphene can easily be transferred to different substrates. Figure 6 shows a 30” graphene sheet that was grown by CVD and transferred to a polyethylene terephthalate (PET) substrate using a roll to roll process [7].

The GBs in graphene are usually made of pairs of pentagon and heptagon rings in the graphene lattice and follow a serpentine path. Figure 7 shows an atomic resolution scanning transmission electron microscope (STEM) image of a GB in graphene grown by CVD with the defect rings outlined for clarity [8].

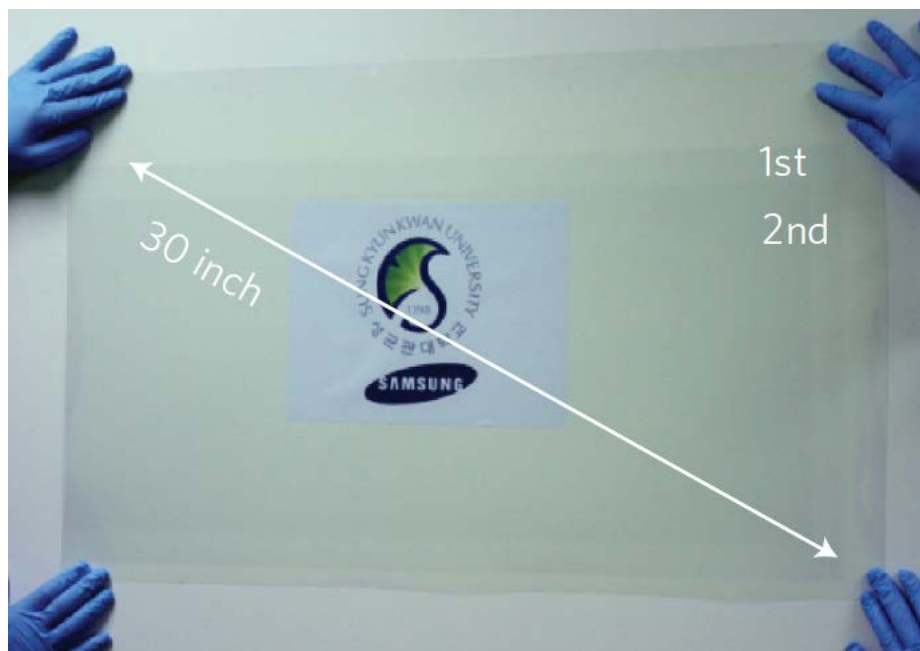


Figure 6. 30” graphene sheet grown by CVD and transferred to a PET substrate using a roll to roll process. The 1st and 2nd labels indicate two sheets of single layer graphene were transferred onto the PET substrate [7].

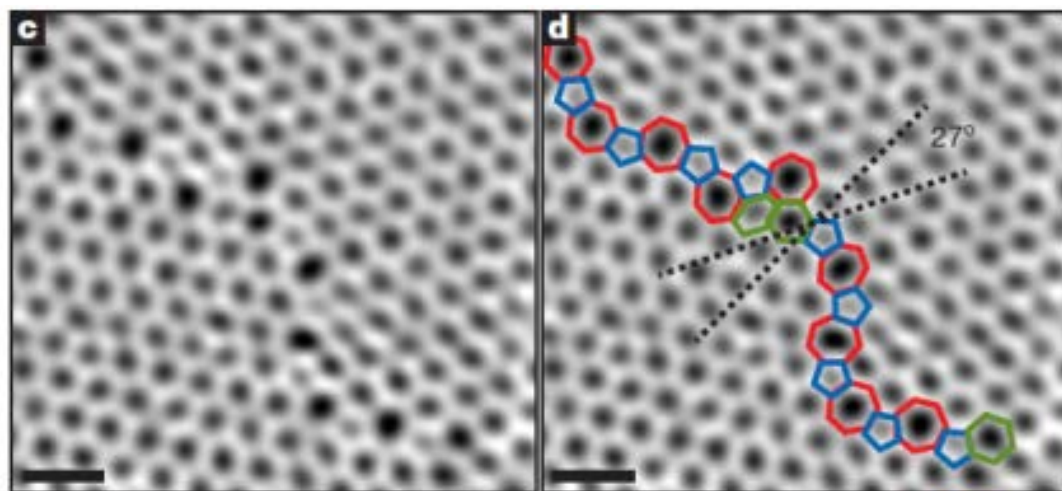


Figure 7. STEM image of the atomic configuration of a GB c) Two grains of graphene (bottom left, top right) forming a GB d), The image from c with the defects outlined as pentagons (blue), heptagons (red) and distorted hexagons (green) forming the GB. (scale bars 5Å) [8].

Atomic force microscopy (AFM) images of a graphene sheet with a GB before and after an indentation measurement are shown in Figure 8. The image shows that the sheet is torn along the GB after indentation.

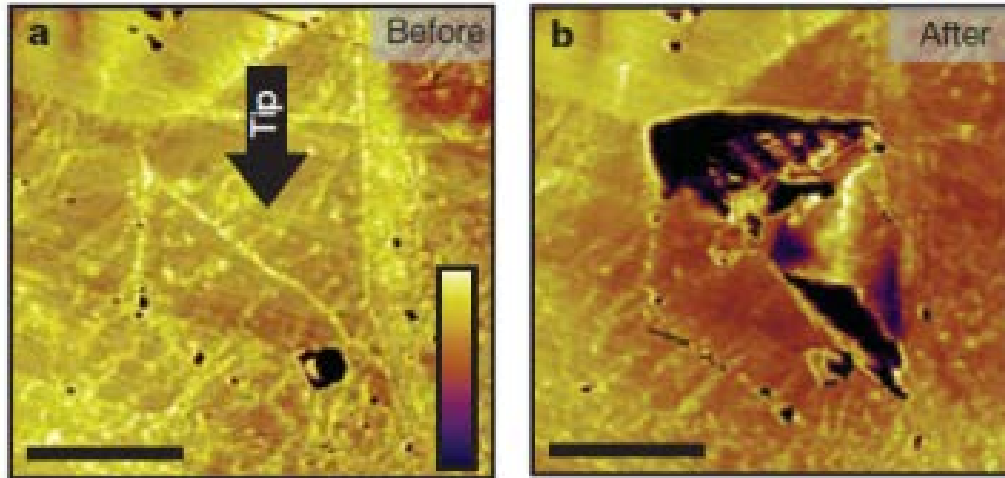


Figure 8. AFM image of a GB before and after an indentation measurement a) Indentation starts at the center of the grain as shown by the arrow. B) The sheet is torn along grain boundaries after indentation. (scale bars 200nm) [8].

The results of the indentation measurements show that failure occurs at loads of 100 nN [8], which is an order of magnitude lower than typical fracture loads of 1.7 μ N reported for exfoliated pristine graphene. The carrier mobility of the sheets with GBs were also reduced to around 7,300 cm^2/Vs [8] as compared to reported values of 20,000 cm^2/Vs for exfoliated pristine graphene.

Another image of a GB in graphene that tears along the GB from an indentation measurement is shown in Figure 9. From the indentation measurements that were performed on this sheet the estimated breaking strength was 35 GPa [9]. This is significantly lower than the breaking strength of pristine sheets of 130 GPa [2]. These studies show that there is a high probability that failure will occur along a GB as a result of tension in the sheet. Therefore it was shown that GBs in graphene reduce the properties of its otherwise pristine form and it is important to understand more about how these effects take place so they can be controlled.

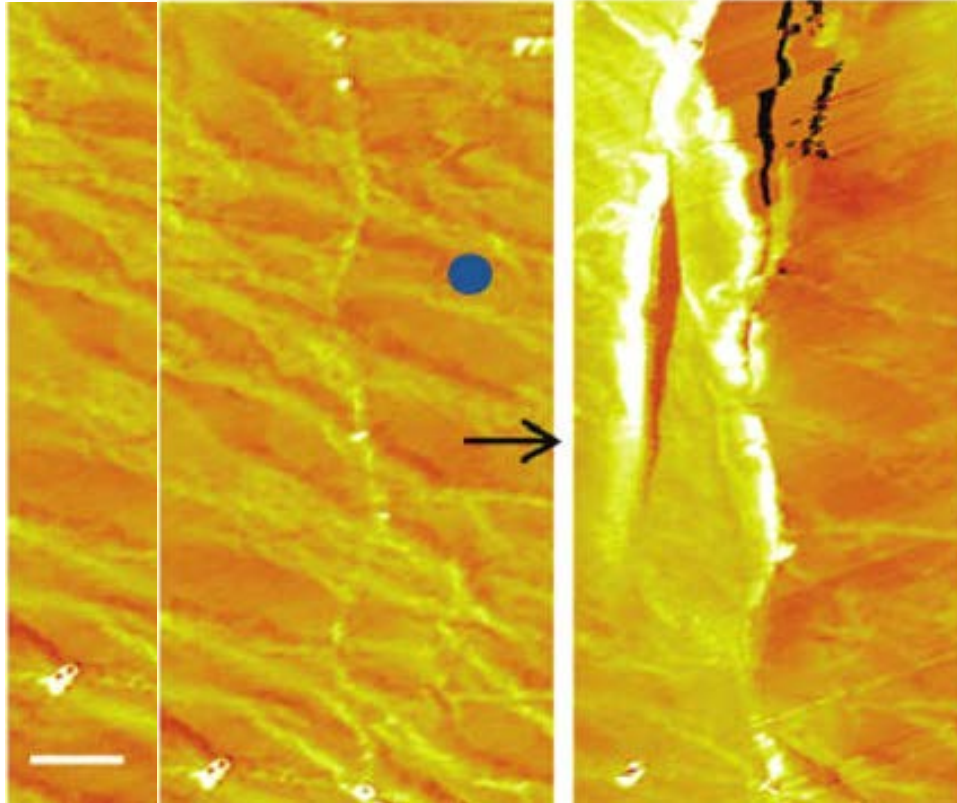


Figure 9. AFM image of a GB before and after an indentation measurement done near a GB indicated by the circle. The arrow indicates the image on the right is the image after indentation. The graphene sheet tears along the GB (scale bars 150nm) [9].

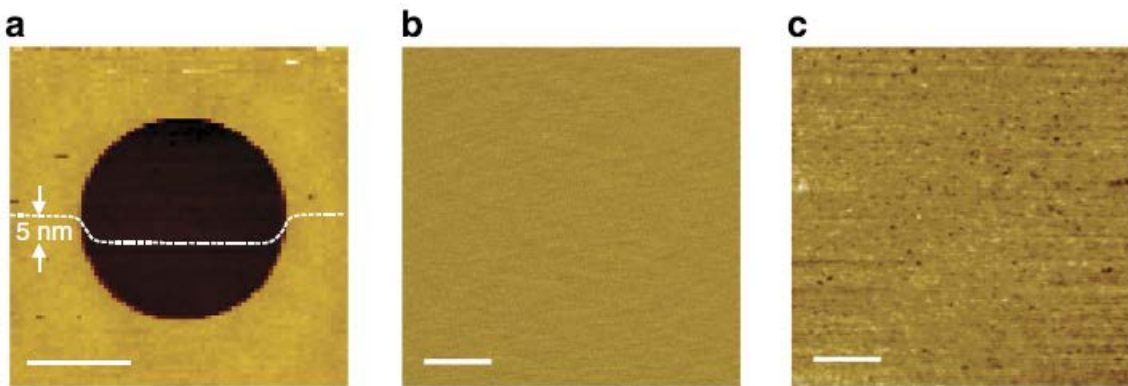


Figure 10. AFM images of defective graphene with nanopores (a) AFM image of a graphene sheet covering a hole to be used in an indentation test. (b) High resolution AFM images of suspended graphene sheet before and (c) after oxygen plasma exposure of 55 s. The plasma treatment produces nanopores that are several nm in size (the dark spots in the image represent the nanopores). Scale bars (a) 1 μm , (b,c) 100 nm. [15].

Figure 10 shows a sheet of defective graphene covering a well in a substrate. As opposed to GBs the defects in these sheets are sp^3 -type, in which an oxygen atom binds to the graphene and vacancy-type defects. The sheets of graphene are originally pristine exfoliated sheets that were transferred to the substrate and subsequently exposed to a tabletop oxygen plasma etcher to create the defects. After exposure the defects are all initially sp^3 -type and then after a longer exposure time they transition to vacancy-type defects. Results of the indentation tests [15] show the sp^3 -type defects only reduce the failure strength of graphene by 14% as compared to pristine graphene, but after the defects transition to vacancy-type the failure strength of the sheets are significantly reduced.

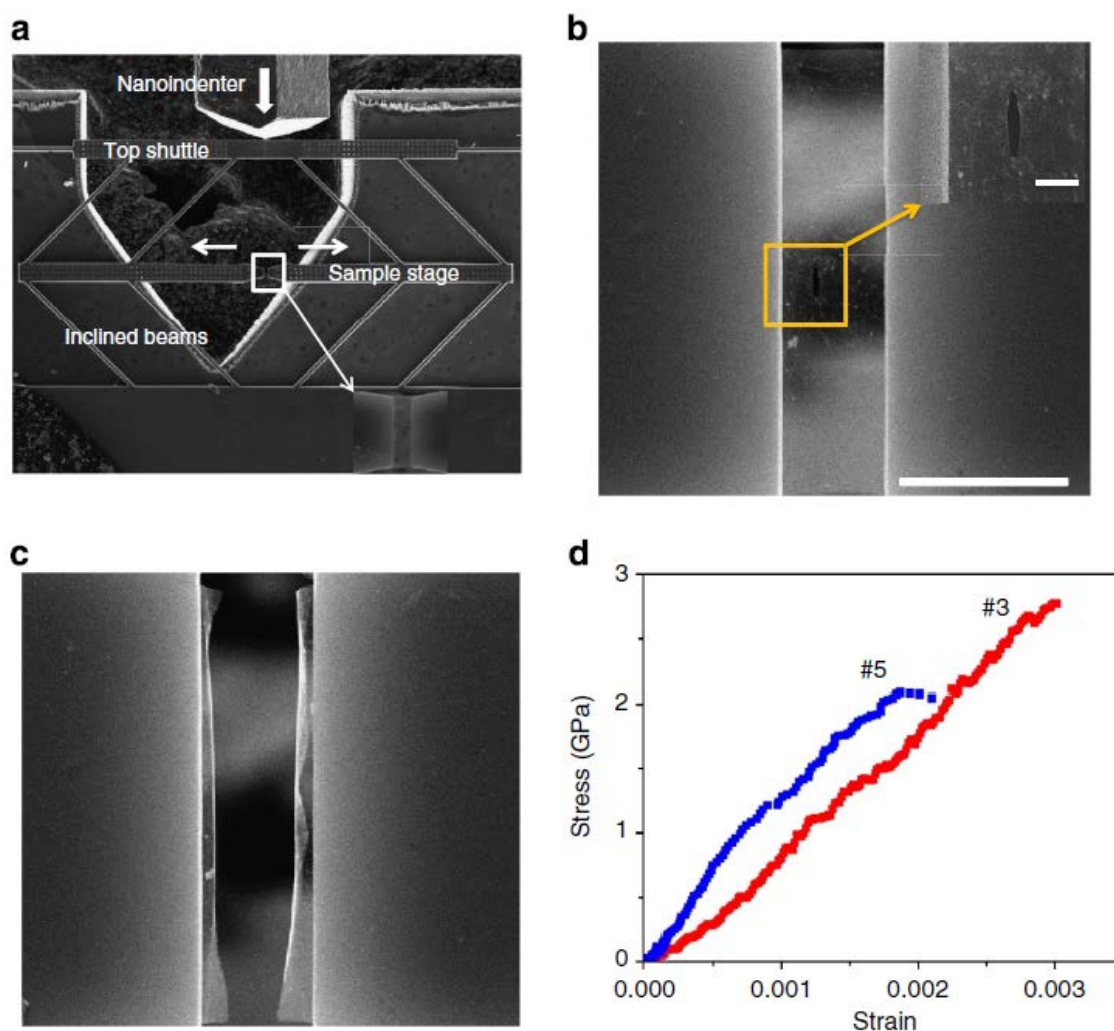


Figure 11. Nanomechanical testing of fracture of graphene with an initial crack. (a) SEM image showing the microdevice used to test the sheets. Movement of the nanoindenter tip (shown by the white arrow) was converted to pure tension of the specimen on the sample stage by the inclined beams. Inset is the magnified image of the boxed region showing graphene across the gap of the sample. **(b,c)** SEM images showing graphene before and after tensile testing, respectively. The scale bar in (b) and its inset are 5 mm and 500 nm, respectively. **(d)** Stress-strain curves of the cracked graphene samples (crack lengths for #3 is 1036 nm and #5 is 2512 nm) [16].

Figure 11 shows a sheet of graphene grown by CVD, and therefore contains GBs. In addition to the GBs an initial crack was introduced to the sheet by focused ion beam cutting. The results in Figure 11 show that the failure strength of these sheets with initial cracks are only around 2.5 GPa. This shows that cracks have a tendency to reduce the failure strength

of graphene much more than GBs alone, since results of failure strength of graphene with only GBs were found to be around 35 GPa [9].

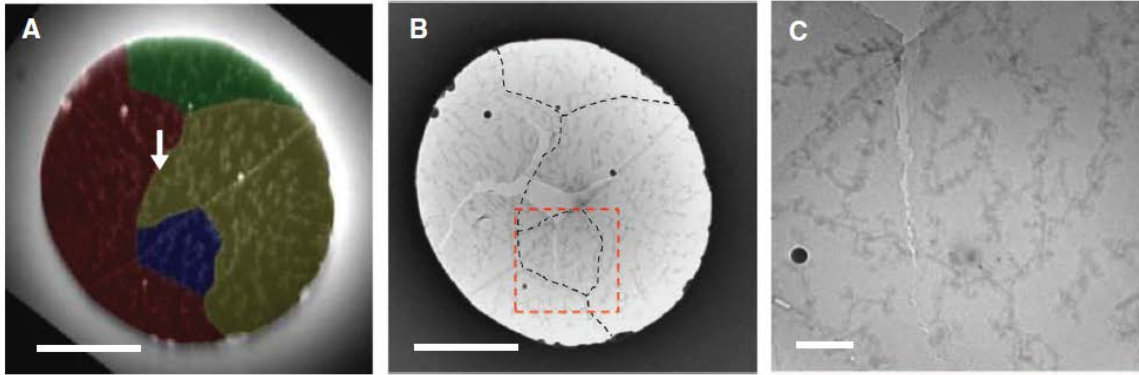


Figure 12. (A) False-color Dark-field-TEM image of a suspended graphene film over a hole before indentation. The arrow indicates the indentation point. (B) Bright-field-TEM image after indentation. Black dashed lines indicate GBs. (C) Enlarged image of the red-dashed area of (B). Scale bars, 1 μm ; (C) 200 nm [10].

Figure 12 shows a polycrystalline sheet of graphene with multiple GBs used in a nanoindentation test. Previous measurements [8, 9] using CVD graphene with GBs show that the failure strength is reduced to around 35 GPa. This is only a fraction of the value reported for pristine graphene of around 130 GPa [2]. If postprocessing steps avoid damage or rippling found in previous studies [8, 9] its strength is only slightly reduced despite the existence of GBs. The reported failure strength for these CVD polycrystalline sheets are around 103 GPa [10]. For the same study [10] the failure strength of graphene sheets with a single asymmetric GB showed a range of failure strength from 95 to 100 GPa.

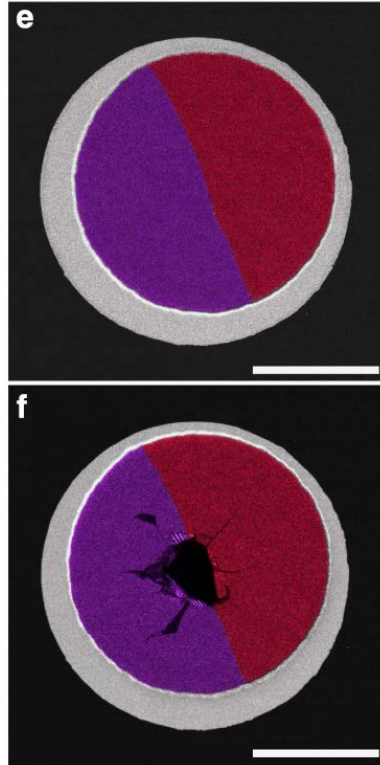


Figure 13. Composite false color dark field-TEM images of bicrystal graphene used to determine its failure strength (e) Graphene before fracture. (f) The same sheet after fracture measurement. Scale bars are 500 nm. [11].

Figure 13 shows images of bicrystal graphene with a single GB used to experimentally determine its failure strength. In these experiments [11] it was found that the GBs reduced the failure strength of graphene as well. In addition to this they also determined that an increase in the GB misorientation angle led to an increase in failure strength. As the GB misorientation angle increased from 0° to 30° the failure strength increased from 53-94 GPa.

Chapter 2: Effect of GBs on tensile failure behavior of graphene

Existing studies suggest that GBs in graphene can have significant effects on the tensile failure strength of graphene [8-11]. However, mechanistic understanding and quantitative determination of such effects are still far from mature. This chapter analyzes the effect of GBs in graphene on its failure strength and critical failure strain. Representative failure modes of polycrystalline graphene as a function of GB misorientation angle and tensile loading direction are also investigated.

2.1 Overview

The purpose of this section is to present an overview of the previous studies of the tensile response of graphene sheets containing various types of defects, such as GBs, which can be made from a periodic arrangement of disclination dipoles as shown in Figure 14. These disclination dipoles can be considered as defects in the pristine graphene and are made from one pentagon and one heptagon ring of carbon atoms. The angles indicated represent the GB misorientation angle and is the total mismatch angle between the left and right grains. The top row of GB structures in Figure 14 are defined by defects made of repeating pentagon and heptagon rings separated by hexagon rings. For various studies this type of GB has been classified as either zigzag oriented for the top row and armchair oriented for the bottom row or just the opposite.

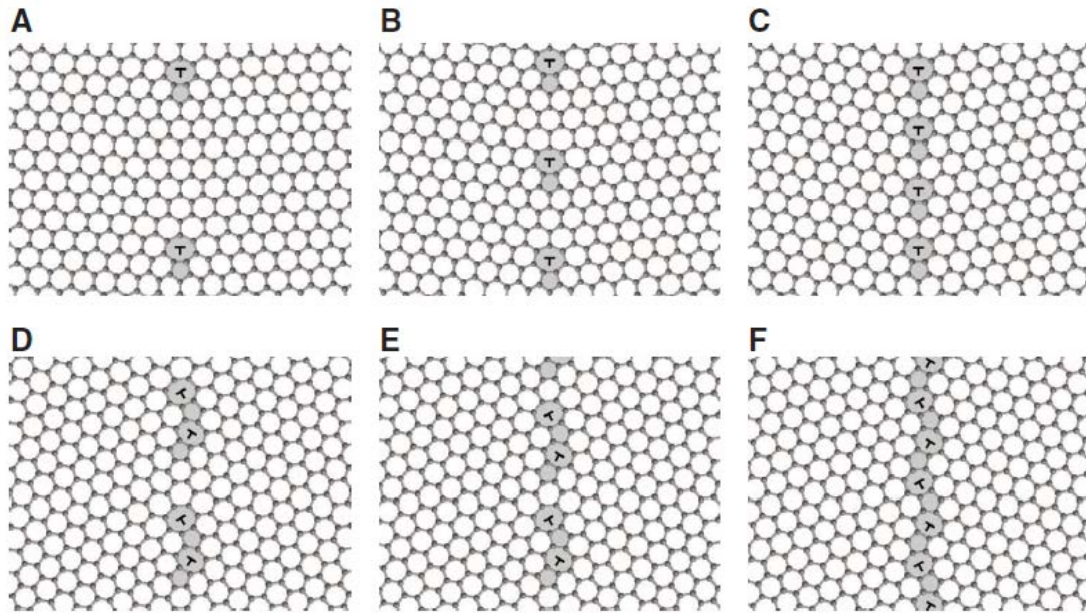


Figure 14. Atomic structures of GBs in graphene used to analyze its failure strength and critical strain. The angles between the two grains are A) 5.5° B) 13.2° C) 21.7° D) 15.8° E) 21.4° F) 28.7° [12].

The bottom row of GB structures is made from the same defects but there are two connected and are at a diagonal to each other. These structures are considered twin or symmetric GBs since the left and right grains are rotated the same amount relative to one another. Asymmetric GBs occur when the left and right hand grains are rotated different amounts relative to one another. Identification of critical bonds located at the top of the disclination dipoles was determined from [12]. The initial strain in these bonds is caused by the deformed graphene structure from the disclination dipoles and determines the failure strength of the sheets. It was found that the higher the initial strain in the critical bonds the lower the strength. It was also determined that as the defect density of the GB increased the failure strength increased. This is shown in Figure 15 where the defect density is related to the GB misorientation angle and when it increases so does the failure strength.

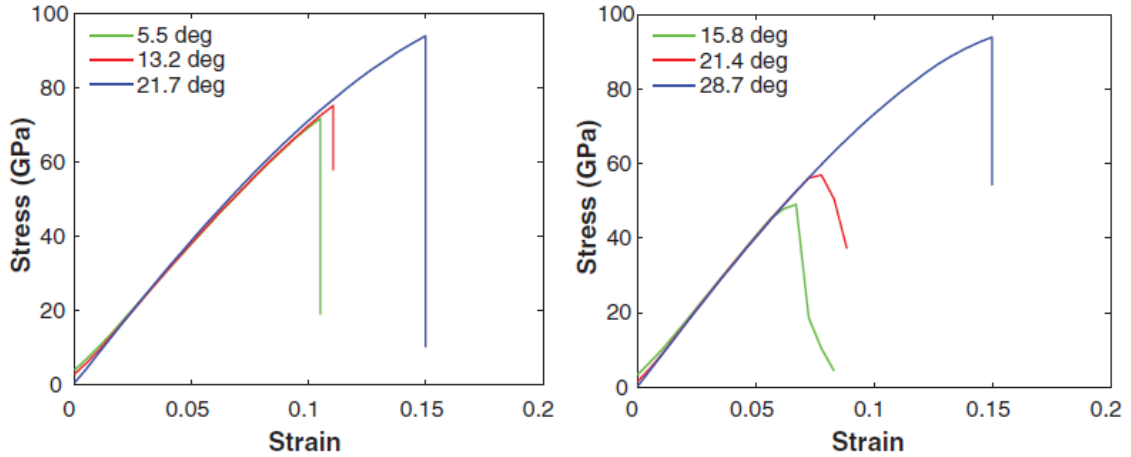


Figure 15. The stress-strain curves for zigzag and armchair oriented GBs. This study shows failure strength of graphene increases with the defect density [12].

This was in contrast to the predictions from fracture mechanics methods, which modeled the defects as cracks and predicted a lower strength for a higher defect density. This is shown in Figure 16 where the dimensionless stress-intensity factor, $K_I/(\sigma_\infty\sqrt{a})$, decreases as the normalized crack-spacing gets higher. It is assumed that if K_I exceeds K_{IC} (the experimentally measured fracture toughness for a given material), then crack propagation will occur.

Fracture mechanics was unable to predict the trends from MD simulations because the influence of strained atomic bonds was absent from the model.

It was later found that it is not just the density of defects that affects the failure strength of the sheets. The arrangement of the defects also impacts the failure strength. This was shown by analyzing GBs with clusters of disclination dipoles [17]. The GBs analyzed are shown in Figure 17 and shows the defect density increasing with the GB misorientation angle.

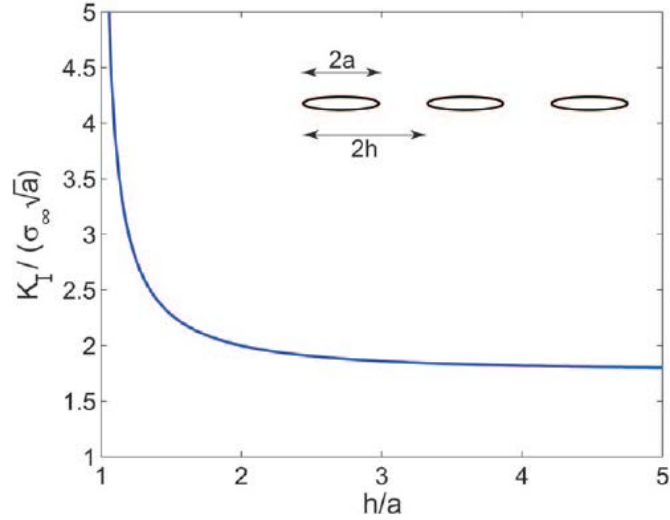
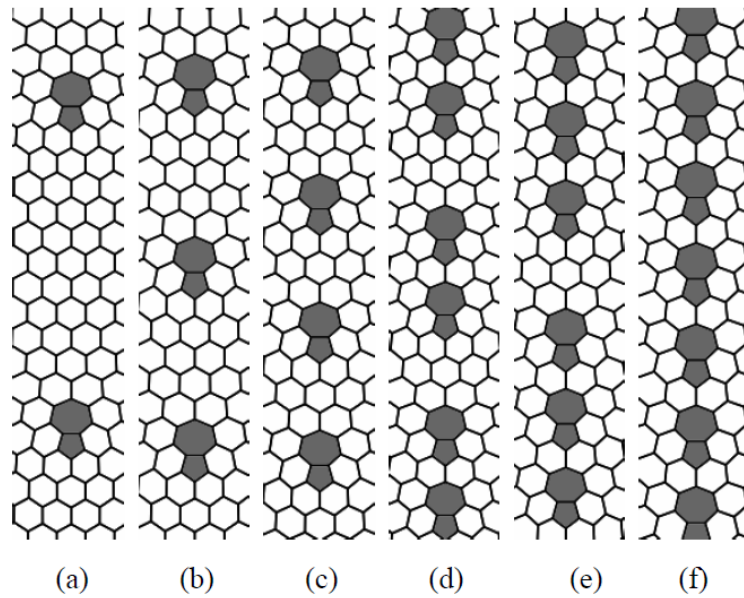


Figure 16. Dimensionless stress-intensity factor versus normalized crack-spacing indicating a lower strength for higher defect density, which is in contrast to results shown in Figure 15 [12].



a, $\theta=5.1^\circ$, b, $\theta=9.5^\circ$, c, $\theta=13.2^\circ$, d, $\theta=16.4^\circ$, e, $\theta=17.9^\circ$, and f, $\theta=21.8^\circ$.

Figure 17. Atomic structure of six GBs showing defect density increases with GB misorientation angle [17].

In contrast to the previous study the results show that the failure strength does not always increase with the defect density as shown in Figure 18. For the armchair GBs the 16.4° and

17.9° GB misorientation angle have higher defect density but lower failure strength than the 13.2° GB misorientation angle. Therefore, the arrangement of the defects, not just the defect density, determines the failure strength of graphene.

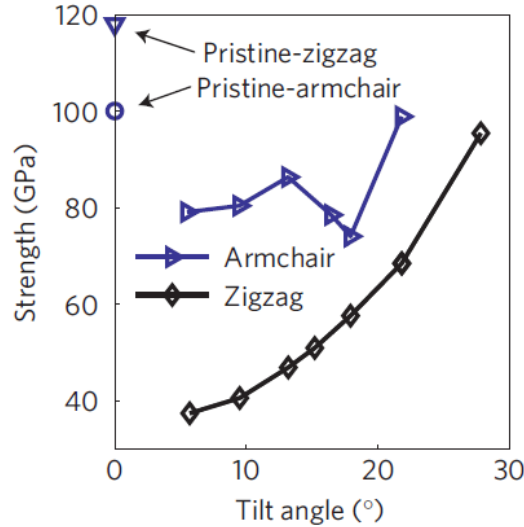


Figure 18. Failure strength vs. GB misorientation angle (Tilt angle) showing the 16.4° and 17.9° GB misorientation angles have lower failure strength than the 13.2° GB misorientation angle. Therefore, the arrangement of the defects, not just the defect density, determines the failure strength. The two isolated points are the strengths of pristine graphene stretching in the zigzag and armchair directions, respectively [17].

Figure 19 shows the initial stress field in graphene as a result of the defects and that the highest stress is at the top of the dipoles. The stress field around each defect influences the initial stress in the other bonds. Therefore the arrangement of the defects is important. Like previous studies it was also found that bond breaking normally starts at the top of the disclination dipoles, where these bonds are subjected to the highest initial tensile stress [12, 17-19]. For experimental cases [20] the strain field surrounding each dislocation has a two lobed structure similar to the shape of the stress field obtained from the MD results shown in Figure 19.

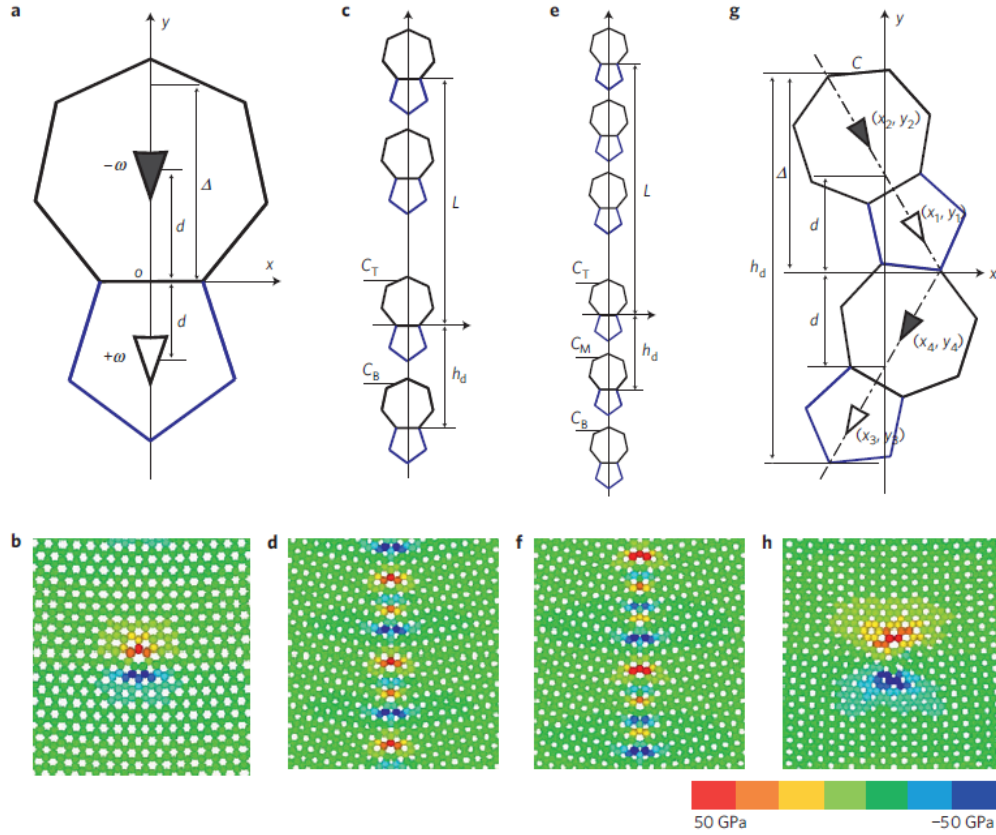


Figure 19. Defects forming GBs and the stress fields in graphene from MD simulations. a) A disclination dipole formed from a pentagon and heptagon ring. b), d), f), h), Normal stress contours as a result of the defects from a), c), e) and g), respectively [17].

These previous MD studies gave results for the failure strength of polycrystalline graphene that are slightly higher than the results obtained from experiments. A theoretical model was proposed which describes the formation of cracks at GBs containing partial (non-topological) disclinations as shown in Figure 20. A partial disclination is defined as the point where the GB misorientation changes in a step-like manner.

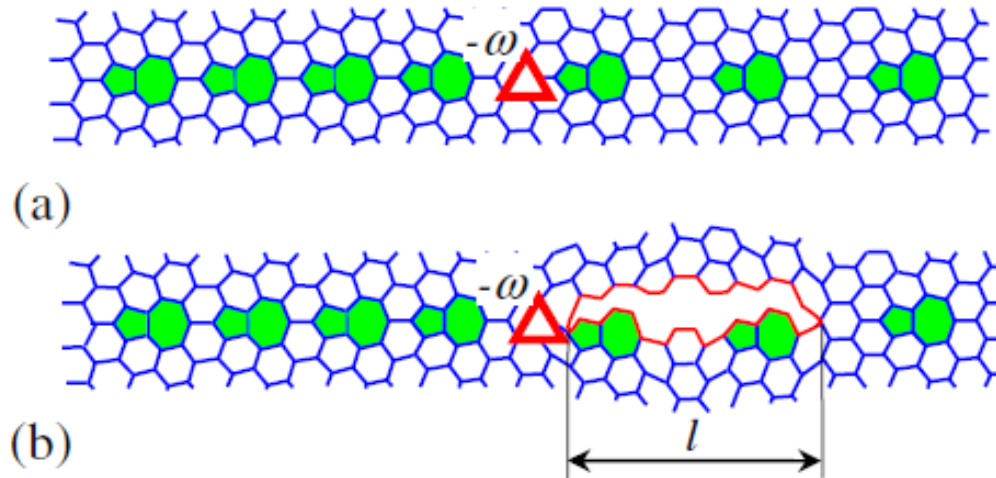


Figure 20. A partial disclination at a GB in graphene, which is defined as the point where the GB misorientation changes in a step-like manner and is located by the red triangle where the periodicity, l , of the defects changes. (a) A GB in graphene without cracks. (b) A GB in graphene containing a nanocrack [21].

In reality GBs in graphene are not like the ones that are structurally perfect in MD simulations. In this model fracture occurs where there is a change in the periodicity, l , of the defects along the GBs. The model gives an explanation for why the experimental data for the fracture of polycrystalline graphene are at comparatively low levels of stress (35 GPa) as compared with the results of computer simulations with structurally perfect, periodic GB (50-100GPa) [21, 22]. Figure 18 confirms the model since it shows the failure strength is lower for the armchair GBs when the periodicity of the single disclination dipoles is broken by clusters for the 16.4° and 17.9° GB misorientation angles.

Other types of GBs structures have also been analyzed. Figure 21 shows two special cases where the GB misorientation angle is either 0° or 60° . These two atomic configurations are usually referred to as line defects (LDs) as opposed to GBs.



Figure 21. GBs with a 0° and 60° misorientation angle [23].

Figure 22 shows GBs where the left grain is held fixed in the armchair or zigzag orientation while the right grain is rotated.

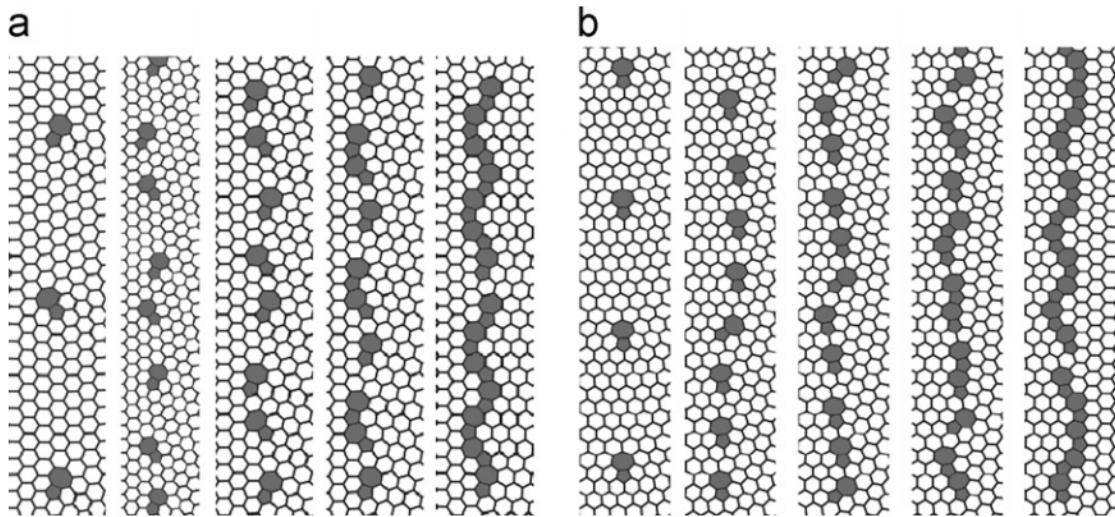


Figure 22. Atomic structures of a) matched-zigzag GBs where the left grain is held fixed in the zigzag direction and the orientation of the right grain is chosen to give several different GB misorientation angles: 4.7° , 10.9° , 14.7° , 19.1° , and 27.5° and b) matched-armchair GBs where the boundary of the left grain is along the armchair direction and the orientation of the right grain is chosen to give several different GB misorientation angles: 6.6° , 14.7° , 19.1° , 23.4° , and 27.5° [24].

MD results for the fracture of polycrystalline graphene with different grain shapes and sizes are shown in Figure 23. The results show a 50% reduction of the strength of the material and that it is independent of the grain size, d . However there was a clear size dependency for the failure strain as a function of the grain size which shows an increase in critical strain as the grain size decreased [22].

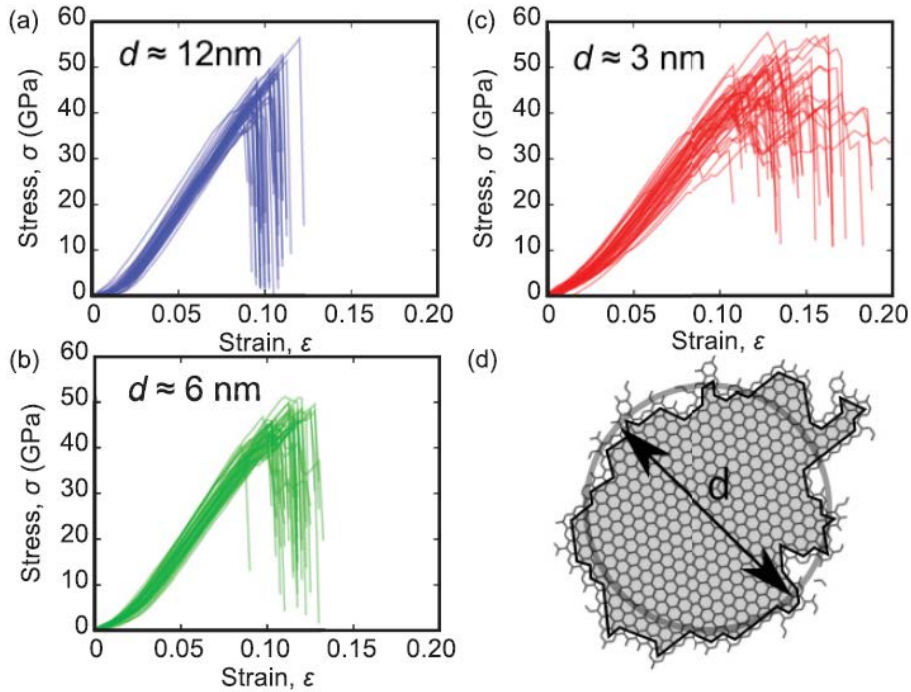


Figure 23. Stress-strain curves for polycrystalline graphene for different grain shapes and sizes, d . The size of the grains is determined as an average diameter for a grain assumed to be circular as indicated in d) [22].

Hexagonally shaped single crystal grains have been grown as shown in Figure 5. Figure 24 shows a polycrystalline sheet that could be created from these hexagonal grains.

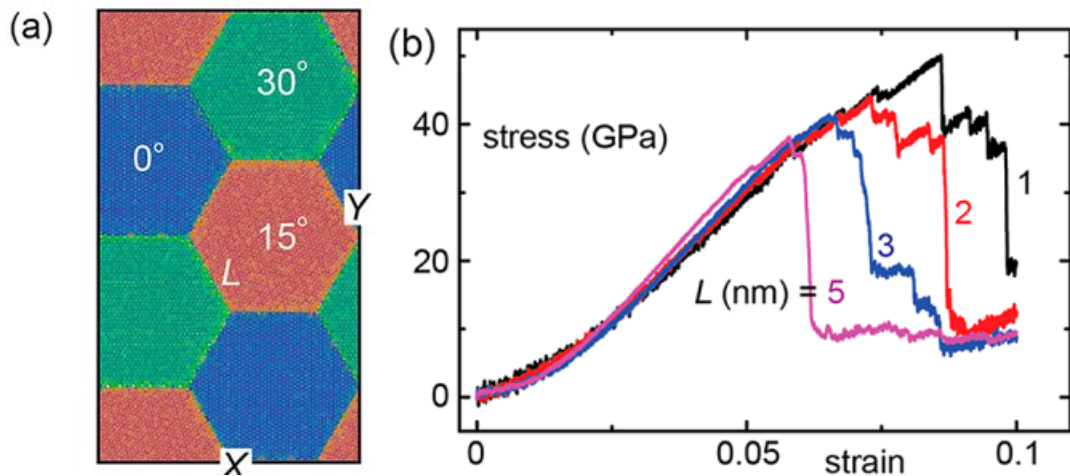


Figure 24. (a) Atomistic model for polycrystalline graphene where hexagonal grains of graphene are stitched together. (b) Stress-strain curves for polycrystalline graphene with hexagonal grains with different sizes, L , under uniaxial tension [25].

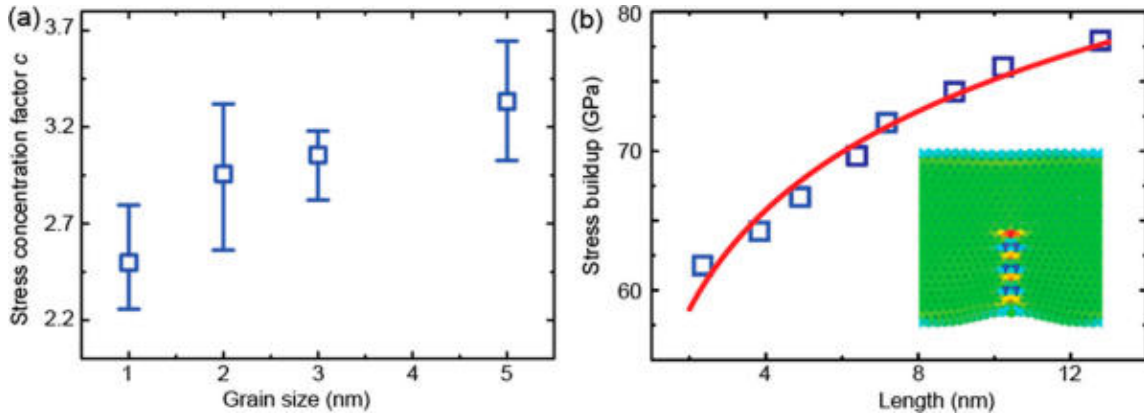


Figure 25. (a) Stress concentration factor for the polycrystalline sheet with hexagonal grains and (b) stress buildup from a semi-infinite GB with length L in a graphene sheet, fitted into the logarithm scaling law. The inset shows a stress map from the top view [25].

The sheets were made of hexagonal grains that were fit together to form idealized GBs made of only pentagon and heptagon rings. The study found that failure strength scales logarithmically with its grain size. As the grain size increases there is more stress buildup in the critical bonds in the heptagons where bond breaking starts, which leads to a smaller failure strength [25]. This is in contrast to the independence of failure strength on grain size for arbitrary shaped grains from the previous study [22], which however did not consist of idealized GBs and also included large voids. These two studies for arbitrary shaped [22] and hexagonal shaped [25] grains however both show that the critical strain increases as the grain size decreases. These studies on sheets with different grain arrangements and sizes give insight into how GBs effect the failure strength of graphene.

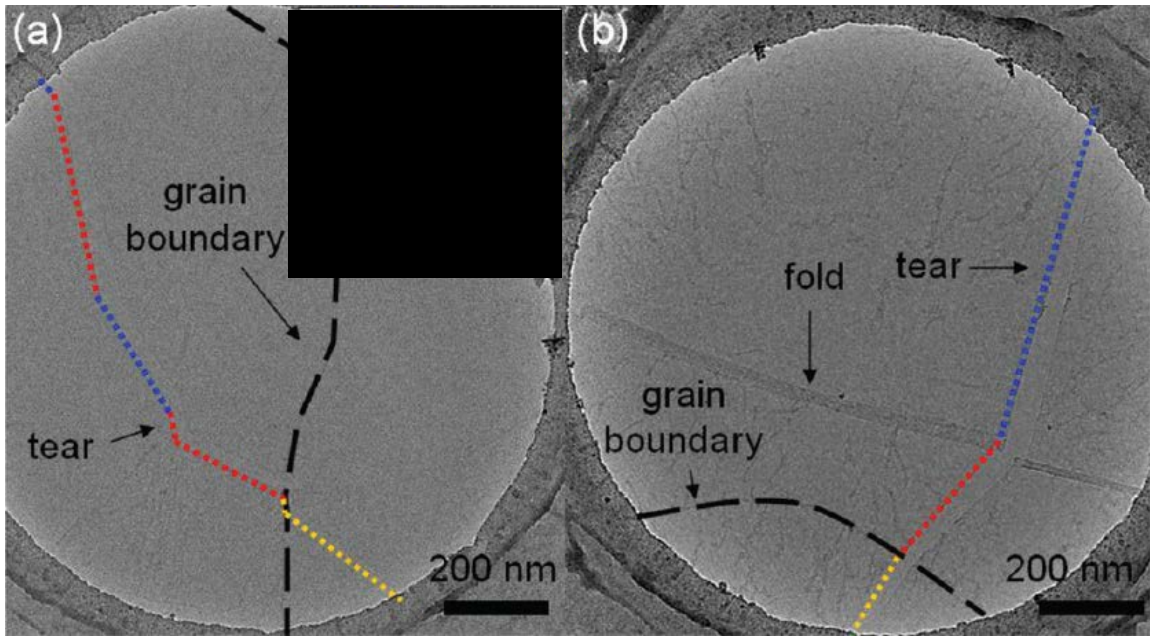


Figure 26. Experimental results of tears in graphene crossing the GB. (a) TEM image of graphene tear crossing, not following, a GB. Blue dotted lines represent tear lines in the zigzag direction. The red and yellow dotted lines represent tear lines in the armchair direction. (b) Another TEM image of a graphene tear crossing a GB and a fold in graphene [26].

Figure 26 shows experimental results of tears in graphene with GBs. Once the initial failure of the critical bond occurs the crack that is created will usually follow a certain direction through the lattice. The behavior of tears from these experimental results shown in Figure 26 surprisingly do not follow but cross the GB [26]. Figure 27 shows that the lowest energy (or work of fracture) is mainly along the armchair or zigzag direction and therefore the preferred tear direction.

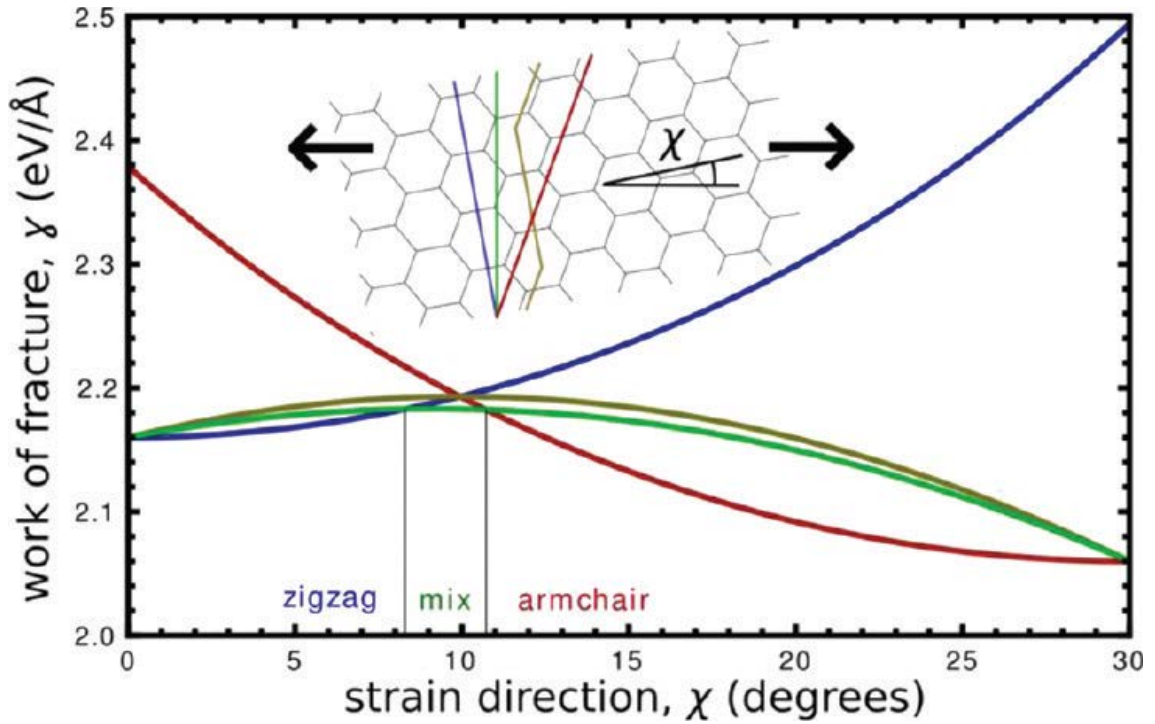


Figure 27. Theoretical simulations for preferred tear directions showing the direction-dependent energetics of cracks. At a given orientation of local strain with respect to graphene lattice, given by the angle χ , the lowest-energy curve represents the stable crack direction. The inset shows possible crack paths. The shortest paths normal to the applied strain (green) is favorable only in a narrow range of χ , so that armchair and zigzag-edged tears should be observed most of the time [26].

The shortest paths normal to the applied strain (green) is favorable only in a narrow range of applied strain direction, χ , so that armchair and zigzag-edged tears should be observed mostly. Hence, if the sheet were to break along the GB it would expose an energetically unfavorable edge. In the experimental results the tears always started at points away from the GB and then crossed them. However, it was suggested that if the tears started along the GBs and the applied stress normal to the GBs then fracture would continue along the GB [26] like the previous two studies [8, 9] from above have shown.

It was found that GB with high thermodynamic stability (low formation energy) were nearly as strong as pristine graphene [27, 28]. Thermodynamic stability of a GB can be measured in terms of the formation energy per unit length by the following equation

$$E_{form} = (E_{GB} - N \times E_{gr})/2L \quad (1)$$

where E_{GB} stands for the energy of the entire GB supercell, E_{gr} is the energy per carbon atom of the pristine graphene, N is the number of carbon atoms in the GB supercell, L stands for the periodic length of the boundary, and factor 2 accounts for two boundaries in one supercell. Figure 28 shows an example of a supercell used in the calculation.

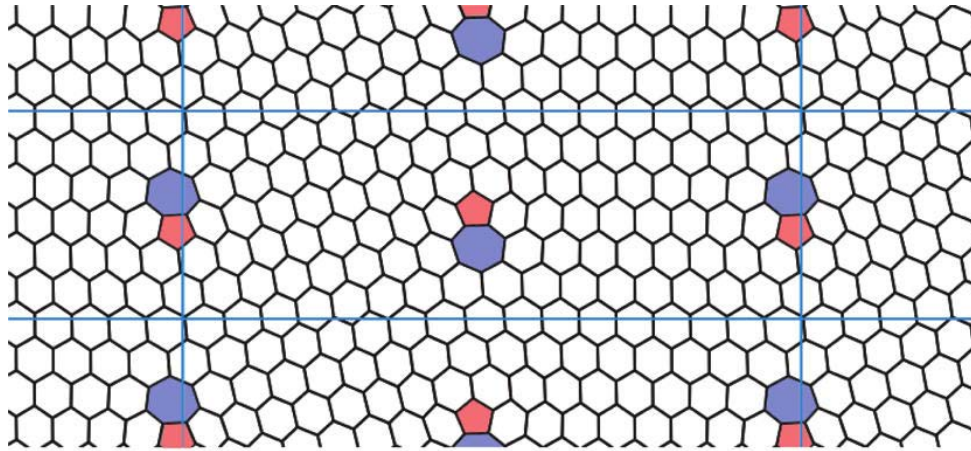


Figure 28. Example of a supercell used to calculate the thermodynamic stability of graphene with GBs [27].

Other studies using MD simulations for polycrystalline sheets show that cracks initiate at points where grain boundaries meet (triple junctions) and fail at strengths of 46 GPa[22], which is close to the failure strength in experiments of 35 GPa. These junctions are likely to occur in large polycrystalline sheets where GBs made of very long linear arrangements of dislocation dipoles are unlikely to exist without running into one another. This is another explanation [21] for the comparatively low failure strength of experimental results as compared to the MD simulations where only idealized twin GBs exist [12, 17].

Other types of defects can exist in graphene as a result of processing that effect its mechanical properties besides GBs. Irradiation of graphene with electrons or ions can generate point defects due to the ballistic ejection of carbon atoms. Chemical reactions of carbon atoms in a graphene with other species can also lead to defects [29]. Figure 29 shows point vacancies, bivacancies, and Stone-Wales defects in graphene.

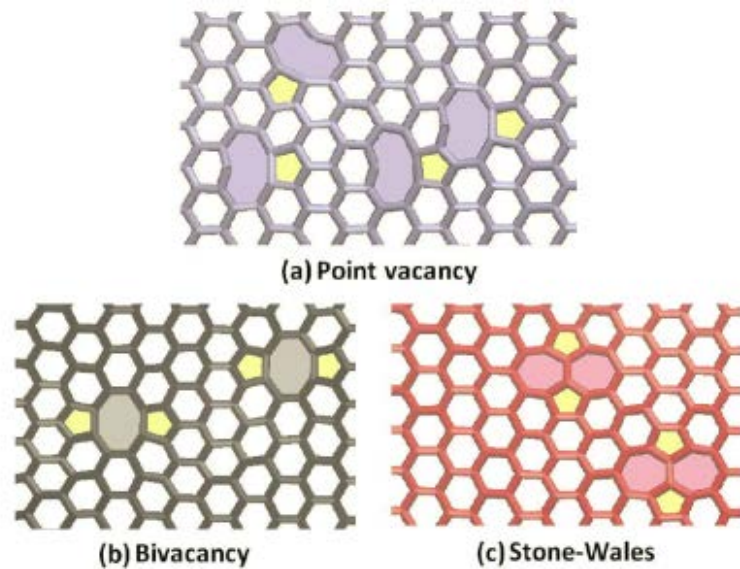


Figure 29. Atomic structure of point vacancy, bivacancy, and Stone-Wales defects used to determine the effect of these defects on the tensile response of graphene [14].

MD simulations on these defects showed a sharp decline of around 20% in the failure strength and strain at failure of graphene for only 0.25% concentration of these types of defects [30]. Another study [31] confirmed this reduction in failure strength for various vacancy concentrations as shown in Figure 30.

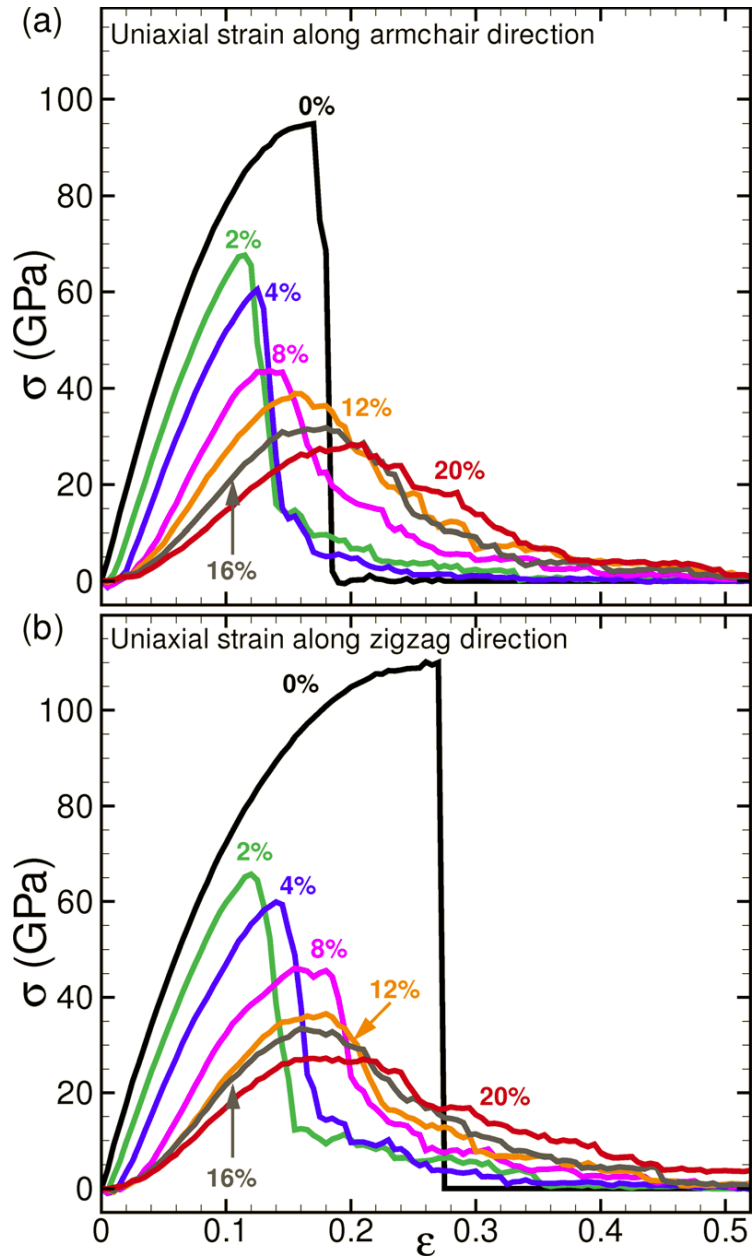


Figure 30. Stress-strain response of pristine (0%) and irradiated graphene with vacancy defects subjected to uniaxial tensile strain along the (a) armchair and (b) zigzag directions. The initial vacancy concentrations expressed as percentages of lattice sites are indicated in the figure. With the exception of the defect-free case, all stress-strain curves were determined by averaging over ten initial configurations and initial conditions [31].

With increasing vacancy concentration there is a monotonic decrease in the tensile strength of graphene, saturating at about 30GPa. Increased ductility of the damaged graphene sheets is also clearly shown from the monotonic increase in failure strains. Using irradiation can

therefore be used to increase the ductility of graphene if so desired. While these defects appreciably degrade the strength of pristine graphene the damaged samples still exhibit tensile strengths of 30 GPa, which is significantly higher than typical engineering materials [31].

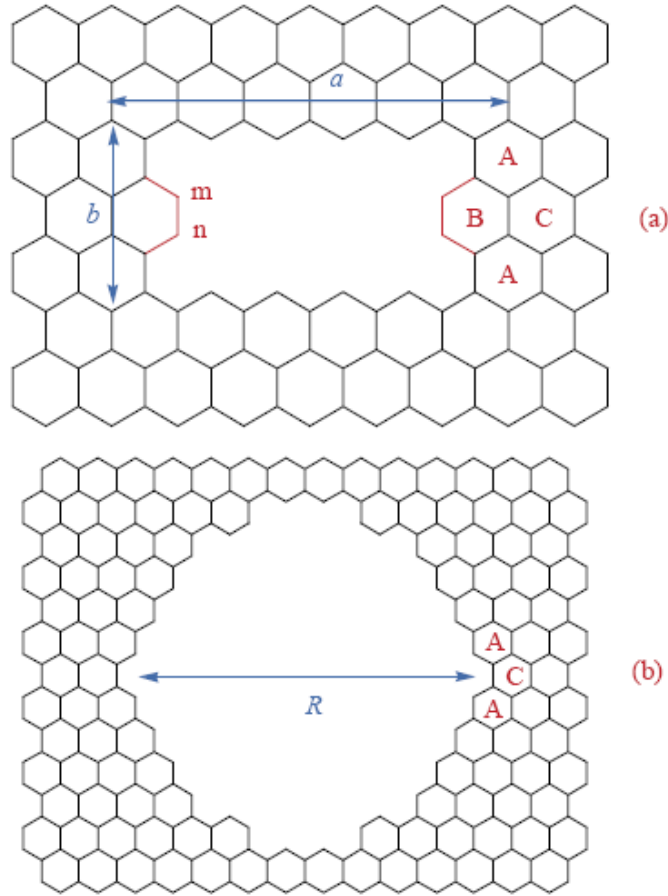


Figure 31. Atomic structure of a rectangular and circular vacancy used to determine the effect of these defects on the tensile response of graphene [32].

A rectangular and circular vacancy is shown in Figure 31. The Young's modulus of a graphene sheet with rectangular vacancy can be increased by reducing the size of the vacancy edge a or b in Figure 31. When the length of edge a of a rectangular vacancy equals the diameter of a circular vacancy ($R=a$), their fracture strength are similar. Also,

with the increase of the edge length a or b in the rectangular vacancy the crack tip exhibits an increase in its radius and is blunted which leads to a higher fracture strength [32].

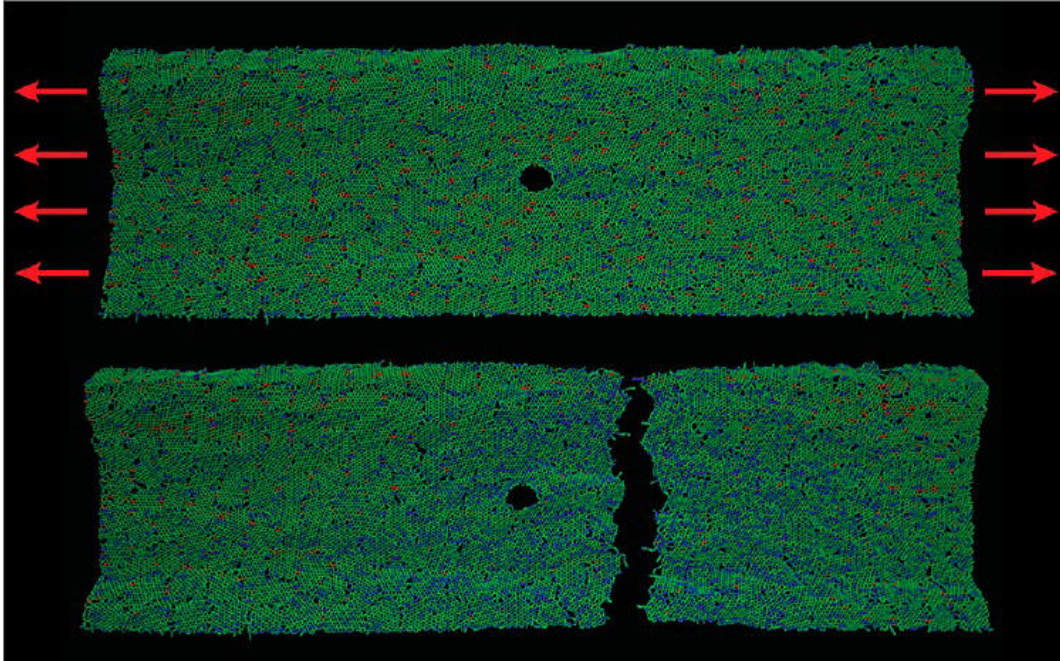


Figure 32. Flaw insensitive fracture of polycrystalline graphene. The image shows fracture occurs away from a large hole in the middle of the sheet [33].

Figure 32 shows an image of polycrystalline graphene where the fracture occurs away from a large hole in the middle of the sheet. While it was shown that GBs substantially weaken the strength of graphene, polycrystalline graphene render the material less sensitive to structural flaws when they are less than some characteristic length so that there exists no stress concentration near the flaw [33]. The key finding is that the crack nucleation and coalescence are not always induced by the larger hole or notch in the system.

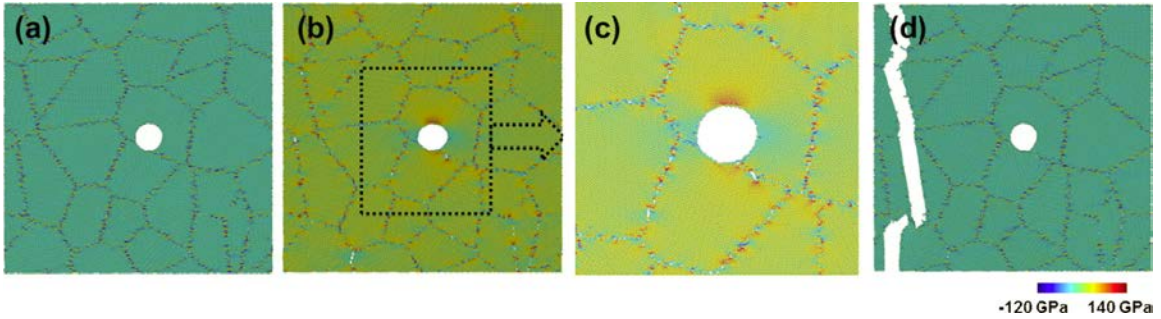


Figure 33. Flaw insensitive fracture of polycrystalline graphene. (a) initial atomic configuration containing a circular hole of 5 nm. (b) the onset of crack (c) Stress concentration at the hole root (d) The snapshot of graphene after failure [34].

The effect of some defects that are smaller than the grain size of polycrystalline have been investigated [34]. Figure 33 shows a sheet of polycrystalline graphene where the defect is a hole and the diameter is smaller than the average grain size of the sheet. For this case a GB intersects the notch but this GB is parallel to the loading direction. It can be seen that failure of the sheet occurs away from the hole.

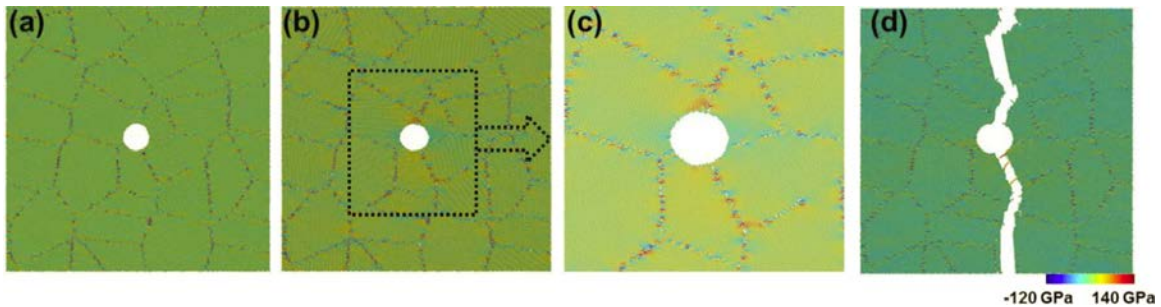


Figure 34. Flaw sensitive fracture of polycrystalline graphene. (a) initial atomic configuration of polycrystalline graphene sample containing a circular notch of 5 nm (b) the onset of crack (c) stress concentration at the hole root (d) the snapshot of graphene after failure [34].

Figure 34 shows another instance where the hole is smaller than the average grain size. In this case the GB intersects the hole again, but this time is perpendicular to the loading direction. It is shown that now failure occurs at the hole. When the notch size is smaller

than the grain size the failure depends on notch location and whether an overlapping GB is perpendicular to the loading direction.

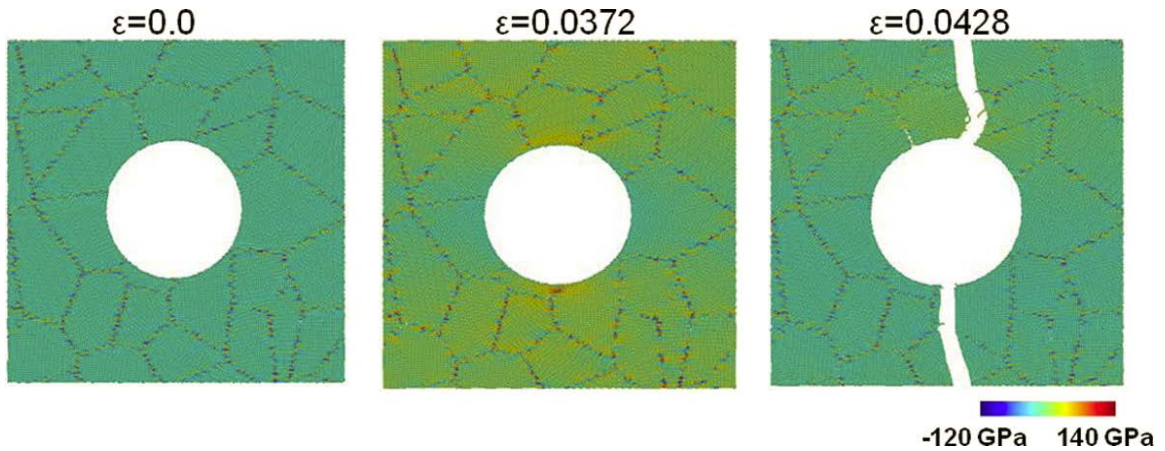


Figure 35. Snapshots of the failure process for polycrystalline graphene containing a circular hole of 20 nm [34].

For the fracture shown in Figure 35 a large notch will cause a notch-sensitive failure because the overlapping stress concentration zone cannot be avoided. When the notch diameter is larger than the average grain size, the failure is generally notch-sensitive. If the stress concentration zone of the notch is within the grain interior failure is notch insensitive and the failure initiates at the weakest GB elsewhere.

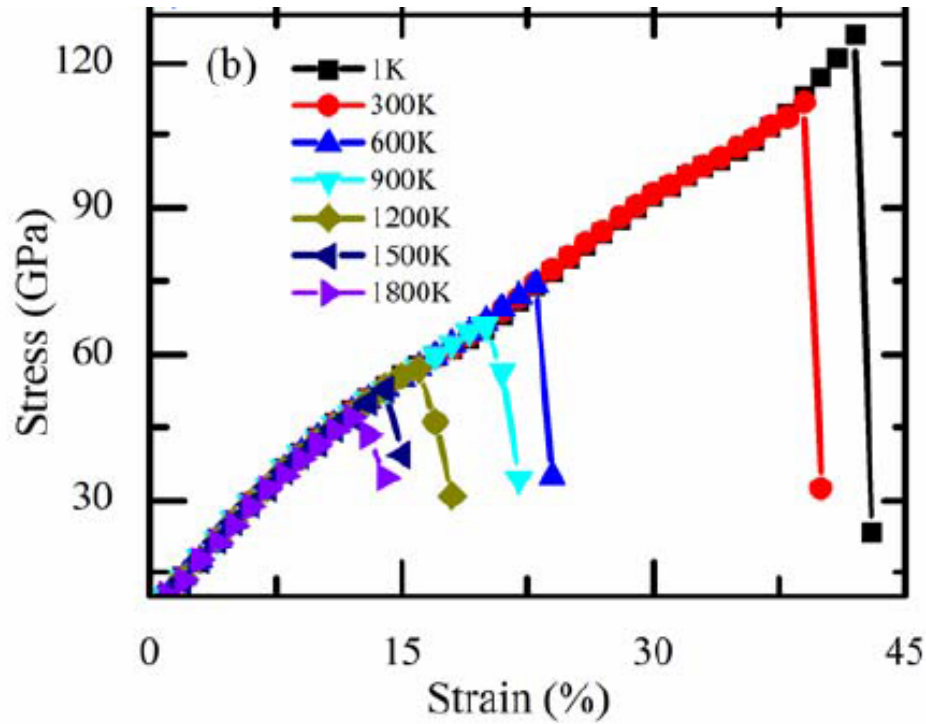


Figure 36. Temperature dependence of fracture obtained from the stress–strain curves of pristine graphene with uniaxial tension along the armchair direction at different temperatures from 1 K to 1800 K [35].

It is also important to mention that the parameters used in the MD simulations have an effect on the results. Figure 36 shows the temperature dependence on the fracture of graphene. As the temperature increases the fracture stress and strain decreases for graphene [35]. It was also shown that the tensile strength can be reduced by using a lower strain rate in the MD simulations [36].

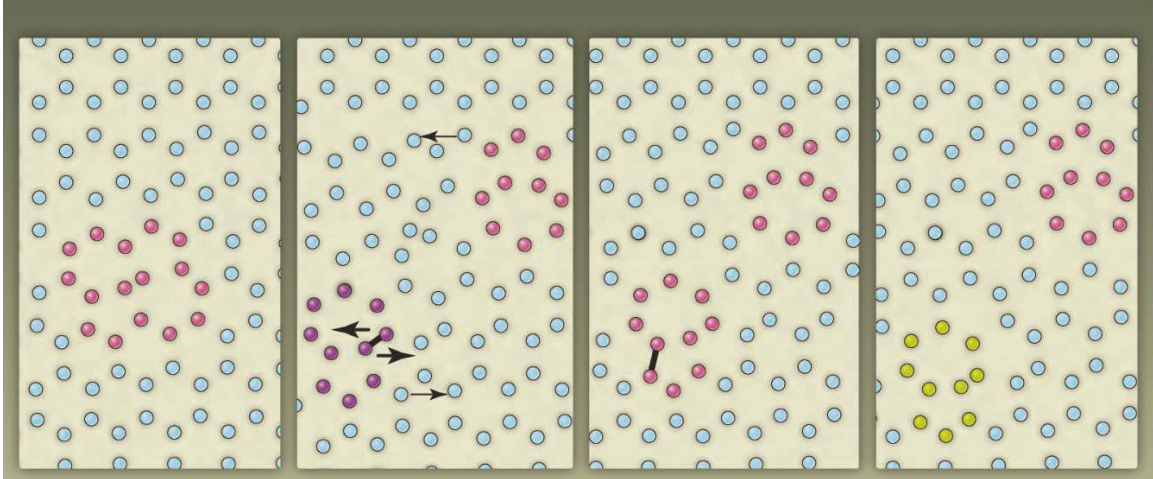


Figure 37. Transformation of a Stone-Wales defect into two separate dislocations by using electrons from a TEM beam [37].

Knowing why defects move through the lattice and having a way of controlling the arrangement of these defects to control the properties of graphene has been studied [20, 37]. Figure 37 shows the manipulation of a defect in graphene using a transmission electron microscope (TEM). The TEM was used to create two defects from the Stone-Wales defect then translate the defects in different directions. This could be used to create specific patterns of defects or GBs in graphene to control its properties.

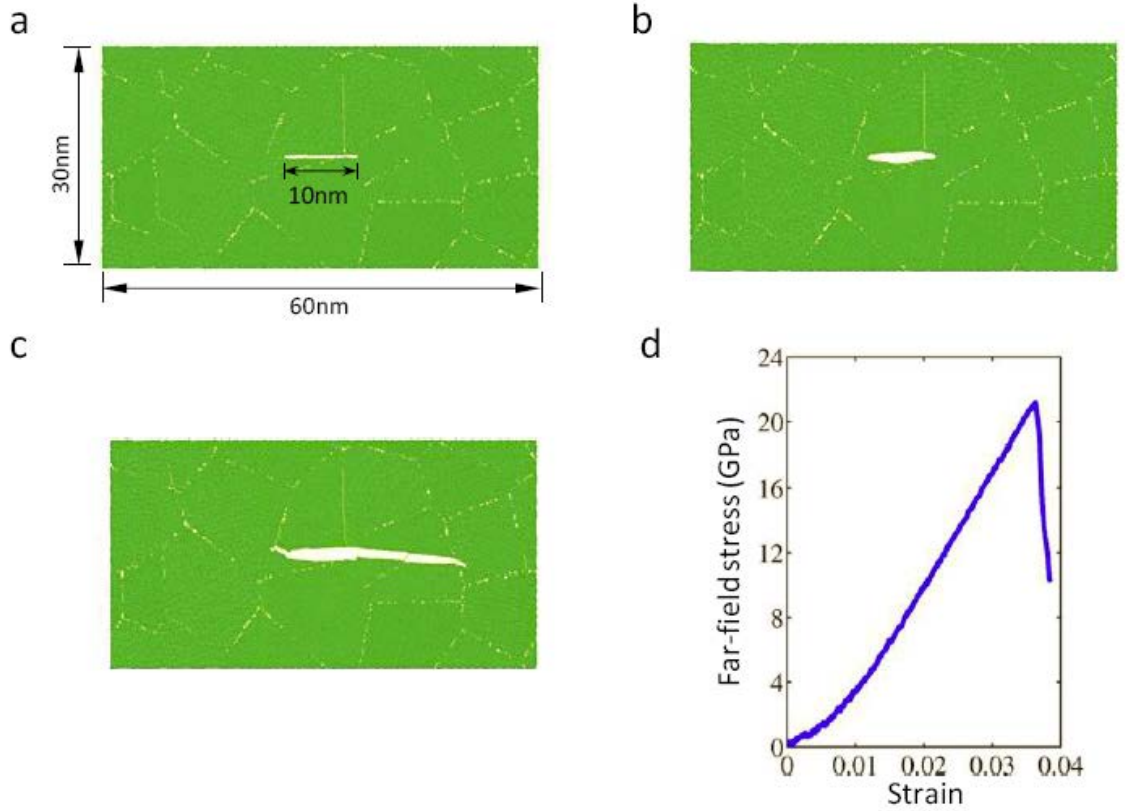


Figure 38. MD simulation of brittle fracture for a polycrystalline graphene sheet with a pre-crack (a-c) Snapshots of crack growth process with an initial crack length $2a_0=10\text{nm}$ (d) corresponding stress-strain curve [38].

Fracture mechanics was unable to predict the relationship between defect density and failure strength for graphene sheets that contain a single GB [12]. However, the applicability of Griffith theory was shown to apply to polycrystalline graphene sheets to predict brittle fracture [38]. The Griffith criterion to determine whether or not brittle fracture occurs can be determined using Eq. (2).

$$\sigma_c \sqrt{a_0} = \sqrt{\frac{2\gamma E}{\pi}} \quad (2)$$

where σ_c is the critical stress, $2a_0$ is the crack length, γ is the surface energy, and E is Young's Modulus. The theory of brittle fracture is applicable to graphene if the pairs σ_c

and a_0 give a constant product of $\sigma_c\sqrt{a_0}$. Results of the product from MD simulations and experiments on polycrystalline sheets [40] indicated that the product could be considered a constant. Therefore the classic Griffith theory of brittle fracture applies to polycrystalline graphene.

2.2 GB misorientation angle and loading angle

Analysis of graphene with twin GBs has been investigated for their effect on failure strength and critical strain. The loading angles considered previously were only perpendicular or parallel to the loading direction. In reality large graphene with many grains will have GBs dispersed throughout in various directions. Therefore it is important to have an understanding of the effect of different loading angles. This analysis looks at the effect of different loading angles ranging from 0-90°. Figure 39 shows how the GB misorientation angle and loading angle are defined.

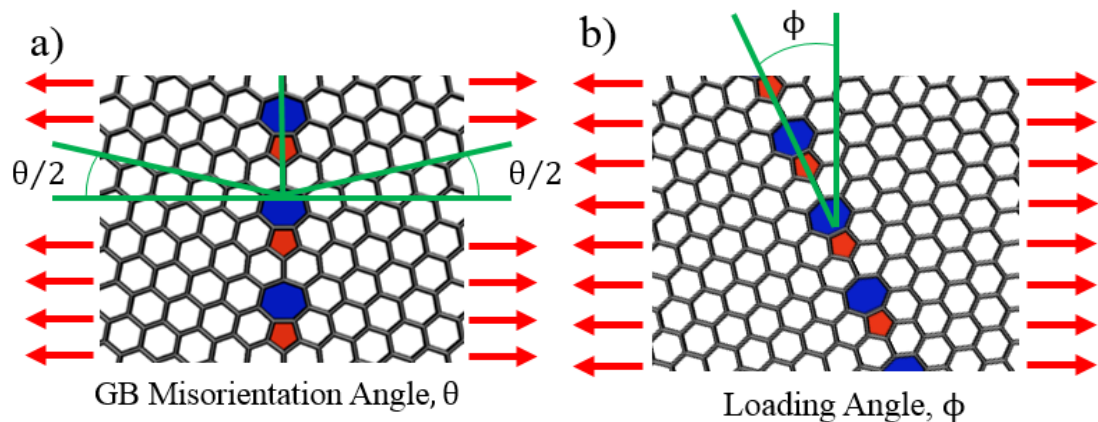


Figure 39. Definition of a) GB misorientation angle, θ , and the b) loading angle, ϕ .

2.3 Structure of a twin GB

Figure 40 shows a GB composed of arrays of disclination dipoles made from pentagon and heptagon rings embedded in graphene. The 24 GB structures analyzed were made of different configurations of pentagon or heptagon rings along the GB. Each GB is in an idealized atomic configuration that would result from two grains being in their given orientation relative to one another. These structures are similar to previous studies that have been conducted on GBs in graphene [12, 17, 27, 39-41]. The GBs are divided into three main categories. The armchair (AC) GBs have a GB misorientation angle in the range of 2.1° to 21.8° , transition GBs range from 23.3° to 30.2° , and zigzag (ZZ) GBs range from 32.2° to 54.3° . The AC GBs are divided into three categories based on whether the GB is made of 1 (1dp), 2 (2dp), or 3 (3dp) disclination dipole clusters.

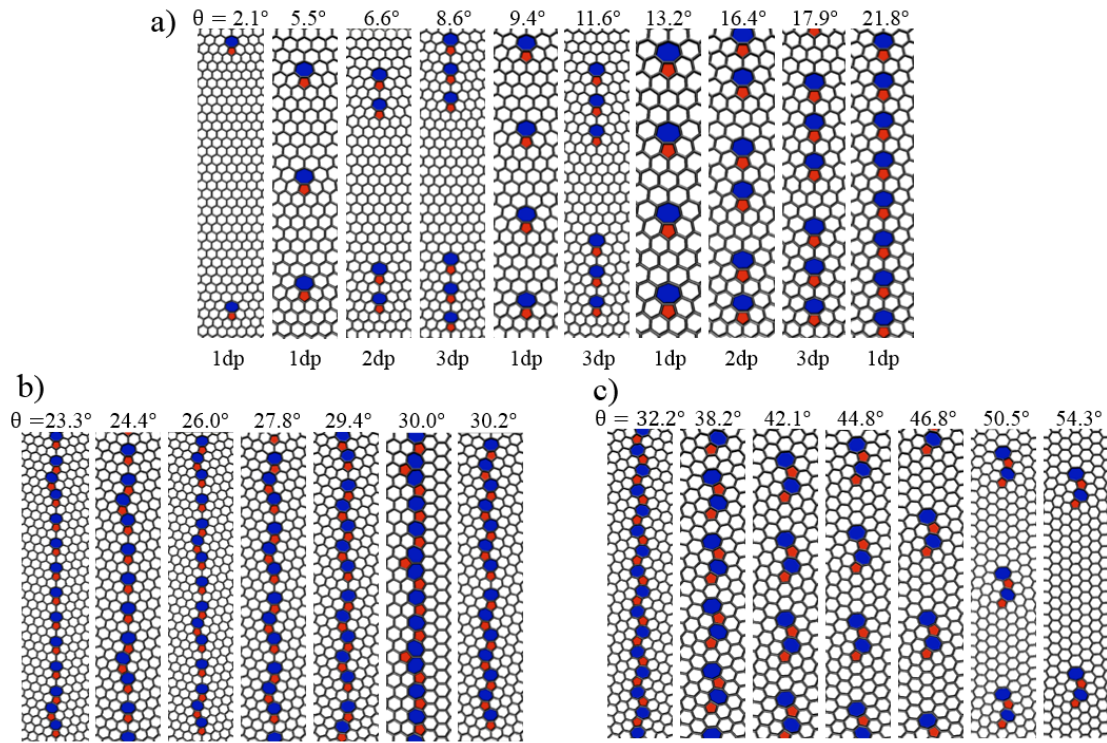


Figure 40. Atomic structure of a) armchair GBs ranging from 2.1° - 21.8° , b) transition GBs 23.3° - 30.2° , and c) zigzag GBs 32.2° - 54.3° .

2.4 MD simulation method

Matlab was used to generate the atomic configuration of the GB structures in two dimensions. The Large-scale Atomic/Molecular Massively Parallel Simulator (LAMMPS) was used for the MD analysis. First an energy minimization was performed, which also allowed the structure to buckle in the third dimension to find the lowest energy state of the

sheets. From there an assigned displacement was incrementally applied to one end of the sheet while the other end was held in place until fracture occurred. The adaptive intermolecular reactive bond order (AIREBO) potential was used to model the interaction of the carbon atoms and their bond breaking and formation[42]. In order to overcome unreasonably high tensile forces when the carbon–carbon bond length is greater than 1.7 Å, the onset of the covalent interaction cutoff distance was increased to 1.92 Å, so that the carbon-carbon bond interactions more closely resemble what is observed in physical experiments[12, 17, 39]. The size of the graphene sheets were 120x120 Å². Non-periodic boundary conditions (BC's) were used on all sides. A Berendsen thermostat with an NVE integration scheme was used in the simulations and the temperature was set at 300 K. The time step used was 0.001ps. Tensile strain was applied to one edge with a strain rate of 0.0005/picoseconds.

2.5 MD stress and strain

In order to calculate the stress-strain curves of the sheets during deformation, the stress on each individual carbon atom was first calculated using the following equation[12]

$$\sigma_{ij}^{\alpha} = \frac{1}{\Omega^{\alpha}} \left[\frac{1}{2} m^{\alpha} v_i^{\alpha} v_j^{\alpha} + \sum_{\beta=1,n} r_{\alpha\beta}^j f_{\alpha\beta}^i \right] \quad (3)$$

where i and j denote the indices in the Cartesian coordinate system, α and β are the atomic indices, m^{α} and v^{α} are the mass and velocity of atom α , respectively, $r_{\alpha\beta}$ and $f_{\alpha\beta}$ are the distance and force between atoms α and β , respectively, and Ω^{α} is the atomic volume of atom α . The first term is the kinetic energy contribution and the second term is the pairwise energy contribution. The atomic volume is defined as

$$\Omega = \frac{l_0 \cdot w_0 \cdot t}{N} \quad (4)$$

where l_0 is the original length of the sheet, w_0 is the original width, t is the thickness and is assumed to be the interlayer spacing of graphene in graphite and is 3.35\AA , and N is the total number of atoms. The stress on each atom was computed every 200 time steps and then the average stress over the entire sheet was used in order to obtain a spatial average.

The strain was obtained from the following equation

$$strain = \frac{l - l_0}{l_0} \quad (5)$$

where l is the current length of the deformed sheet and l_0 is the original. Stress-strain curves and snapshots of the fracture modes generated from the MD output are shown in Figure 41. The highest point on the curve was used to determine the failure strength of the sheet.

For some sheets fracture occurred in a slow process and strings or monatomic carbon chains (MACC, or carbyne) formed and would weakly hold the sheet together. The formation of these strings have been shown to appear in other studies as well [43].

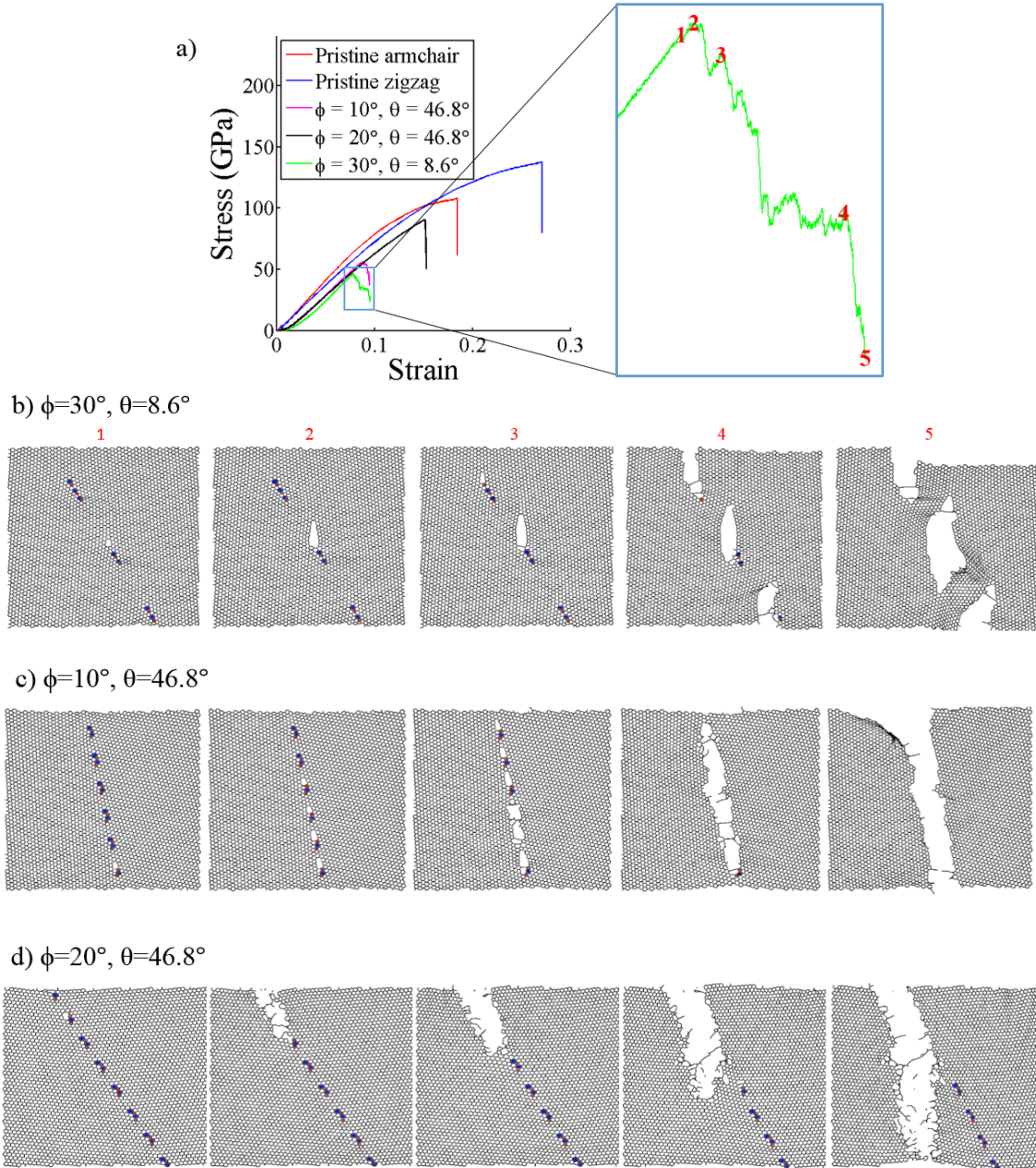


Figure 41. a) Stress vs. strain plots for various graphene sheets. Snapshots of the fracture process for the b) intragranular fracture mode (inset), c) intergranular fracture mode, and d) transition fracture mode.

To determine the critical strain in such cases it was assumed that the critical strain could not be larger than the corresponding strain at a point having a strength of less than 50% of the maximum strength as indicated from the stress strain plot. This was done since the sheet

may not completely fracture, but would remain intact with very large voids, resulting in large strains when the actual failure should be assumed to occur well beforehand.

2.6 Tensile effect from GB misorientation angle and loading angle

To obtain a good estimate of the critical strain and failure strength of the graphene sheets 10 different atomic configurations were simulated for each of the 24 GB misorientation angles and each of the 12 loading angles. An average of the simulations was used for both values. Figure 42 shows the failure strength versus loading angle for all 24 GB misorientation angles.

For the AC GBs shown in Figure 42a the lowest strength always occurs near the 25° loading angle. This is because the first bond that breaks is at the top of the disclination dipole and has the highest stress initially before any tension is applied and at this loading angle the bond is almost parallel to the loading angle. Figure 43 shows this bond and its orientation to the loading angle.

The GB structures in Figure 40 shows that the disclination dipoles in the transition GBs do not follow any pattern as they do in the AC and ZZ GBs. Therefore there is no trend in the failure strength of these GBs as shown in Figure 42b.

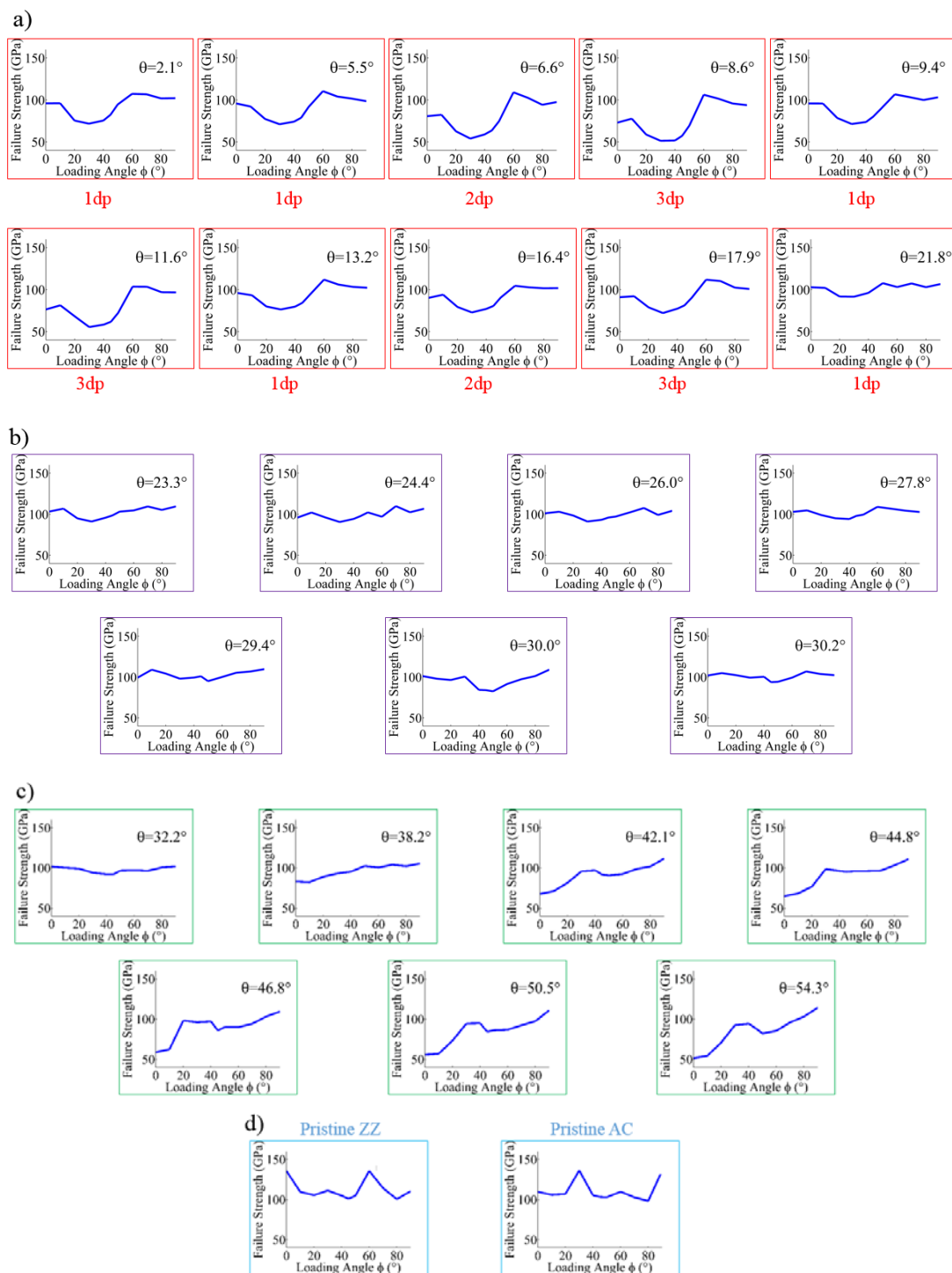


Figure 42. Failure strength vs. loading angle for the a) armchair GBs, b) transition GBs, c) zigzag GBs, and d) pristine sheets.

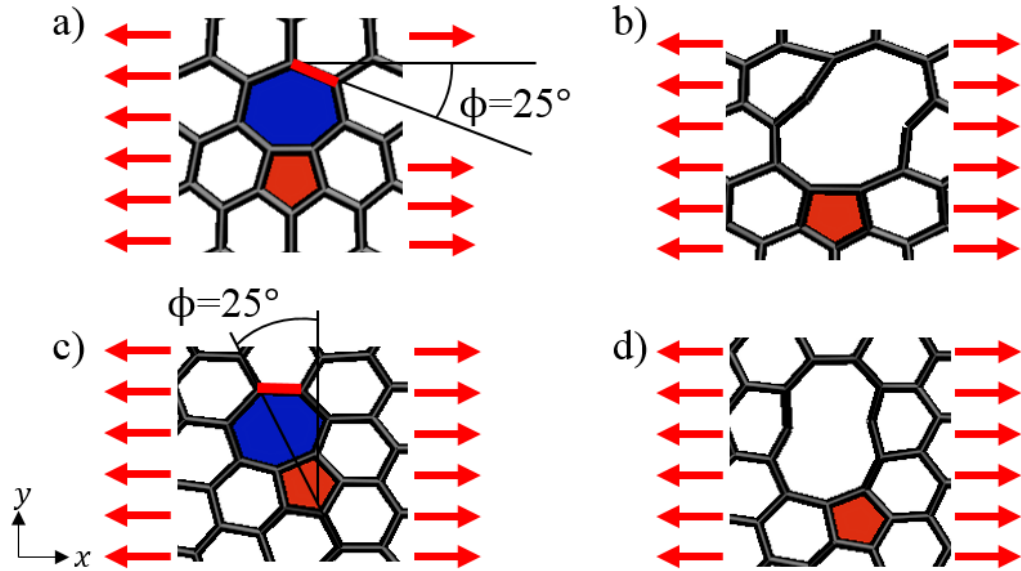


Figure 43. Snapshots of the critical bond breaking in the heptagon ring at the top of the disclination dipole for a) and b) $\phi = 0^\circ$ loading angle, and c) and d) $\phi = 25^\circ$ loading angle. The red line in a) and c) indicate the critical bond which is the bond that breaks first.

For the ZZ GBs the lowest strength is always near the 0° loading angle. This is because the bond with the highest stress initially is also at the top of the disclination dipole cluster and at this loading angle is almost parallel to the loading angle as shown in Figure 44a. Figure 44 shows that when the loading angle is at 50° the critical bond shifts from the top of the disclination dipole to the right since this bond is now the more parallel to the loading angle than the previous critical bond. Figure 42c shows that there is a local minimum in the failure strength near the 50° loading angle when this shift occurs.

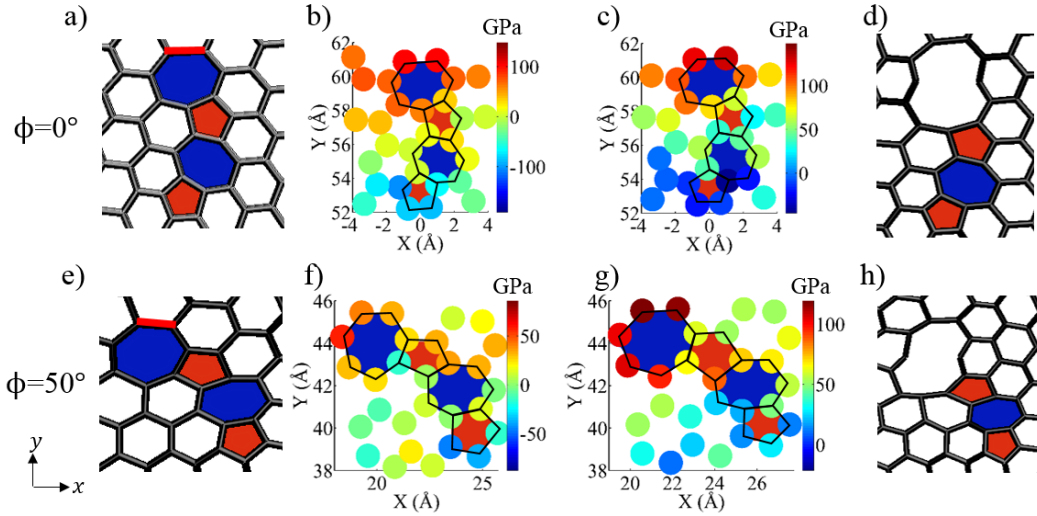


Figure 44. Images of the a) critical bond, b) initial stress, c) stress before fracture, d) broken critical bond for the $\phi = 0^\circ$ loading angle, and e) critical bond, f) initial stress, g) stress before fracture, h) broken critical bond for the $\phi = 50^\circ$ loading angle.

Fracture was shown to initiate at the top of the disclination dipoles where the highest stress occurs and would continue in one of three modes. They were classified as intragranular, occurring within the grain; transitional, occurring partly within the GBs and the grain; and intergranular, occurring within the GBs. Figure 45 shows a map indicating which of these fracture modes occurred for all GBs that were analyzed.

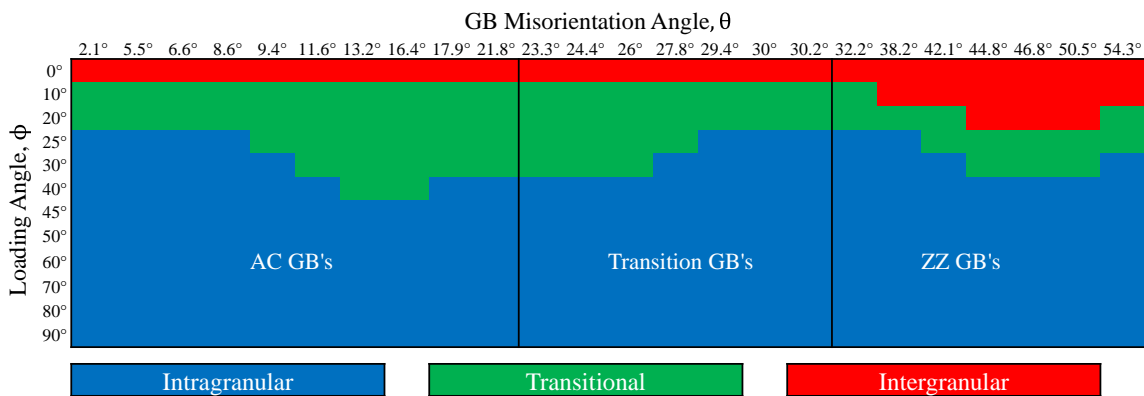


Figure 45. GB fracture mode map in the space of GB misorientation angle, θ , and loading angle, ϕ . Blue region is for intragranular, occurring within the grain; green is transitional, occurring partly within the GB and the grain; and red is intergranular, occurring within the GB.

All of the fracture modes are intergranular for the 0° loading angle. As the loading angle increases the fracture mode changes to a transitional mode and after 40° all fracture modes occur as intragranular cracking. The fracture mode is mainly transitional cracking for the GB misorientation angles that have a high defect density up to the 40° loading angle. This is because it is easy for the cracks that initiate from the defects along the GBs to connect with each other so that fracture propagates along the GBs. This trend is broken however when the zigzag or armchair direction of the lattice of one of the grains approaches a perpendicular alignment with the loading direction. When this occurs it is easy for the crack to propagate along this direction which prevents the cracks from connecting and propagating along the GB and therefore intragranular cracking occurs. For example, for the 30° loading angle and the 42.1° GB misorientation angle the fracture mode is intragranular, but for the same loading angle and 44.8° GB misorientation angle the fracture mode is transitional even though the 44.8° GB misorientation angle has a lower defect density.

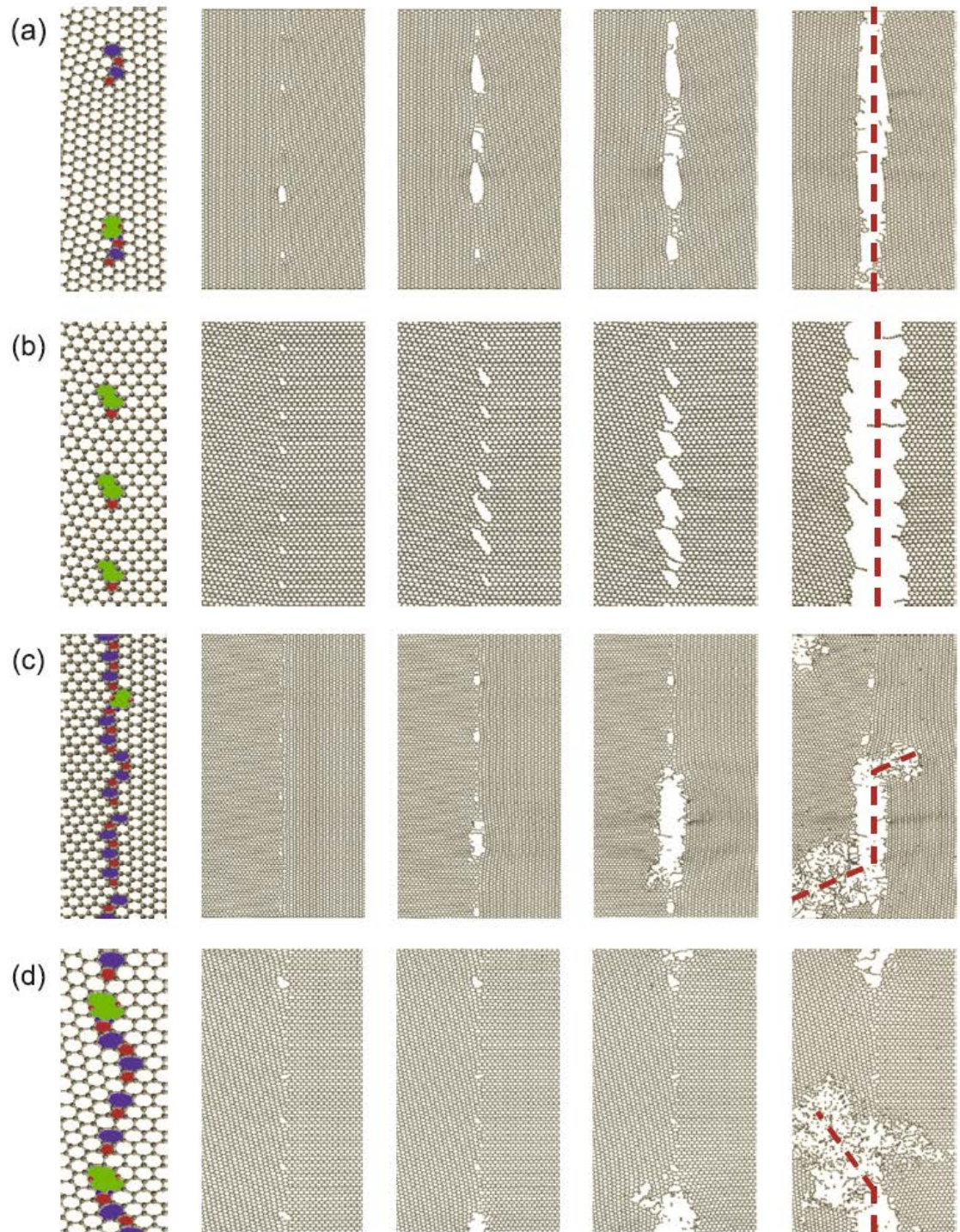


Figure 46. Two different failure types of graphene with GBs (a) and (b) The direction of crack propagation is parallel to the GB (c) and (d) The cracks grow away from the GB. The cracks, pentagons, and heptagons are colored in green, red, and blue, respectively. The red dashed lines represent the torn edges [44].

Figure 46 shows that there can be two types of failure for graphene sheets that contain GB. The type of failure was determined by the arrangement of the defects along the GB. Once initiated cracks grow along the direction perpendicular to the atomic bond with maximum tensile traction. When the defects along the GB follow a periodic arrangement the crack propagates along the GB. However, when the defects follow an irregular or random arrangement the cracks tend to propagate through the grains. Therefore the arrangement of the defects can have an impact on the type of failure mode.

Figure 47 shows a contour plot of the failure strength and critical strain for all GB misorientation angles and loading angles that were analyzed. Both plots follow the same trend that the failure strength and critical strain increase with the loading angle. The local minimum regions where the critical bond becomes parallel to the loading angle can be identified near the 25° loading angle for the AC GBs and 50° loading angle for the ZZ GBs.

Figure 45 shows that the fracture mode for the lower loading angles are either transitional or intergranular. This mode of fracture leads to lower failure strengths, since the cracks easily join and propagate more quickly along the GBs. The MD results in Figure 47 confirms this since higher loading angles have higher failure strengths than the lower loading angles.

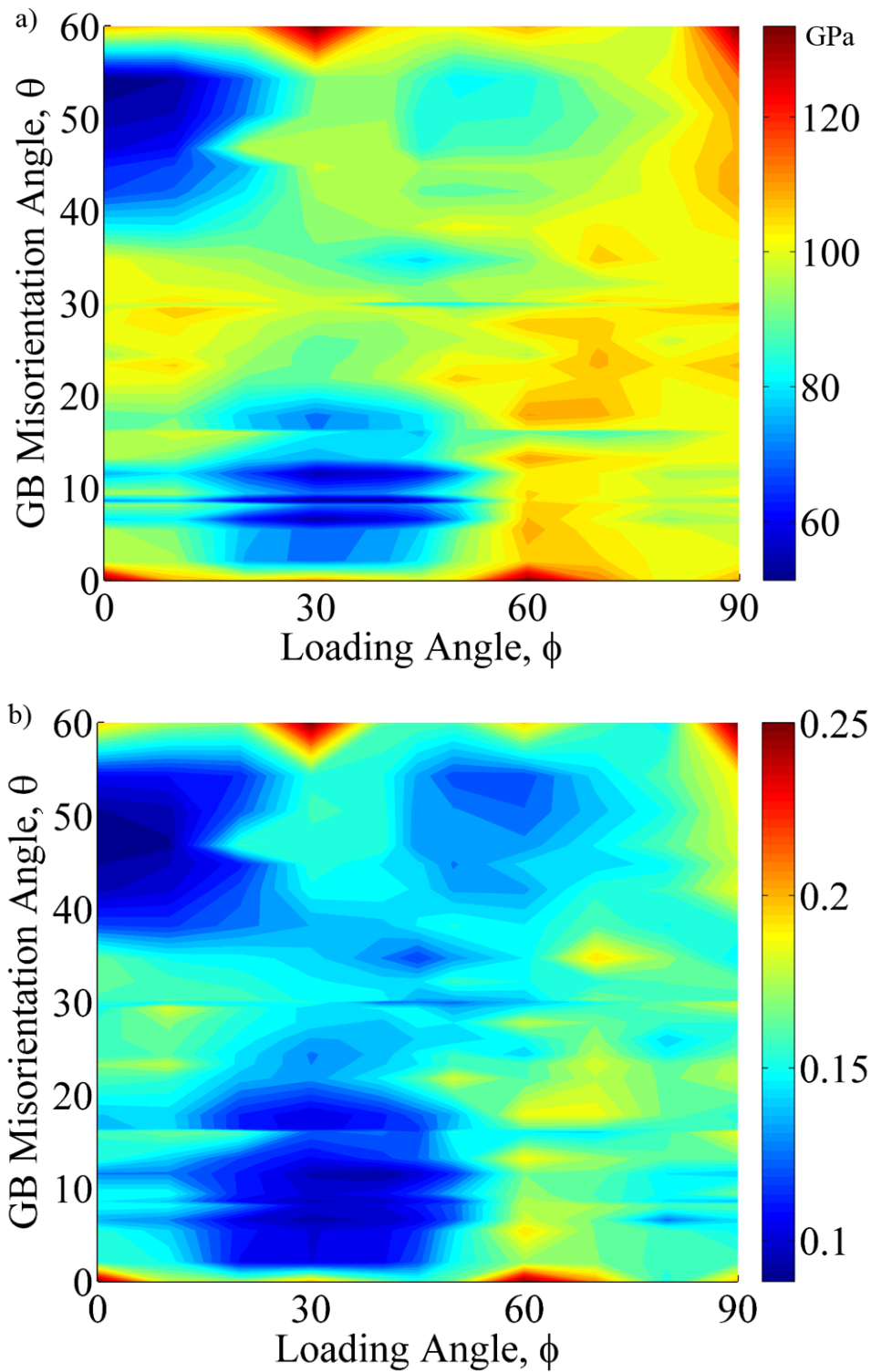


Figure 47. Contour plots of a) failure strength (GPa), and b) critical strain for the sheets of graphene with GBs for the range of all loading angles and GB misorientation angles that were analyzed.

2.7 Continuum theory of tensile response

Failure strength of graphene is dependent on the GB misorientation angle [12, 17, 24, 39] and loading angle and can be explained well by continuum mechanics. The following will show how the stress field around each disclination dipole in these GBs influences the failure strength.

Previous studies [18] have shown that failure is caused by the breaking of the critical bonds with the highest initial stress in the heptagon rings shown in red in Figure 43 and Figure 44. The breaking of these bonds is the point at which the failure strength of graphene is assumed to occur. Figure 48 shows a disclination dipole and its stress field for the x component.

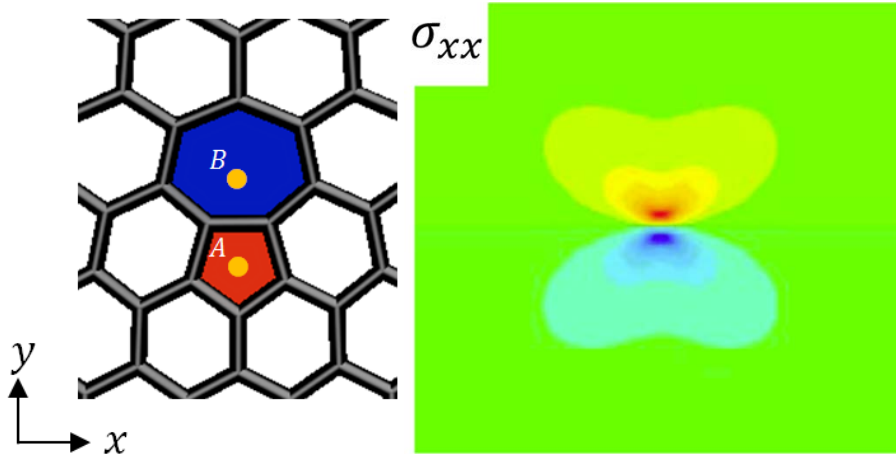


Figure 48. Atomic structure of a disclination dipole and its stress field for the x component [17].

The stress field for the x component is given by the following equation [24, 45]

$$\sigma_{xx} = \frac{E}{12} \left[\ln \left(\frac{r_A}{r_B} \right) + \frac{(y - y_A)^2}{(r_A)^2} - \frac{(y - y_B)^2}{(r_B)^2} \right] \quad (6)$$

where E is Young's Modulus, and $r_A = \sqrt{(x - x_A)^2 + (y - y_A)^2}$, $r_B = \sqrt{(x - x_B)^2 + (y - y_B)^2}$. Figure 49 shows a grain boundary made of a series of periodic disclination dipoles.

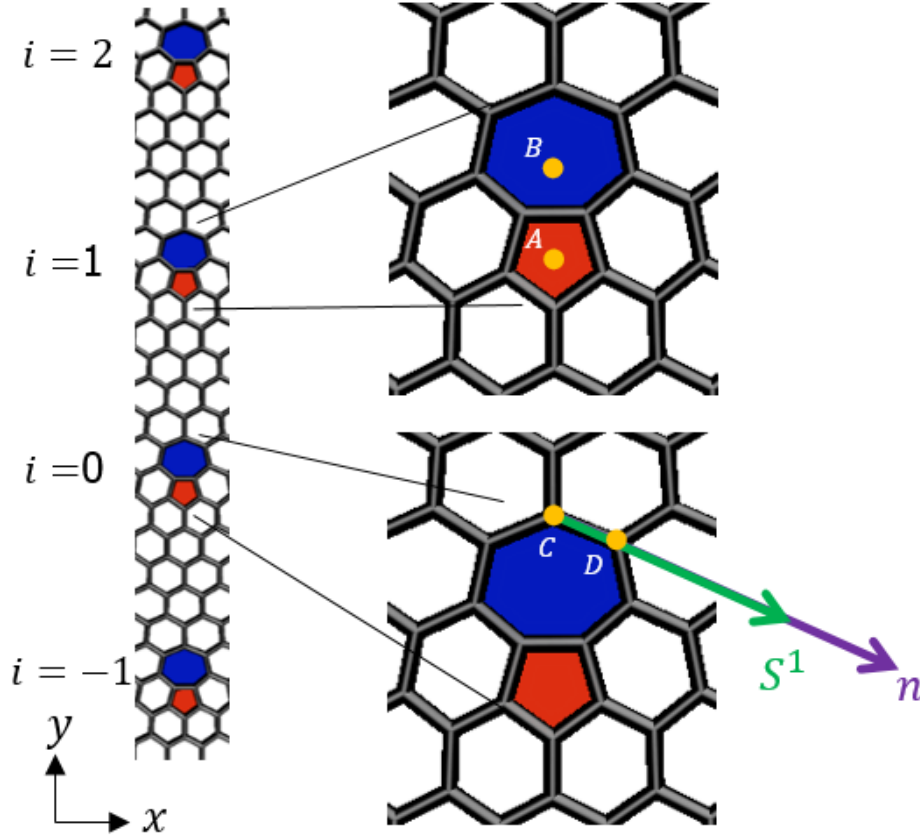


Figure 49. AC GB made of a series of periodic disclination dipoles. The points A and B indicate the location of the dipole that will have its stress field added into the initial stress calculations for the critical bond that is labeled by points C and D. S^1 is the initial stress added to the critical bond from the dipole containing points A and B, and n is the normal vector defining the direction of the critical bond.

All three in plane stress components for one of the disclination dipoles for the GBs shown in Figure 49 are given by the following equations [24, 45].

$$\sigma_{xx}^i = \frac{E}{12} \left[\ln \left(\frac{r_A^i}{r_B^i} \right) + \frac{(y - y_A^i)^2}{(r_A^i)^2} - \frac{(y - y_B^i)^2}{(r_B^i)^2} \right] \quad (7)$$

$$\sigma_{yy}^i = \frac{E}{12} \left[\ln \left(\frac{r_A^i}{r_B^i} \right) + \frac{(x - x_A^i)^2}{(r_A^i)^2} - \frac{(x - x_B^i)^2}{(r_B^i)^2} \right] \quad (8)$$

$$\sigma_{xy}^i = \frac{E}{12} \left[\ln \left(\frac{r_A^i}{r_B^i} \right) + \frac{(x - x_A^i)(y - y_A^i)}{(r_A^i)^2} - \frac{(x - x_B^i)(y - y_B^i)}{(r_B^i)^2} \right] \quad (9)$$

where E is Young's Modulus, and $r_A^i = \sqrt{(x - x_A^i)^2 + (y - y_A^i)^2}$,

$r_B^i = \sqrt{(x - x_B^i)^2 + (y - y_B^i)^2}$. The 2D Cauchy stress tensor is

$$\sigma^i = \begin{bmatrix} \sigma_{xx}^i & \sigma_{xy}^i \\ \sigma_{xy}^i & \sigma_{yy}^i \end{bmatrix} \quad (10)$$

The normal vector, n , defining the direction of the critical bond is

$$n = \begin{bmatrix} n_x \\ n_y \end{bmatrix} \quad (11)$$

The initial tensile stress in the critical bond of the single dipole at $i = 0$ shown in Figure 49 is given as

$$S^i = (\sigma^i \cdot n) \cdot n \quad (12)$$

The direction n of this critical bond is from point C to D and the stress is calculated at point C . The failure strength of graphene composed of a periodic array of these defects is given by the following equation

$$\sigma_T = \sigma_0 - \sum_{i=\pm 1}^{i=\pm \infty} S^i \quad (13)$$

where σ_0 is a fitting parameter and is assumed to be the failure strength of the single disclination dipole at $i = 0$ in an otherwise pristine graphene sheet and $\sum_{i=\pm 1}^{i=\pm \infty} S^i$ is the

superposition of the initial stress contributions from all of the other disclination dipoles in the GB to the critical bond excluding the initial stress from disclination dipole at $i = 0$. The initial stress from the dipole at $i = 0$ is excluded since this stress is assumed to be captured by the fitting parameter σ_0 . To determine the failure strength for the AC GBs the stress components in Eqs. (7), (8), and (9) are used with Eq. (13). To determine the failure strength of a ZZ GBs, as shown in Figure 50, the same method is used except new stress components are needed. The ZZ GBs are composed of a series of periodic defect clusters that are composed of two disclination dipoles as shown in Figure 50.

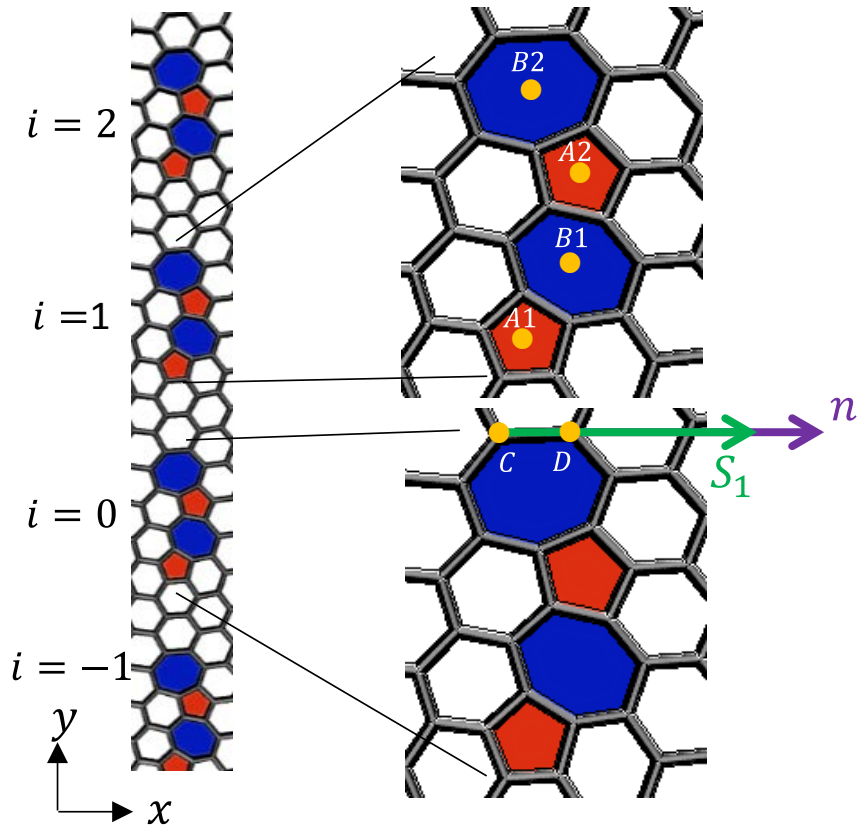


Figure 50. ZZ GB made of a series of periodic disclination dipole clusters. The points A1, B1, A2 and B2 indicate the location of the dipole cluster that will have its stress field added into the initial stress calculations for the critical bond that is labeled by points C and D. S_1 is the initial stress added to the critical bond from the dipole containing points A1, B1, A2 and B2, and n is the normal vector defining the direction of the critical bond.

Therefore the same equations for the stress components from the AC GBs are used except that there are two dipoles in each cluster and they are at an angle to one another. These ZZ GBs stress components are given by

$$\sigma_{xx}^i = \frac{E}{12} \left[\ln \left(\frac{r_{A1}^i}{r_{B1}^i} \right) + \frac{(y-y_{A1}^i)^2}{(r_{A1}^i)^2} - \frac{(y-y_{B1}^i)^2}{(r_{B1}^i)^2} \right] + \frac{E}{12} \left[\ln \left(\frac{r_{A2}^i}{r_{B2}^i} \right) + \frac{(y-y_{A2}^i)^2}{(r_{A2}^i)^2} - \frac{(y-y_{B2}^i)^2}{(r_{B2}^i)^2} \right] \quad (14)$$

$$\sigma_{yy}^i = \frac{E}{12} \left[\ln \left(\frac{r_{A1}^i}{r_{B1}^i} \right) + \frac{(x-x_{A1}^i)^2}{(r_{A1}^i)^2} - \frac{(x-x_{B1}^i)^2}{(r_{B1}^i)^2} \right] + \frac{E}{12} \left[\ln \left(\frac{r_{A2}^i}{r_{B2}^i} \right) + \frac{(x-x_{A2}^i)^2}{(r_{A2}^i)^2} - \frac{(x-x_{B2}^i)^2}{(r_{B2}^i)^2} \right] \quad (15)$$

$$\sigma_{xy}^i = \frac{E}{12} \left[\ln \left(\frac{r_{A1}^i}{r_{B1}^i} \right) + \frac{(x-x_{A1}^i)(y-y_{A1}^i)}{(r_{A1}^i)^2} - \frac{(x-x_{B1}^i)(y-y_{B1}^i)}{(r_{B1}^i)^2} \right] + \frac{E}{12} \left[\ln \left(\frac{r_{A2}^i}{r_{B2}^i} \right) + \frac{(x-x_{A2}^i)(y-y_{A2}^i)}{(r_{A2}^i)^2} - \frac{(x-x_{B2}^i)(y-y_{B2}^i)}{(r_{B2}^i)^2} \right] \quad (16)$$

where $r_{A1}^i = \sqrt{(x-x_{A1}^i)^2 + (y-y_{A1}^i)^2}$, $r_{B1}^i = \sqrt{(x-x_{B1}^i)^2 + (y-y_{B1}^i)^2}$, and $r_{A2}^i = \sqrt{(x-x_{A2}^i)^2 + (y-y_{A2}^i)^2}$, $r_{B2}^i = \sqrt{(x-x_{B2}^i)^2 + (y-y_{B2}^i)^2}$.

The failure strength of graphene with a ZZ GBs is calculated using the stress components in Eqs. (14), (15), (16), and Eq. (13) where σ_0 is now a different fitting parameter and is assumed to be the failure strength of a defect cluster made of the two disclination dipoles at $i = 0$ in Figure 50 and $\sum_{i=\pm 1}^{i=\pm\infty} S^i$ is the sum of the initial stress contributions from all of the other disclination dipoles in the GB to the critical bond excluding the initial stress from the defect cluster at $i = 0$.

The analysis done here is similar to the study shown in Figure 17. The main difference is that the previous study only included the x component of the stress field in the calculations while this study included all three in plane stress components and the resultant stress was calculated along the direction of the critical bonds. Figure 51 shows a comparison of the calculations using all components (solid lines and triangles) to using only the x component

(dotted lines and squares). The results show that there is a significant difference between the two calculations.

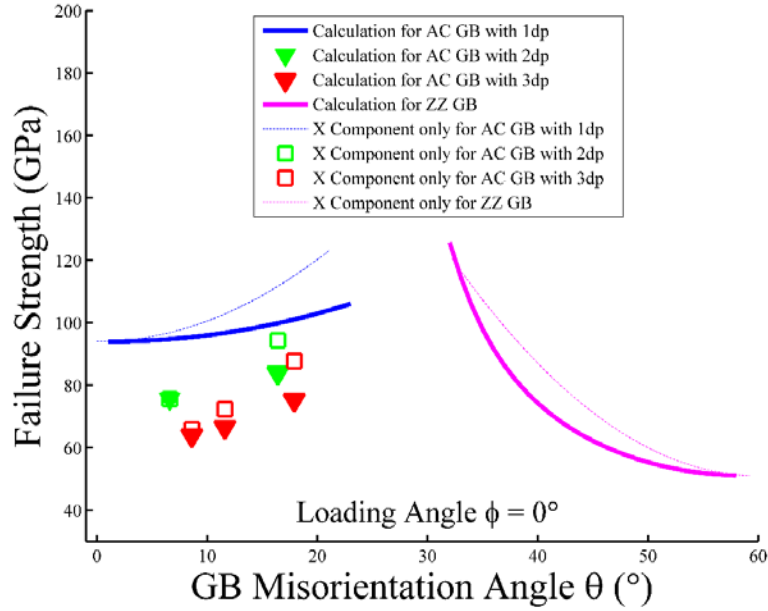


Figure 51. Comparison of GB calculations using all three stress components to only using the x component for the 0° loading angle.

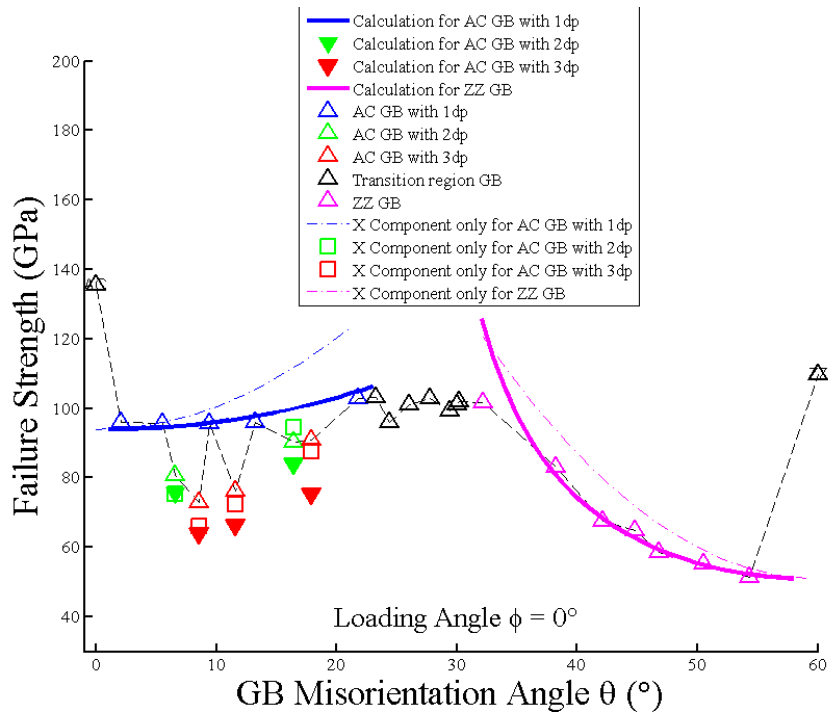


Figure 52. Comparison of all GB calculations with MD results from this paper for the 0° loading angle.

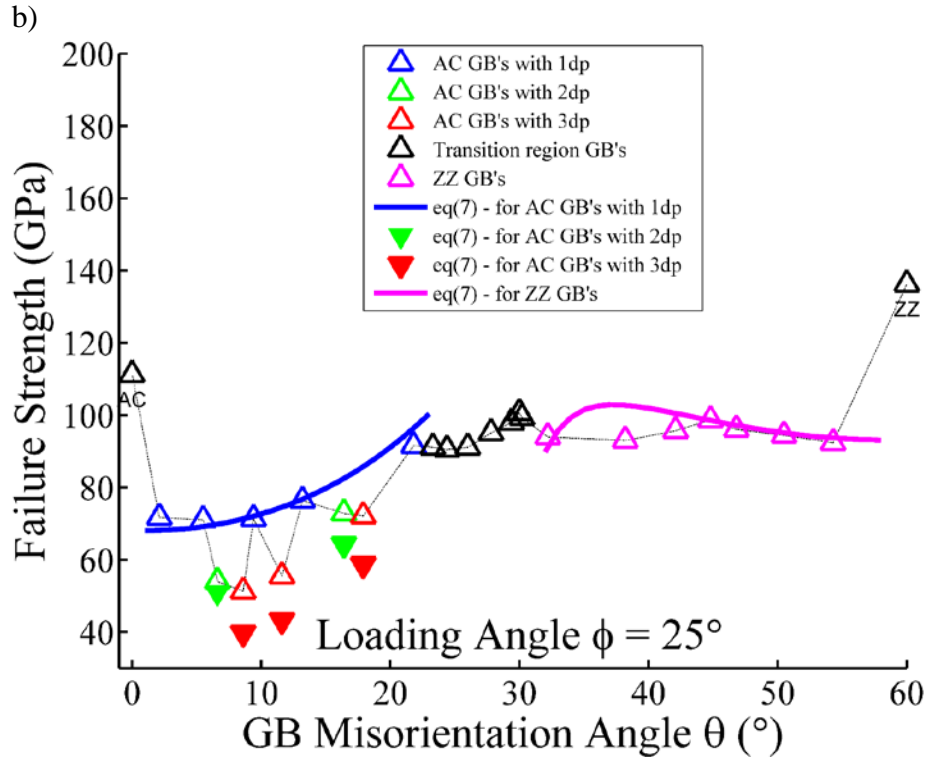
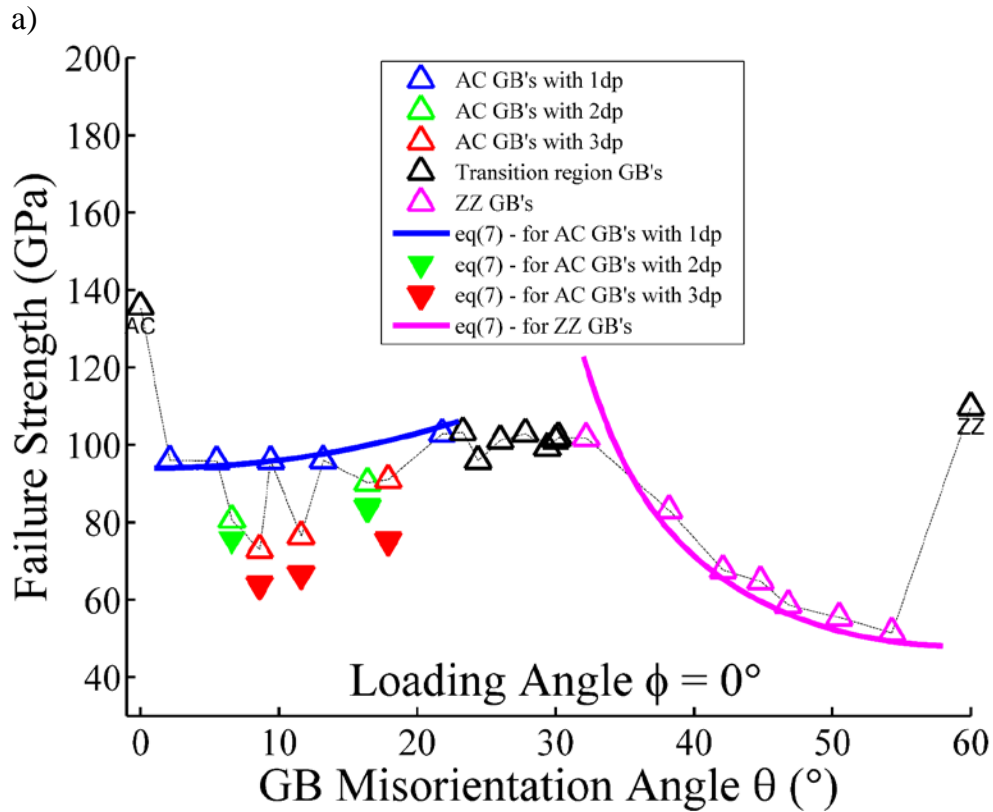


Figure 53. Failure strength vs. GB misorientation angle for the a) 0° loading angle, and b) 25° loading angle.

Although the calculated and MD simulation results match well in Figure 17, a comparison using the MD simulation results for this dissertation show a better fit for the AC and ZZ GBs using Eq. (13), which is shown in Figure 52.

Figure 53 shows results of GB calculations using Eq. (13) compared with results from the MD simulations for the 0° and 25° loading angle. The graphs in Figure 53 shows that the GB calculations and MD simulation results match well. For the AC GBs for the 0° loading angle the point where the stress is evaluated to determine the ultimate failure strength is point C in Figure 49, the normal vector, n , is from point C to D, and the fitting parameter $\sigma_0 = 94$ GPa. For the AC GBs for the 25° loading angle the fitting parameter σ_0 will change since the defect at $i = 0$ is now at a different orientation relative to the tension in the sheet and is $\sigma_0 = 68$ GPa, and the point where the stress is evaluated is now point D in Figure 49. n is evaluated along the same bond except the direction is now rotated 25° . For the AC GBs the 2dp and 3dp GBs have lower failure strengths than the 1dp GBs. This is because the stress contributions from all the disclination dipoles do not contribute as much compressive stress to reduce the initial tension in the critical bond because of their arrangement along the GB. In the calculations no additional variables need to be accounted for when analyzing the 1dp, 2dp, or 3dp AC GBs since the arrangement and location of all of the dipoles are taken into account in the calculations for the stress components in Eqs. (7), (8), and (9). For the ZZ GBs for the 0° loading angle the point where the stress is evaluated to determine the ultimate failure strength is point D in Figure 50, the fitting parameter $\sigma_0 = 51$ GPa, and the normal vector, n , is from point C to D in Figure 50. For the ZZ GBs for the 25° loading angle the fitting parameter σ_0 will again change and is $\sigma_0 = 93$ GPa, and the point where the stress is evaluated is still point D in Figure 50, but the

normal vector is from point D to E in Figure 50, since this is now the bond that is most parallel to the loading direction and is the first to break. For other loading angles the GB calculations and MD simulations results also matched well when using different fitting parameters, σ_0 , and by evaluating the stress at points where the highest initial stress occurs and using a normal vector along the direction of the critical bond.

2.8 MD modeling of failure

The analysis of the graphene sheets in sections 2.2-2.7 dealt with sheets that consisted of a single GB which divided the sheet into only two grains. The fracture analysis done in section 2.8 deals with polycrystalline graphene sheets consisting of multiple GBs and multiple grains.

2.8.1 GB construction

The steps involved in creating polycrystalline graphene used for this analysis proceeds as follows. First a sheet of pristine graphene is generated and its orientation is assigned an arbitrary angle. The sheet is then cut by deleting atoms that are within a given distance along some predetermined GB line. This process is then repeated for each grain in the sheet. Figure 54 shows three grains that are separated by three GBs up to this point.

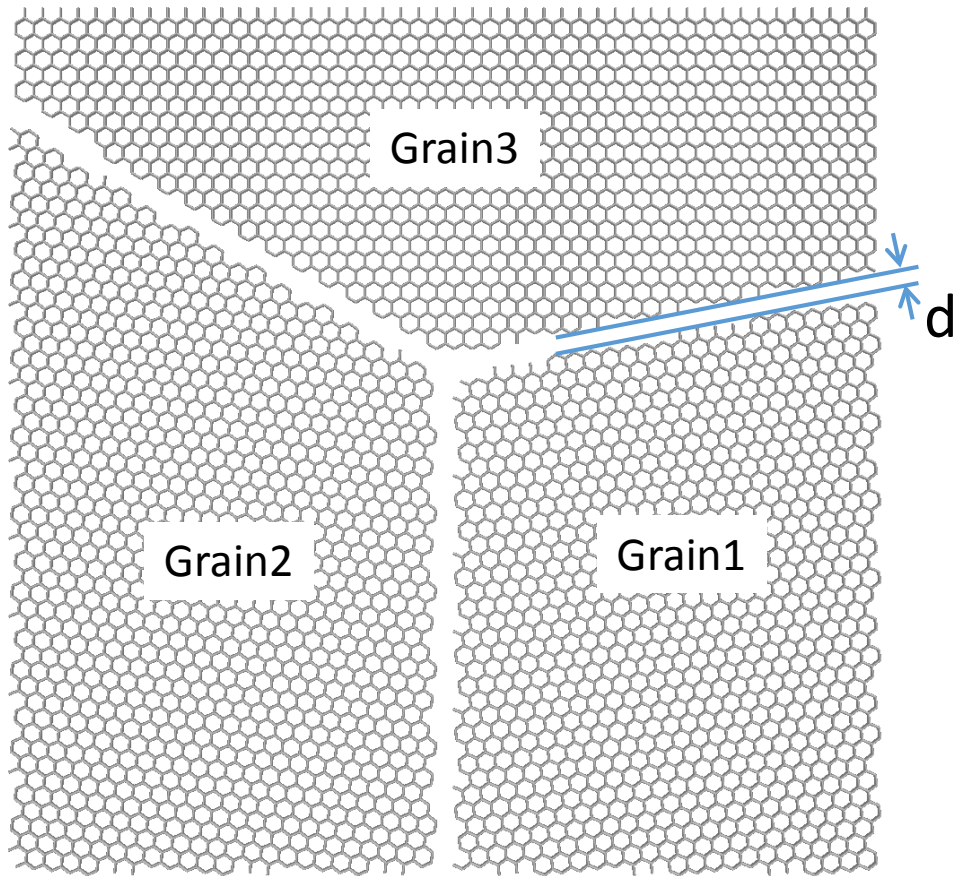


Figure 54. Three grains at arbitrary GB misorientation angles that are used to stitch together a polycrystalline sheet for use in the MD analysis.

From here the distance of all the atoms near the boundary of Grain 1 to the atoms near the boundary of Grain 2 are evaluated. If the distance, d , between two atoms is smaller than some assigned value, for example 1.1\AA , the atom from Grain 1 is deleted. This same process is repeated for Grain 1 to Grain 3 and so on. From here the atom coordinates are used in LAMMPS and an energy minimization is performed so that the atomic bonds between all of the atoms are in their most stable form for the polycrystalline graphene sheet. Figure 55 shows the atomic configuration of a sheet of graphene consisting of three grains before and after energy minimization.

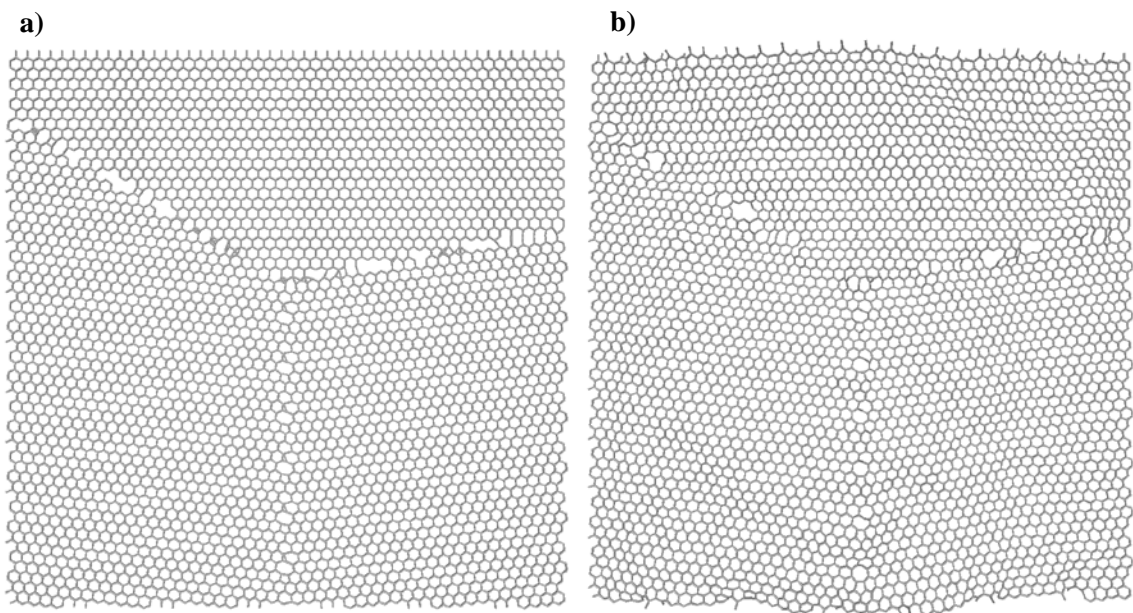


Figure 55. Atomic configuration of a polycrystalline sheet a) before and b) after energy minimization using LAMMPS.

2.8.2 Triple junction

Figure 56 shows graphene where the GBs form a triple junction.

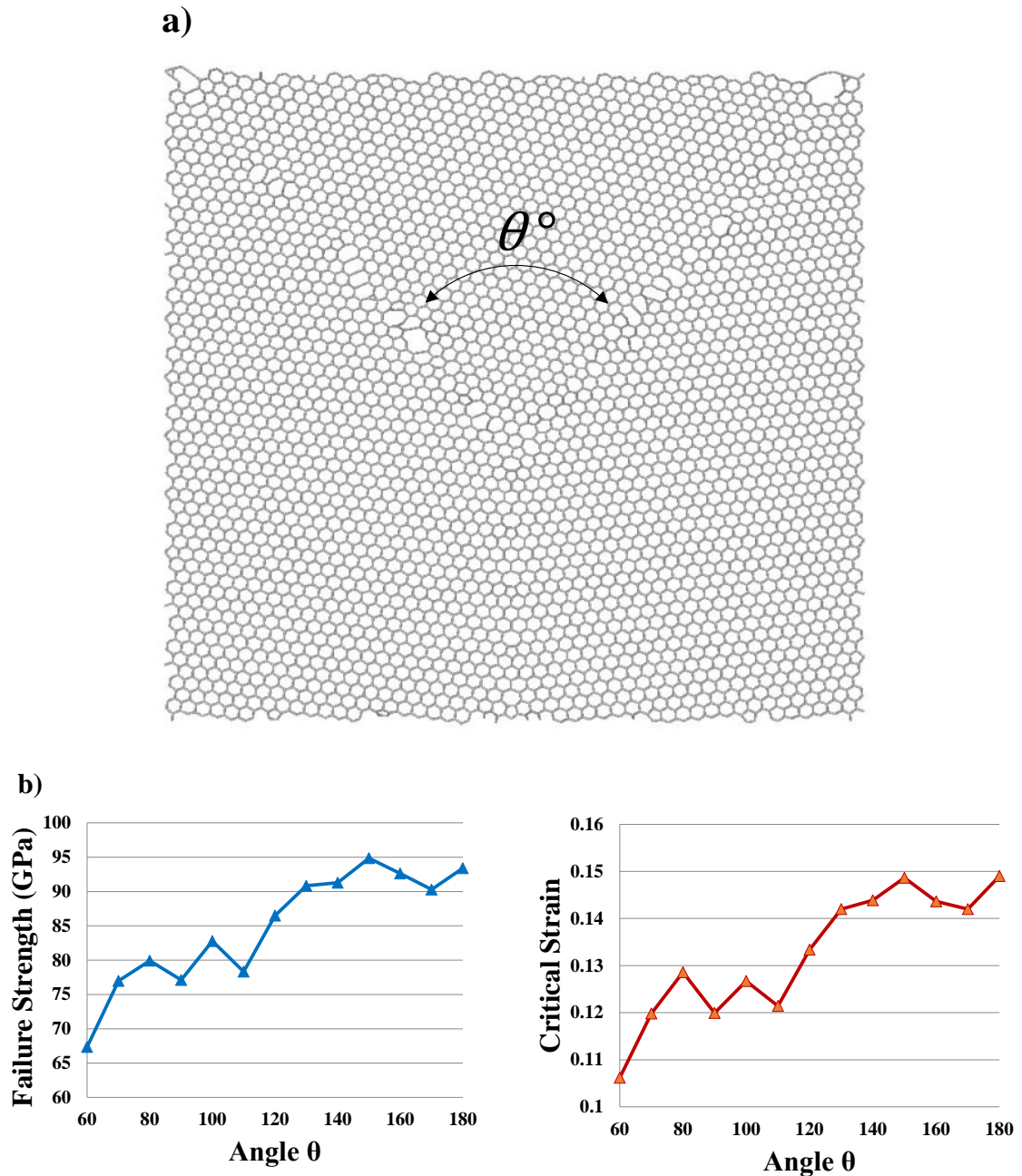


Figure 56. Triple junction analysis a) atomic configuration of graphene with a triple junction, b) Stress-Strain results for triple junction at different angles, θ .

The junction of GBs is where failure is most likely to occur in a polycrystalline sheet and confirmed by previous studies [25, 46]. This effect is enhanced for larger grains [25]. The

results in Figure 56 show an increase in failure strength and critical strain as the angle θ increases, which is expected. The results for the failure strength and critical strain converge to a value of around 95 GPa and 0.15, respectively, as the angle increases. In this study only the angle of the triple junction was controlled and the orientation of each individual grain was at an arbitrary angle. Therefore each of the GBs in the sheets had arbitrary GB misorientation angles. Figure 57 shows the fracture process for a case where it starts at the triple junction and then continues along the bottom GB. The fracture usually starts at the intersection of GBs, but can also occur along the edges or at points along single GBs.

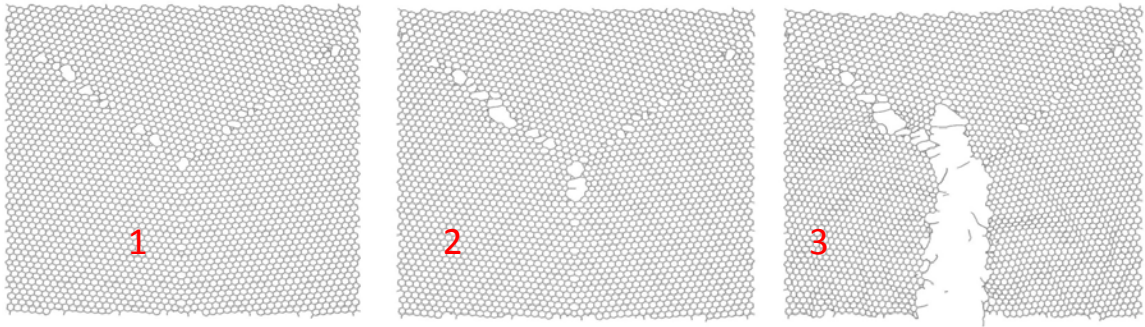
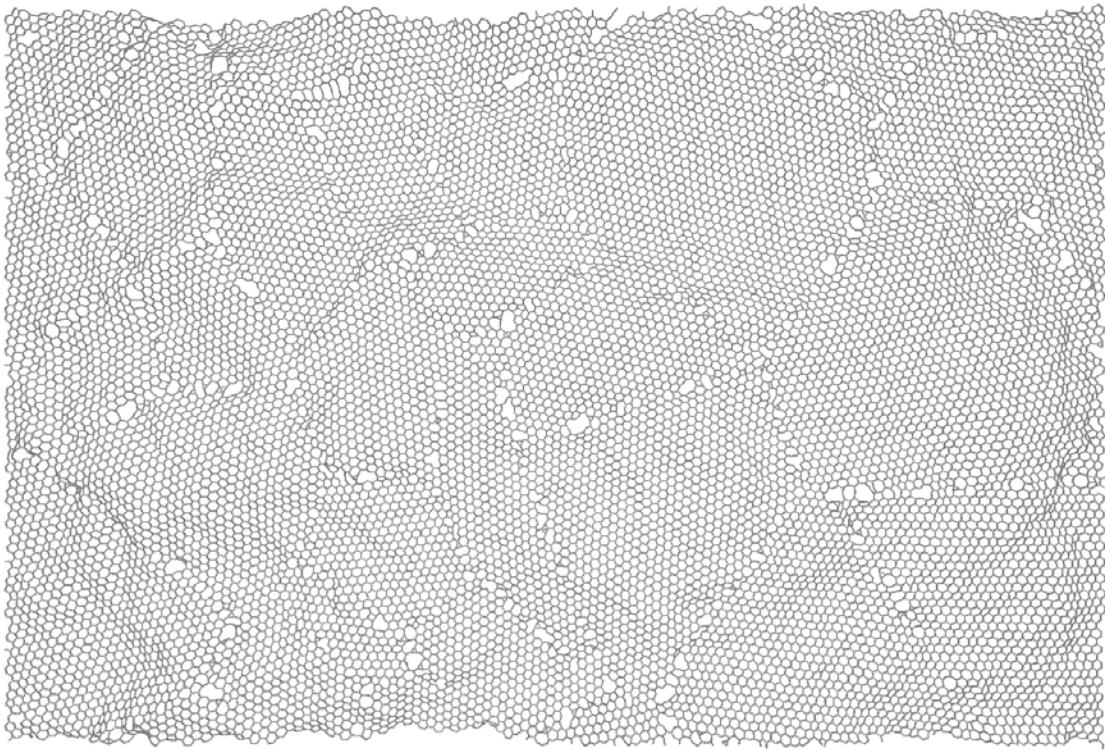


Figure 57. Three snapshots of the usual fracture process of a triple junction showing that fracture starts at the junction.

2.8.3 Different grain size and shapes

a)



b)

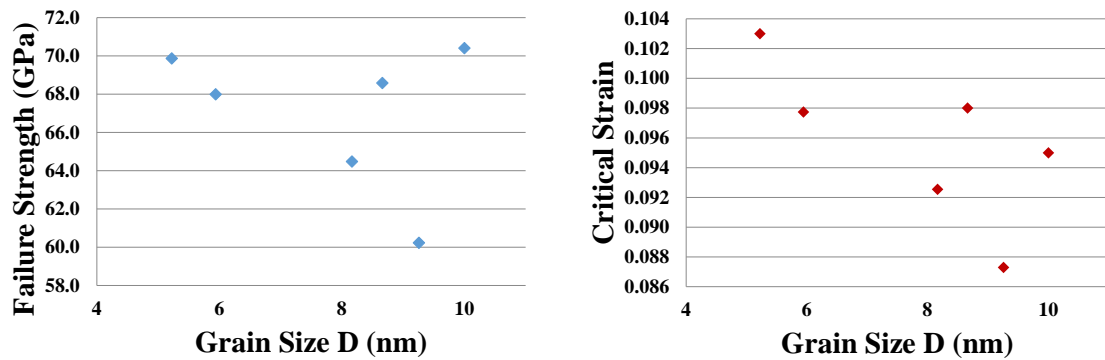


Figure 58. a) Atomic structure of a graphene sheet with an overall size of $30 \text{ nm} \times 20 \text{ nm}$ with arbitrary shaped grains, b) Stress-Strain results for arbitrary shaped grain sheets with different size grains, D.

The fracture of polycrystalline graphene with arbitrary grain shapes and sizes was analyzed. An example of the atomic structure of one of these sheets and the failure strength and critical strain for different grain sizes is shown in Figure 58. These arbitrary grains shapes were generated by using a built in Voronoi algorithm in Matlab. The algorithm generates a given number of points at random locations within a specified area and then each point is connected to its nearest neighbor to form an edge of a grain. The average grain size was determined by dividing the area of the sheet by the number of grains that are generated. This results in an average area per grain. Assuming each grain was square, the length of a side was used as the average grain size. These fracture results are similar to the results of the study [22] on polycrystalline sheets with arbitrary grain shapes discussed in the overview. For both studies the failure strength of these sheets are independent of the grain size. However only one simulation for each point was used for the graph in Figure 58 for the failure strength vs. grain size since the sheets were large and the simulation time was very long. In addition to this each sheet used a completely different grain pattern and only the average grain size for the sheet was used when plotting the results for the failure strength of each sheet. These are a couple of reasons for the wide variation in failure strength vs. grain size and no trend was found. Again for both studies there was a size dependence for the failure strain as a function of the grain size which showed an increase in critical strain as the grain size decreased. The main difference between these sheets and the sheets from the study [22] in the overview is the way the grains were stitched together. Large voids and very wide grain boundaries were generated in [22] as shown in Figure 59.

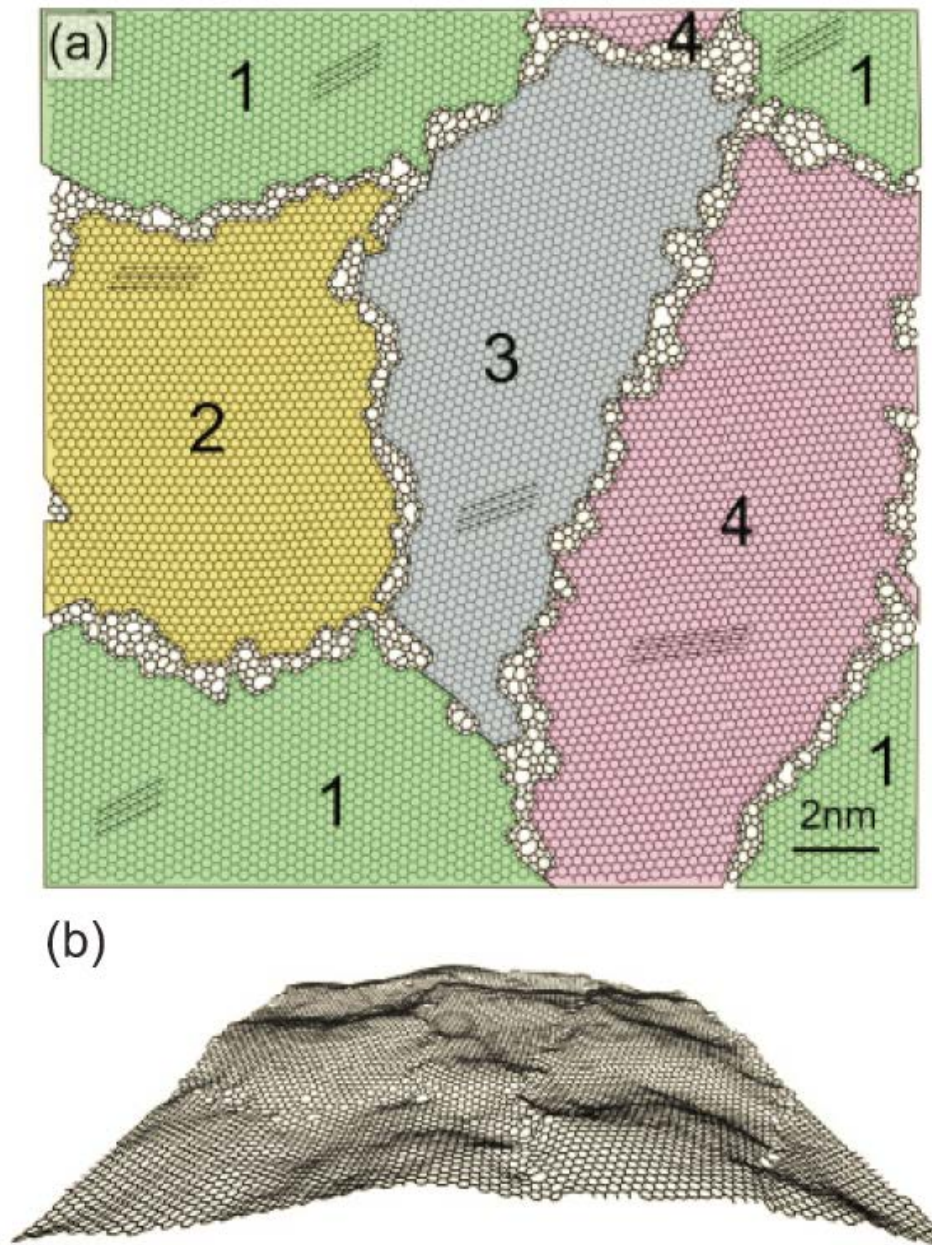


Figure 59. Atomic structure for polycrystalline graphene with periodic BC's. a) top view b) side view of a 20 nm \times 20 nm graphene sheet with four grains, as marked by the numbered shaded areas. Lines indicate the orientations of the graphene lattice within each grain [22].

For the analysis done for this dissertation there were still voids but the sheets were generated in a way so that the grain boundaries were not as wide, which is what has been

shown by most grain boundaries from experimental results from the literature. However the results of the two studies were similar.

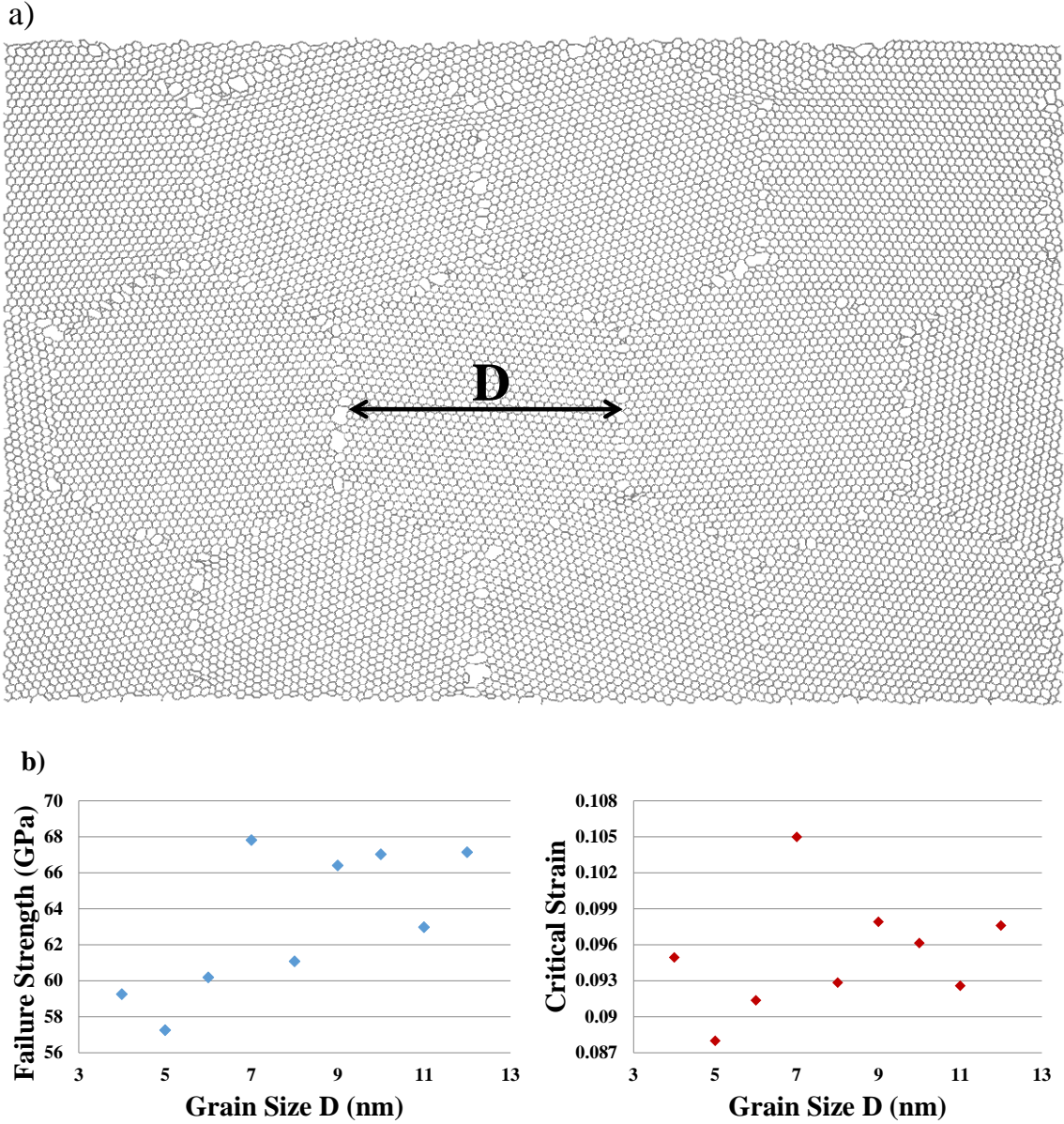


Figure 60. a) Atomic structure of a graphene sheet with an overall size of $30 \text{ nm} \times 20 \text{ nm}$ with hexagonal grains, b) Stress-Strain results for hexagonal grain sheets with different size grains, D .

Figure 60 shows the results of failure strength and critical strain for graphene made of hexagonal grains. These results show a slight increase in failure strength with the grain size. There is no clear trend for the critical strain shown in Figure 60. For the previous study [25] shown in the overview on polycrystalline sheets with hexagonal grains it was also found that as the grain size increased there was a smaller failure strength. This is in contrast to the independence of failure strength on grain size for arbitrary shaped grains from this dissertation and the previous study [22], which however did not consist of idealized GBs and also included large voids.

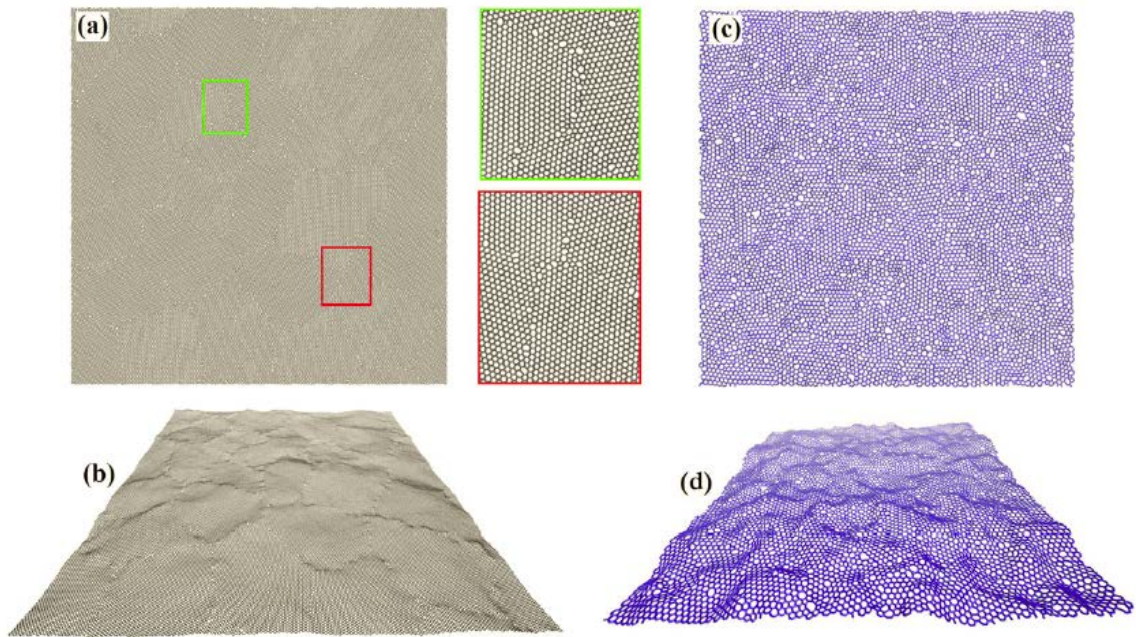


Figure 61. Atomic structure of polycrystalline graphene sheets. a) top view b) side view of a periodic $50\text{nm} \times 50\text{nm}$ polycrystalline graphene sheet with an average grain size of 10nm consisting of 25 grains; c) top view d) side view of a periodic $20\text{nm} \times 20\text{nm}$ polycrystalline graphene sheet with an average grain size of 1nm including 400 grains [47].

The trend of increasing failure strength with increasing grain size was also determined from a previous study [47] that looked at arbitrary shaped grains with sizes ranging from 1-10nm. The atomic structure of the sheets from [47] are shown in Figure 61. This is in contrast to the independence of failure strength on grain size for arbitrary shaped grains done for this dissertation and the previous one [22] from the overview. However in [47] it was found that larger strain occurs for smaller grain sizes, which is in agreement with results from Figure 58 and the study [22] from the overview for arbitrary shaped grains.

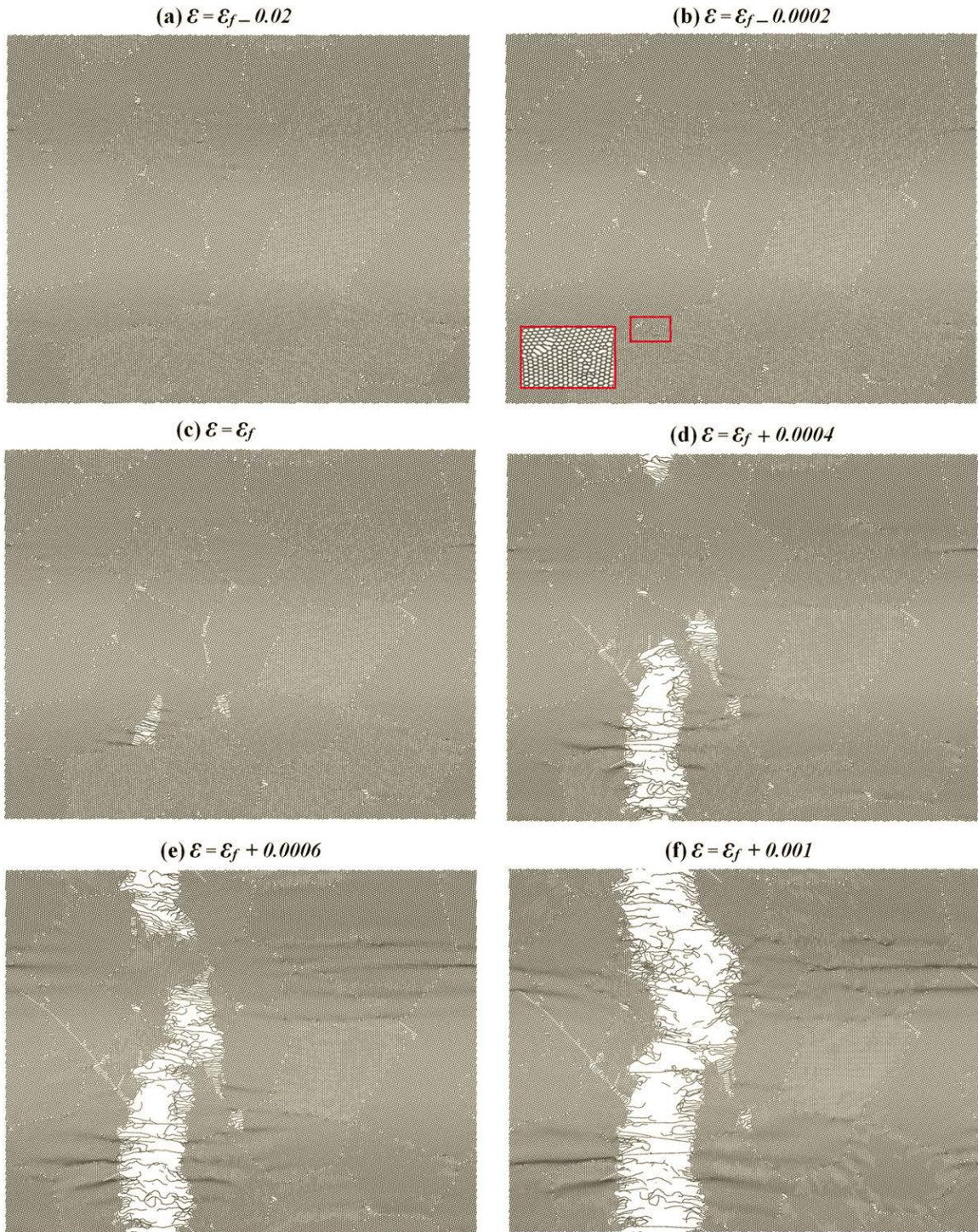


Figure 62. Deformation process of a polycrystalline graphene sheet with arbitrary grain shapes and an average grain size of 10 nm. (ϵ and ϵ_f represent current strain and failure strain, respectively). (b) Inset shows pre-existing cracks at the GBs. (c) The coalescence of existing cracks at one of the GBs. This leads to a large drop in stress-strain curve and the point where ultimate failure strength is defined [47].

Figure 62 show the fracture process for the arbitrary shaped grains that were analyzed in [47]. The fracture process shows that monoatomic chains develop as a result of the applied load. The ultimate failure strength is determined when existing cracks in the GBs begin to coalesce and the monoatomic bonds begin to break. A steep drop in the stress-strain curve as observed at this point. The results from the sheets with other grain sizes showed that for smaller grain sizes the ultimate failure strength of the sheets were reduced. An increase in the defect concentration with smaller grain sizes makes it more probable for the cracks to coalesce and leads to a lower ultimate failure strength.

It was shown that the critical strain increases as the grain size decreases for most studies that were investigated. One reason for this is that smaller grains lead to a more homogeneous structure which allows it to flow more uniformly during loading conditions. However there was no clear relationship on the failure strength of polycrystalline graphene with different grain shapes and sizes. One of the explanations for this is that the process of failure for these sheets are hard to predict when there are many grain boundaries. The failure process usually starts at a junction where the grain boundaries meet as shown in Figure 63, but this is not always the case.

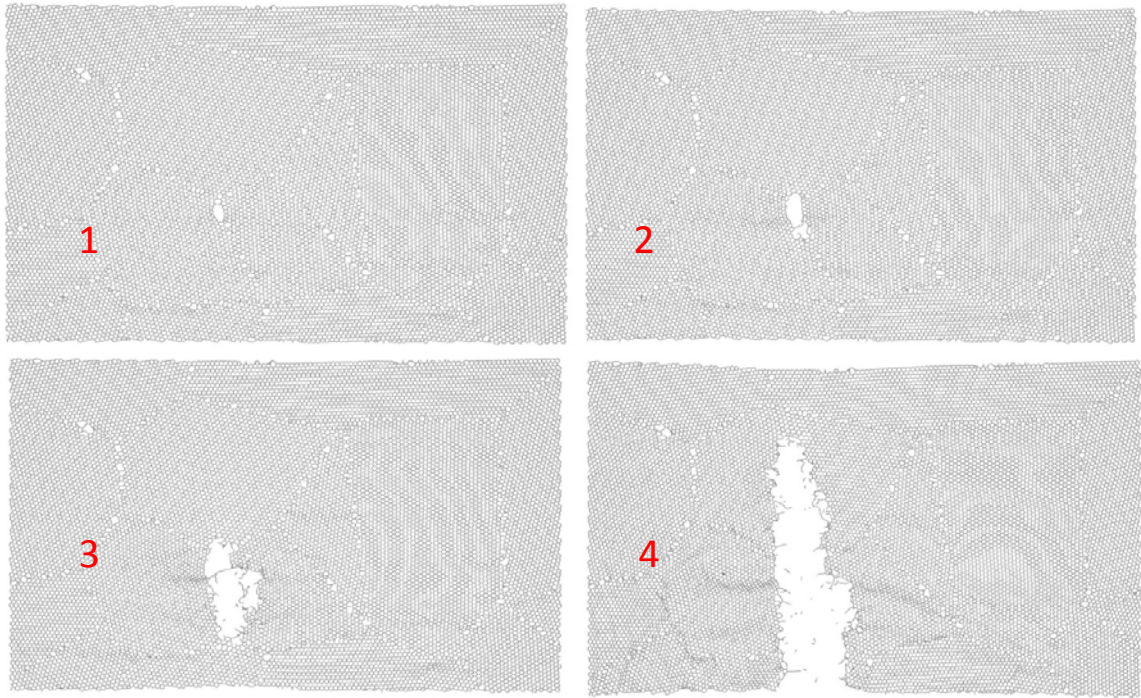


Figure 63. Four Fracture snapshots of the fracture of graphene with arbitrary shaped grains where the failure process starts inside the sheet at a point where the grain boundaries meet.

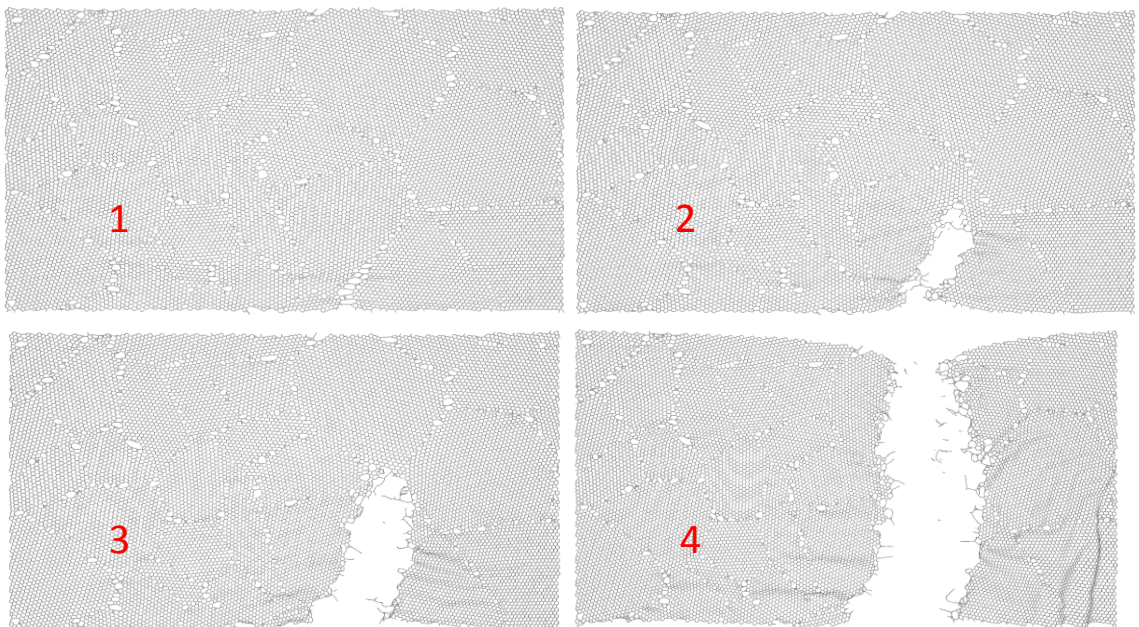


Figure 64. Four Fracture snapshots of the fracture of graphene with arbitrary shaped grains where the failure process starts at the edge of the sheet.

Sometimes the failure may start at the edge of the sheet as shown in Figure 64, or even at some point within a single grain boundary. These studies on sheets with different grain arrangements and sizes give insight into the complexities of how GBs effect the failure strength of graphene.

2.9 Conclusion

It was shown that GBs in graphene can significantly reduce its mechanical properties such as ultimate failure strength and critical strain. MD simulations for pristine graphene showed its ultimate failure strength can be as high as 130 GPa. When GBs are present this value will be reduced to 40-105 GPa depending on the GB misorientation angle and loading angle. These MD results are in good agreement with experimental results [8-11] where the failure strength of polycrystalline graphene with multiple GBs and single GBs were reported to be close to the failure strength of pristine graphene [10, 11] or as low as 35 GPa [9]. In experiments it was also determined that an increase in the GB misorientation angle led to an increase in failure strength. As the GB misorientation angle increased from 0° to 30° the failure strength increased from 53-94 GPa [11]. This is also in agreement with MD results where an increase in the GB misorientation angle for the AC GBs from 0° to 30° led to a similar increase in failure strength. Cracks tend to form at the tops of the disclination dipoles where the initial stress in the critical bond is the highest. The arrangement of these defects along the GB has a significant effect on how much initial stress is in these critical bonds. The breaking of these critical bonds is the point at which the failure strength of graphene occurs. Many studies done before looked at varying the GB misorientation angle, but by also varying the loading angle it was determined there

were critical loading angles that have a significant effect on the ultimate failure strength of graphene. These loading angles are at orientations where one of the critical bonds in the top of the disclination dipoles become parallel to the applied tensile load. This occurs at the 25° loading angle where all of the AC GBs have their lowest failure strength and the 0° loading angle for the ZZ GBs.

A continuum model was developed to approximate the failure strength of graphene containing GBs with different loading angles. It was shown that the model's results matched well with the results obtained from the MD simulations and were an improvement on calculations done previously [17] to predict the failure strength of graphene. This analysis could help to improve the failure strength of polycrystalline graphene by controlling the defect arrangement through irradiation for applications like flexible electronics.

For the MD fracture analysis it was shown that the fracture in graphene with GBs usually first starts at triple junctions. For the analysis done on triple junctions it was shown that as the angle θ increases the failure strength and strain are also increased. Therefore devices that require higher failure strength and strain should try to use patterns of GBs where the angle θ of all the triple junctions are as high as they can be. One example would be a sheet that contained just square regions made from GBs.

Most studies showed an increase in critical strain as the grain size decreased. An explanation for this is smaller grains lead to a more homogeneous structure which allows it to flow more uniformly during loading conditions.

For the MD fracture analysis for the sheets with multiple grains and different grain shapes and sizes it was shown that there can be significant differences in the failure strength. One

explanation for this is the BC's that are used. The MD analysis used for this dissertation used non-periodic BC's while another study [47] used periodic BC's. When using non-periodic BC's the top and bottom edges of the sheets are free. These edges are mostly along energetically unfavorable directions, since it was shown [26] that graphene tends to tear along either the AC or ZZ directions. This is a possible explanation for some of the variance in results and stability issues for some of the simulations where they would end with errors. Another explanation is that while the fracture usually starts at the junction of the GBs, for large sheets with multiple GBs it was shown that the fracture can also start at other locations like the edge of the sheet or points within a single GB. The way that LAMMPS performs the MD calculations may also be a reason for the difference in results. In some cases it was found that two MD simulations with the exact same inputs would not always produce the same type of fracture. This may be because LAMMPS assigns the initial velocities of the atoms in a random way.

Chapter 3: Effect of GBs on thermal behavior of graphene

Graphene is known to have one of the highest thermal conductivities of any material. For suspended single layer graphene the room temperature thermal conductivity was measured as 5300W/mK using Raman microscopy [4]. The thermal conductivity of single layer graphene supported on silicon dioxide is still as high as about 600W/mK [48] near room temperature, exceeding those of metals such as Cu. Heat removal has become an important issue owing to higher levels of dissipated power density and speed of electronic circuits [49]. Therefore it is important to understand more about the heat transport in graphene since it could be used to improve devices that need a way to dissipate heat in the best possible way.

3.1 Overview

This section contains an overview of the previous studies from the literature that have been conducted on the thermal properties of graphene with GBs. One note to mention is the large differences in published results have been obtained for the thermal conductivities of graphene using MD. This can be attributed to the different potentials, sheet sizes, boundary conditions, defects in sheets, etc.

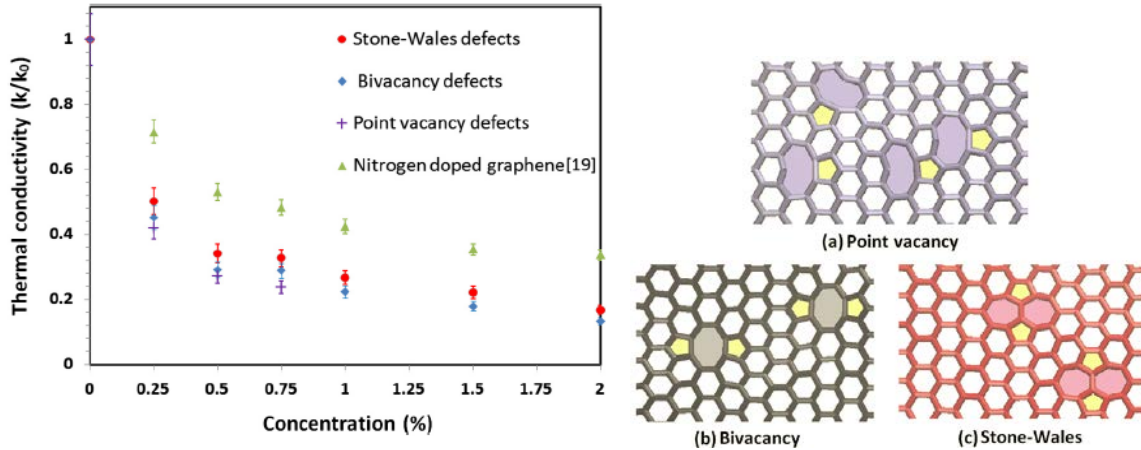


Figure 65. Normalized thermal conductivity of graphene as a function of various defect concentrations [30].

Figure 65 shows the effect of various defects concentrations on the thermal conductivity of graphene. Concentration is defined by the ratio of removed (in point vacancy and bivacancy defects) or rotated (in Stone–Wales defects) atoms to the total number of available atoms in a defect free graphene structure. The results show an exponential trend in the reduction of graphene thermal conductivity as the defect concentration increases [30]. The thermal conductivity was found to increase slightly in another study [50] for increasing temperatures and for higher defect densities there was less variation in thermal conductivity as the temperatures varied.

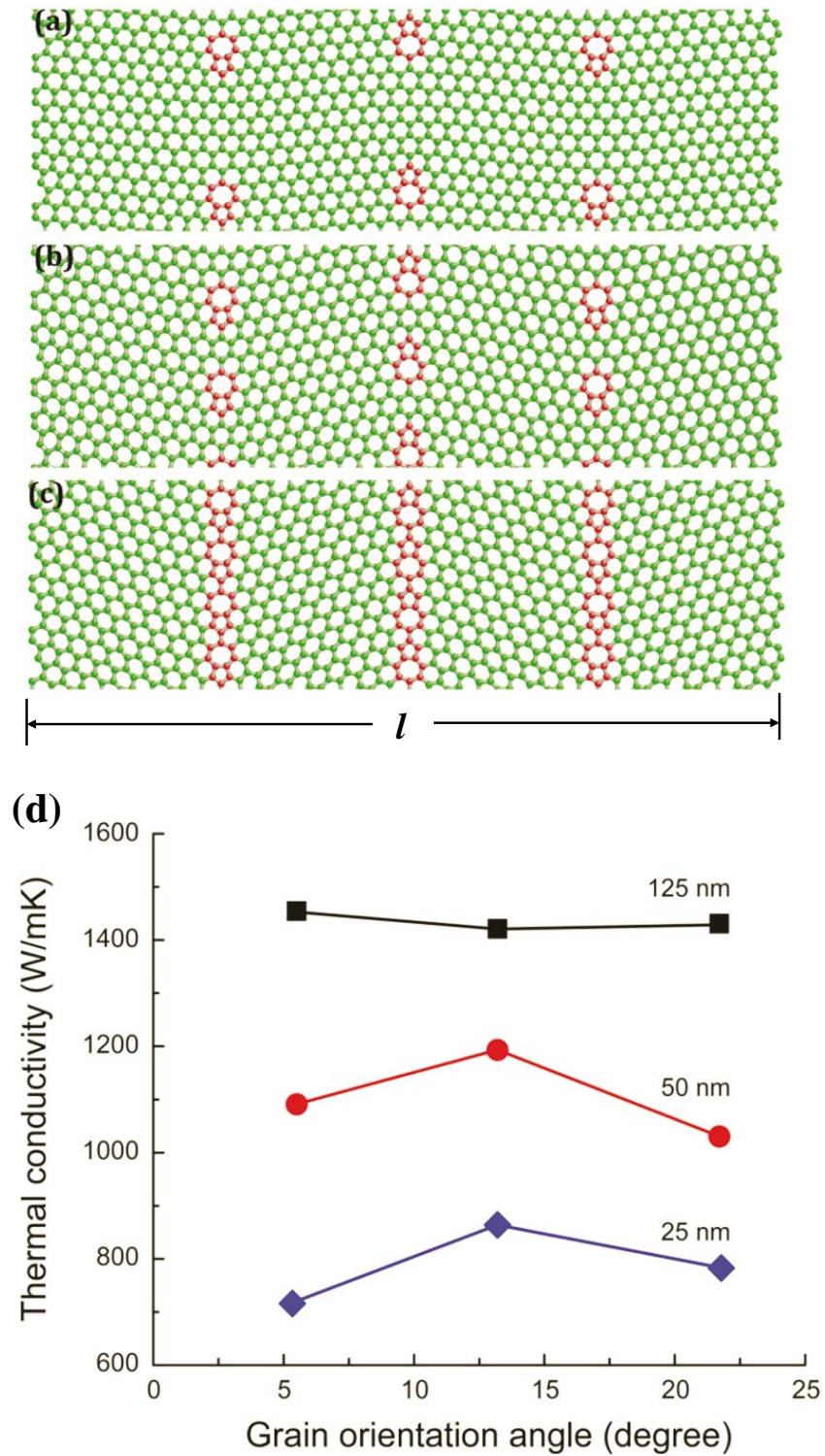


Figure 66. (a)-(c) Graphene of different sheet lengths ($l = 25, 50, \text{ and } 125 \text{ nm}$) (d) thermal conductivity as a function of GB misorientation angle (a) 5.5° , (b) 13.2° , and (c) 21.7° [51].

Figure 66 shows the thermal conductivity of graphene sheets of different lengths as a function of GB misorientation angle. The results show thermal conductivity increases with the length, but there is a weak dependence on thermal conductivity for the three different GB misorientation angles that were analyzed.

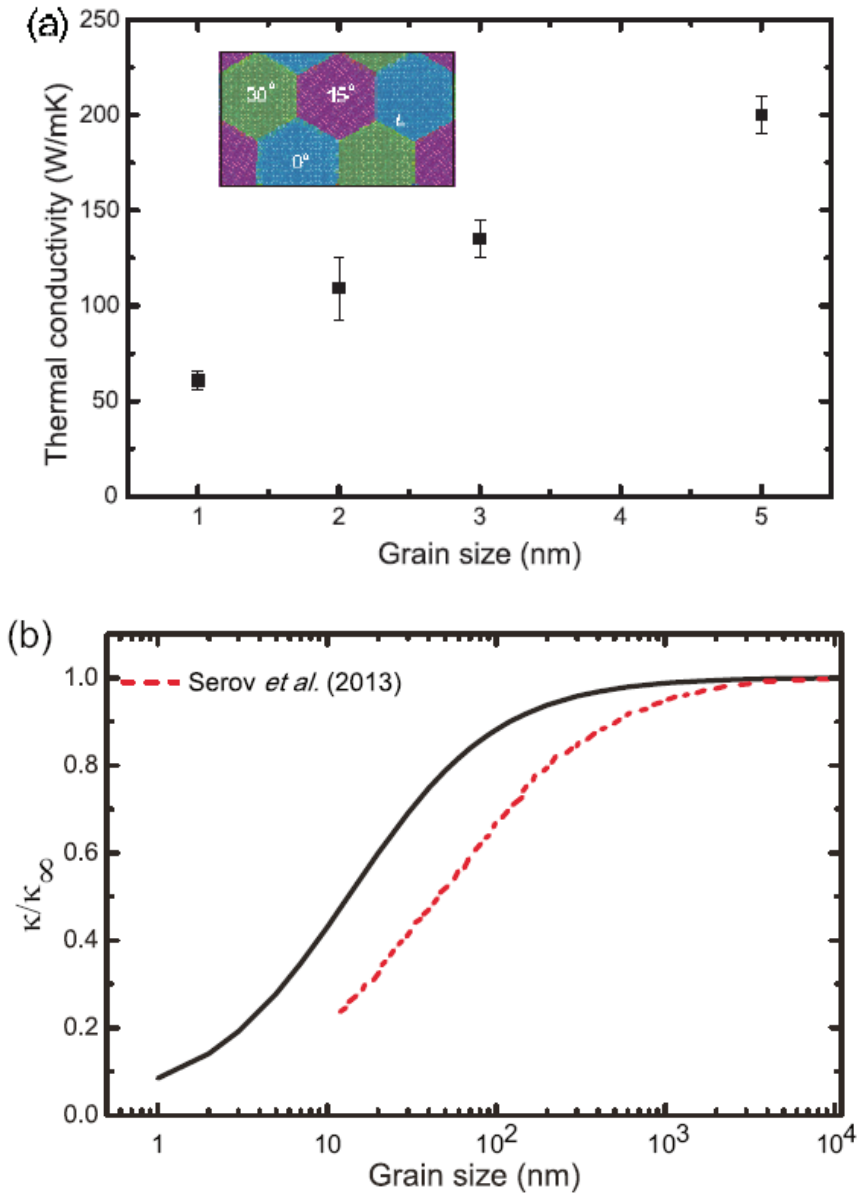


Figure 67. (a) Thermal conductivity, κ , of polycrystalline graphene as a function of grain size, L (b) Predicted κ , normalized by κ for pristine graphene (red dashed line is data taken from Serov et al. 2013) [52].

Figure 67 shows the thermal conductivity increases with the grain size for polycrystalline sheets with hexagonal grains. Based on the study, which included the grain size and fraction of graphene that was considered a GB region, the thermal conductivity of polycrystalline graphene converges to 720 W/mK as the grain size increases to a few microns [52], which is close to the thermal conductivity of pristine graphene supported on a substrate.

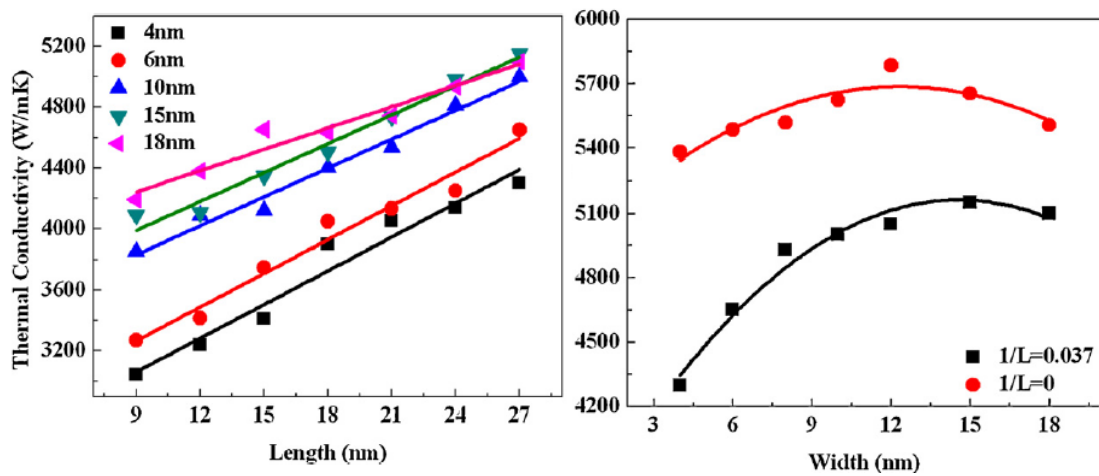


Figure 68. Length and width dependence of graphene sheets on thermal conductivity [53].

Figure 68 displays the dependence of thermal conductivity from length and ribbon width of graphene nano-ribbons (GNRs.) When the ribbon length is smaller than the phonon mean free path, 775 nm in graphene, Umklapp (phonon-phonon) scattering among phonons is negligible, and the collision of phonons at the edge dominates the scattering, which reduces the thermal conductivity. The shorter the ribbons are the stronger the edge scattering is and therefore the thermal conductivity is reduced. For narrower GNRs, the boundary scattering at the long edges are dominant, which also leads to a reduction in thermal conductivity. In Figure 68 it can be seen that the thermal conductivity increases with the width at first to a width of about 15 nm and then decreases. The boundary

scattering will be weakened with increasing ribbon width. However, the increased number of phonons and the smaller energy separation between phonon modes increase the probability of Umklapp scattering for wider GNRs. These two mechanisms compete to determine the thermal conductivity [53]. However another study [54] indicated that the thermal conductivity always continues to increase with the width.

The width of the graphene sheet is not important when using periodic BC's. For example one study [54] chose 5.2 nm for the width. Additional simulations with double width produced the same thermal conductivity. Thus, the variation of width with periodic BC's does not change the thermal conductivity of graphene and 5.2 nm is large enough to model infinitely wide graphene.

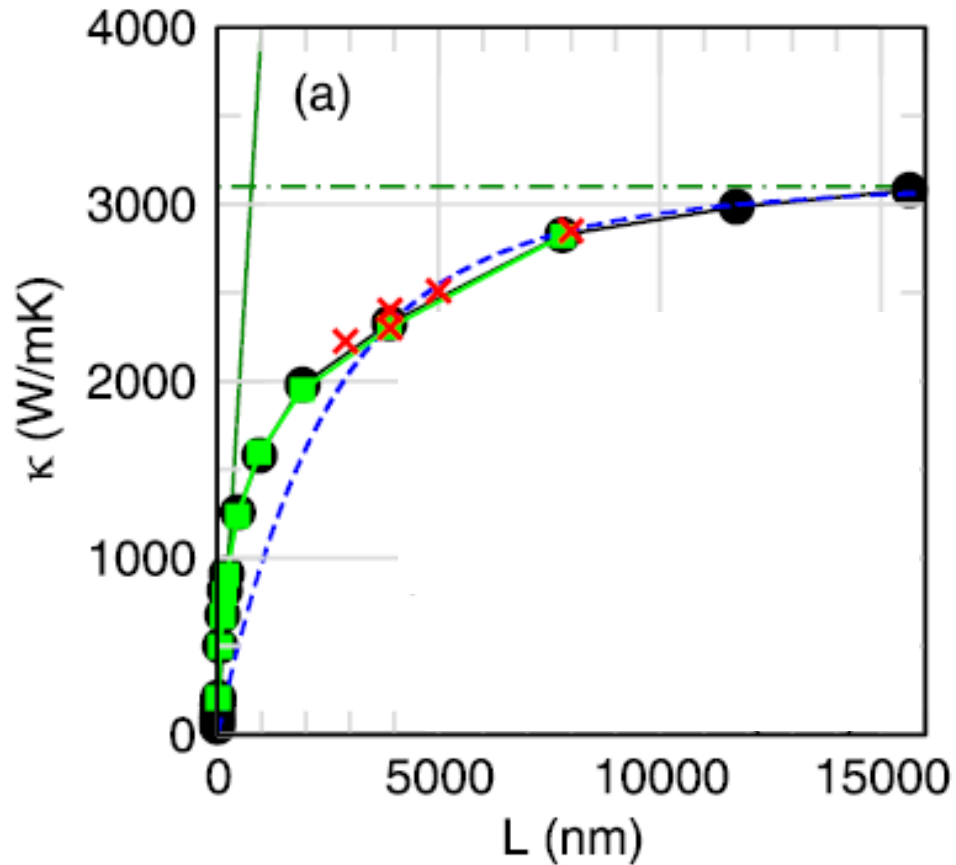


Figure 69. Thermal conductivities (κ) of graphene at room temperature as a function of the length L of graphene with widths of 1.7nm (black filled circles) and 17nm (green filled squares). The (green) solid line indicates the ballistic thermal transport limit and the (green) dot-dashed line is the macroscopic thermal conductivity[55]. The experimental data given are indicated by the (red) cross symbols. The length-dependent thermal conductivities obtained from a high-order heat transport equation are plotted by the (blue) dashed line [55].

Figure 69 shows another study of the length dependence of graphene on thermal conductivity. The thermal conductivities are also found to increase with the length and finally converge at 16 μm to a value of 3200 W/mK [55]. This is significantly lower than values shown in Figure 68 at lengths of only around 27 nm and is an example of some of the large discrepancies in results for thermal conductivity for graphene using MD in the literature.

The number of layers of graphene and whether or not it is suspended or supported on a substrate also has an effect on its thermal conductivity. The thermal conductivity of supported single layer graphene (SLG) is much lower than suspended SLG, and is almost independent of the length. In contrast to the decrease in the thermal conductivity from inter layer interaction in suspended few layer graphene (FLG), the thermal conductivity of supported FLG is found to increase with the layer thickness [56].

It was shown there is no significant change in thermal conductivity of curling and twisted GNRs due to the superior flexibility of graphene [57]. However if there is a sharp bend in the sheet as shown in Figure 70 a reduction in the thermal conductivity occurs [58].

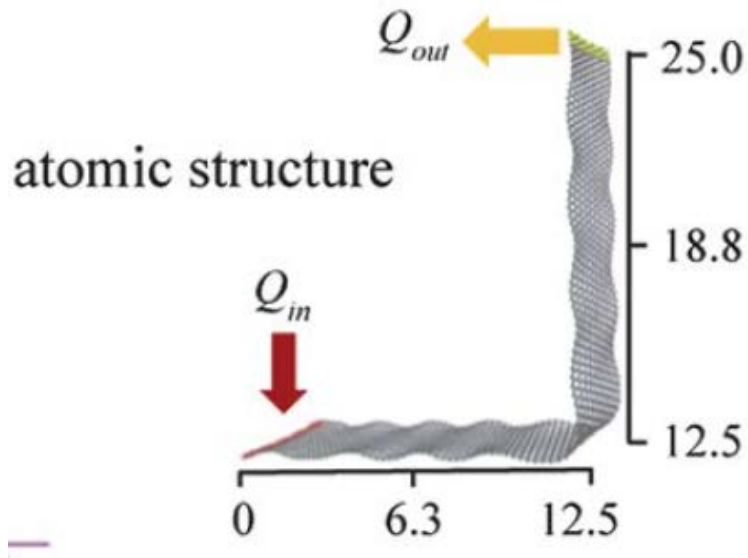


Figure 70. A sharp right-angle bend in a GNR has been shown to effect its thermal conductivity [58].

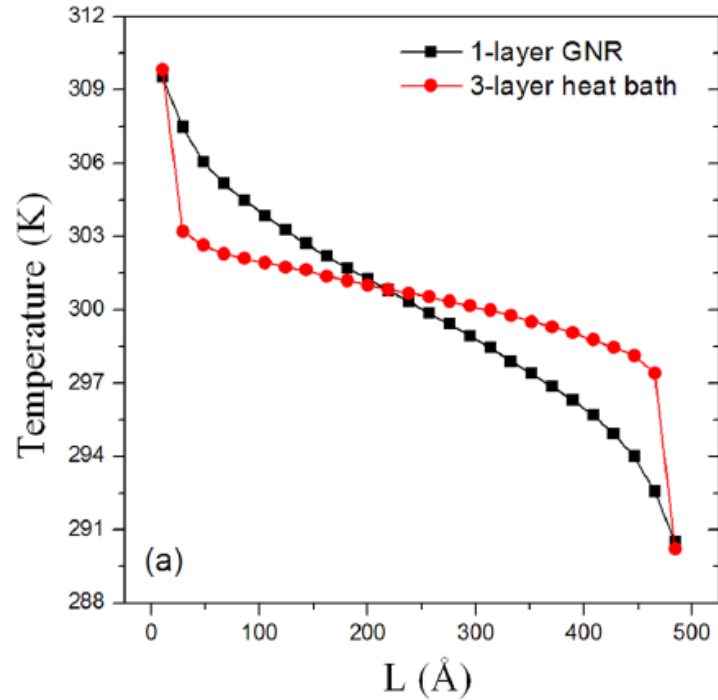


Figure 71. Temperature profiles of ideal suspended (black square) and real suspended (red circle, 3 layer heat bath refers to one graphene sheet and one substrate above and one below) single-layer GNRs [59].

As shown in Figure 71 when there is a graphene-substrate interaction at the ends of the sheet in the MD simulation, used to simulate a sheet suspended at its ends, there is a temperature jump at the ends of the sheet, which leads to a reduction in heat flux and thermal conductivity [59]. Therefore heat flux along real suspended SLG is only 40% of ideal suspended SLG where there is no substrate interaction.

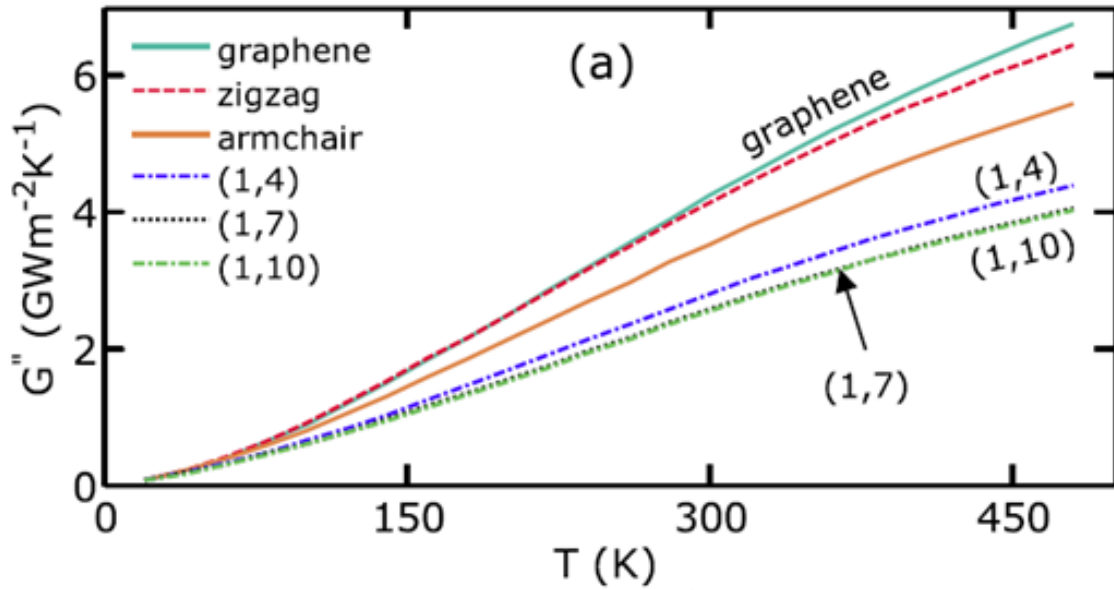


Figure 72. Thermal conductivity, G'' , vs. temperature for pristine GNR with different chiralities defined by the lattice vectors (1,4), (1,7) and (1,10), (the solid green line is for graphene with periodic boundary conditions and is not considered a GNR) [60].

GNRs with different chiralities can also effect thermal conductivity. Figure 72 shows the thermal conductivity vs. temperature of GNRs with different chiralities (the solid green line is for graphene with periodic boundary conditions and is not considered a GNR). Reduction of phonon transmission and therefore thermal conductivity is not due to the edge roughness scattering, but due to the reduction in number of modes, because phonon transmission showed linear dependence on sample width [60]. However, the thermal conductivity does not depend on chirality for sheets with periodic boundary conditions.

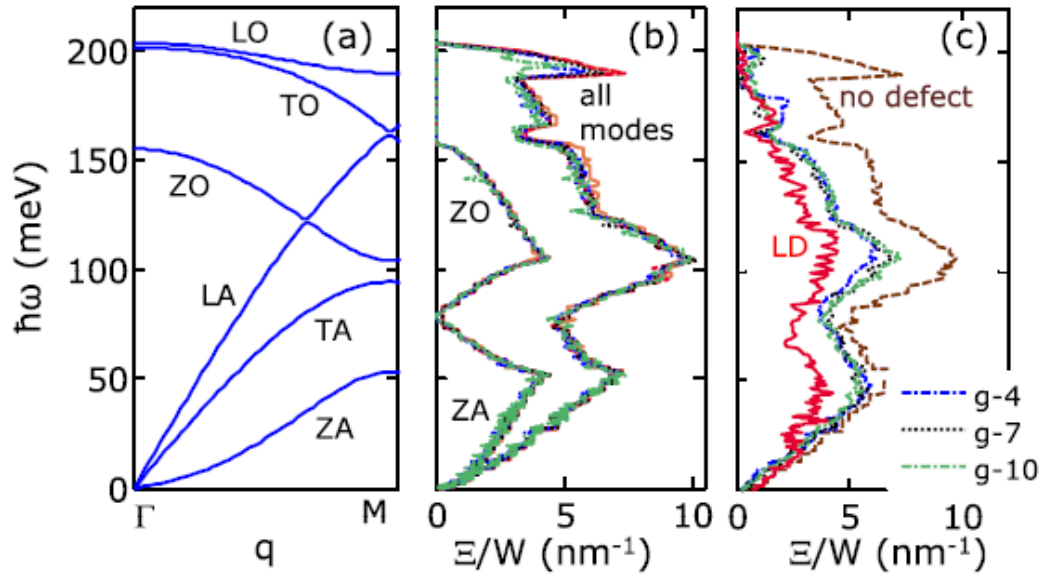


Figure 73. Phonon transmission of graphene supported on a substrate with periodic boundary conditions. (a) Computed dispersion relation for phonon energy $\hbar\omega$ vs. wave vector q . L, T, and Z correspond to longitudinal, transverse, and out-of-plane phonon displacements. A and O labels are for acoustic and optical phonons, respectively. (b) Transmission function (i.e., number of modes per width) across pristine graphene with different chiralities. Individual chiralities are not labeled because all display the same transmission spectrum. The subset of out-of-plane ZA and ZO modes are shown separately. (c) Transmission across different GBs (g-4, g-7, g-10), revealing that transmission depends on the GB structure. LD has the worst transmission [60].

Figure 73 shows results of the phonon transmission function (number of modes per width) for graphene supported on substrates that contain GBs and LDs. Higher phonon transmission correlates to higher thermal conductivity. Graphene with different GB misorientation angles have almost identical phonon transmission but the LDs exhibits the lowest. The main contribution to the thermal conductivity comes from the TA and LA modes because the ZA modes are suppressed by substrate scattering. This is in contrast to suspended graphene where the ZA modes were shown to dominate the thermal transport [61].

To understand the dependence of thermal conductivity in suspended and supported graphene a spectral energy density (SED) analysis [56, 62] for phonons in graphene can be conducted. It is a useful tool to extract phonon information from MD simulations, which can capture the full anharmonicity of the atomic interactions. A previous theoretical study has suggested that thermal conductivity of graphene is most influenced by the contributions from the flexural ZA, or out of plane, phonons [61]. A SED analysis of a suspended and supported graphene sheet is shown in Figure 74 for the ZA phonons. For suspended SLG, Figure 74(a) shows only one distinct and narrow peak shows up. The inset zooms in to show the low frequency ZA peaks. For the supported graphene with different layer numbers, the ZA phonon shifts to the right and the peaks are broadened. Figure 74(b) shows more than two orders of magnitude reduction in SED intensity for the supported sheets. This reduction in SED intensity for supported graphene is in correlation with the reduction in thermal conductivity for graphene supported by substrates.

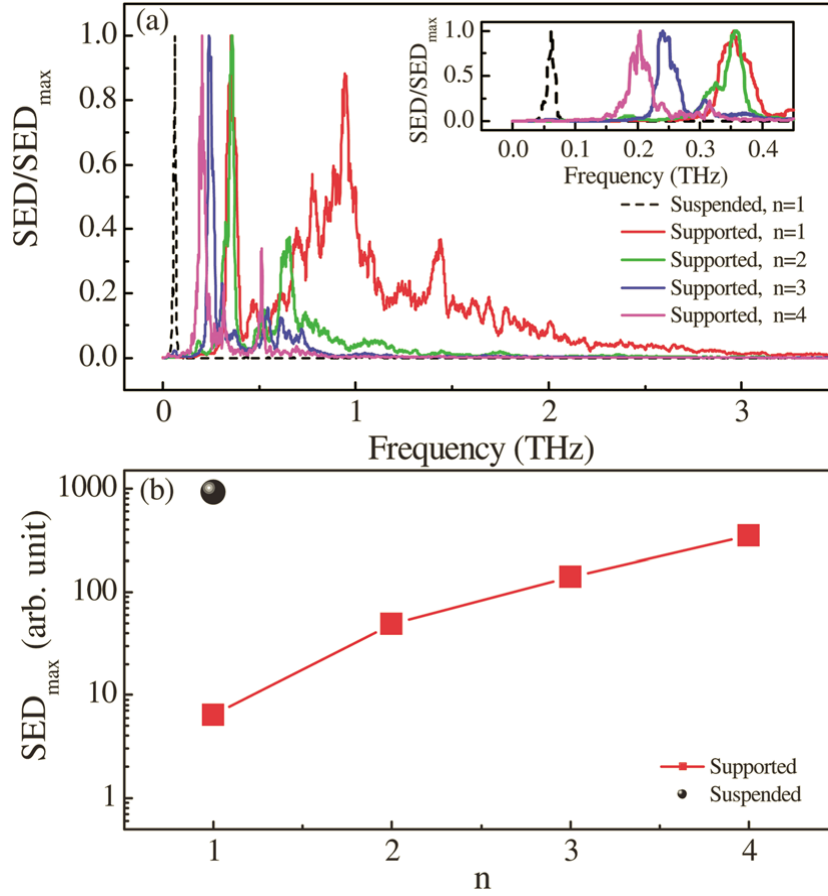


Figure 74. SED analysis for ZA phonons for suspended and supported graphene. (a) Normalized SED for suspended SLG (dashed line) and supported graphene with different number of layers (solid lines). Inset is for the low frequency ZA peaks. (b) SED intensity for the low frequency ZA peaks for suspended SLG (circle) and supported graphene with different layers (square) [56].

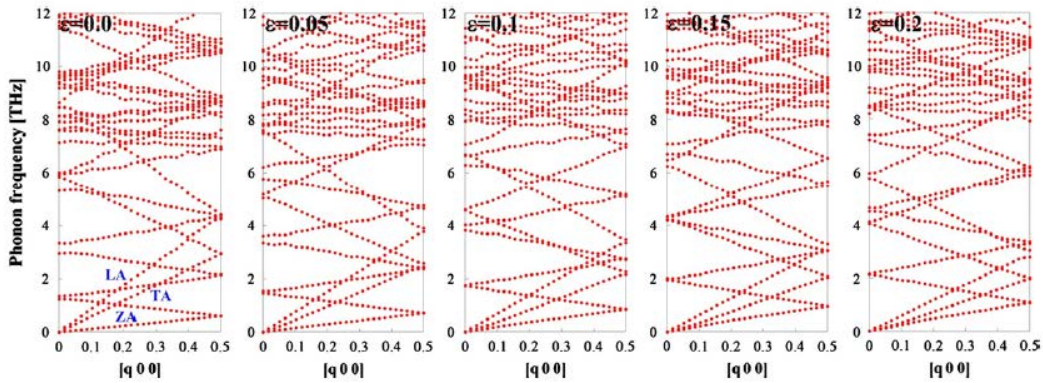


Figure 75. Phonon dispersion relations of a 21.78° GB misorientation angle in graphene for different applied shear strains [63].

The phonon dispersion relations of a 21.78° GB for different shear strains from 0.0 to 0.2 is shown in Figure 75. As the applied shear strain is increased, the velocities of the LA and TA branches are decreased. The phonon velocities of pristine graphene from MD simulations were $v_{LA} = 23.1$ and $v_{TA} = 15.4$ km/s for LA and TA modes, respectively. These values are in close agreements to the experimental values of $v_{LA} = 24.0$ and $v_{TA} = 14.0$ km/s. The phonon velocities of the 21.78° GB are 19.5 and 13.3 km/s for the LA and TA modes under zero strain, which are smaller than those of the pristine graphene due to the existence of the GBs. It is also known the graphene with GBs reduce its thermal conductivity. Therefore a reduction in the phonon velocity as a result of the shear strain correlates to a reduction in thermal conductivity. The LA and TA modes equally contribute to the decrease of the thermal conductivity, because the phonon velocities of the LA and TA modes are reduced by 33.5% and 31.8% at $e = 0.2$, respectively.

3.2 MD simulation method

This section provides details of the MD simulation method that was used to analyze graphene for this dissertation. Non-equilibrium MD (NEMD) simulations using LAMMPS were used for studying the heat transport behavior of graphene sheets. In this method two regions at opposite ends of a sheet are held at different temperatures. By holding the two regions at different temperatures the energy added to the hot region should equal the energy subtracted from the cold region and be proportional to the heat flux moving between the regions [64]. An atomic model for MD simulations on the thermal conductivity of graphene is shown in Figure 76.

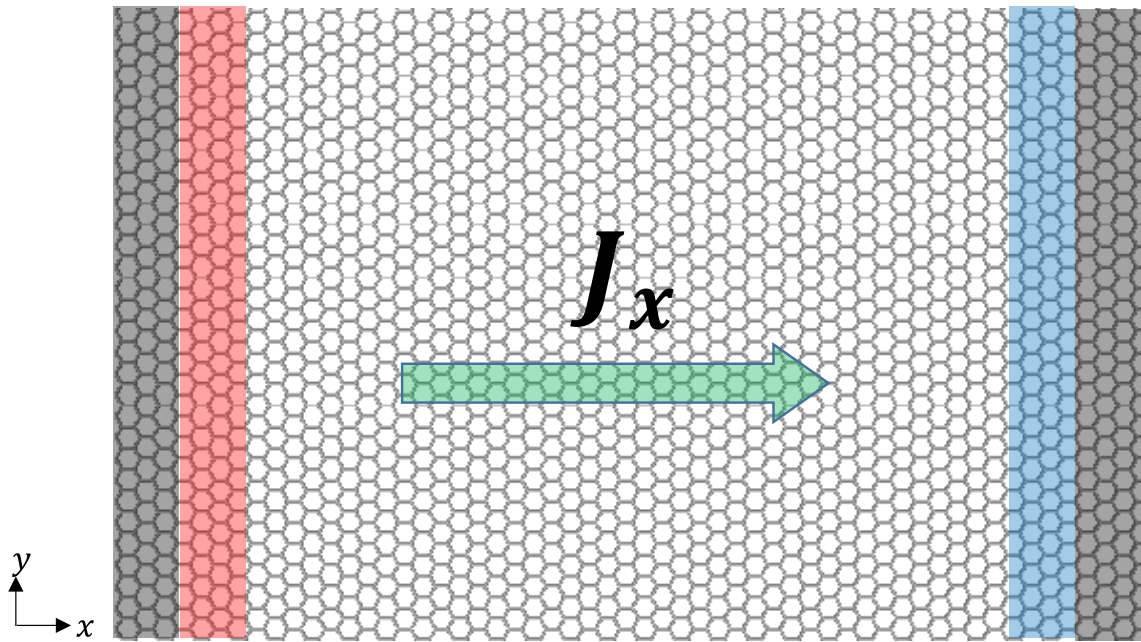


Figure 76. Atomic model for the calculation of the thermal conductivity in graphene. The black atoms at the ends are fixed in their positions. The red region is determined to have a hotter temperature than the blue region. The green arrow indicates the direction of heat flux, J_x , through the sheet.

The atoms in black are held fixed in their positions. To update the positions and velocities of these atoms each time step in LAMMPS an NVT ensemble was used in the time integration. An NVE ensemble was used for the rest of the atoms. NVT or NVE refers to a constant number of particles, velocity, temperature, or energy. The original Brenner and Tersoff inter-atomic potentials were shown to have poor agreement with experimental data on the dispersion curve of in-plane graphite and a newly optimized Tersoff and Brenner potential [65] was developed and was used in these calculations.

NEMD can be performed using the fixed flux or fixed temperature methods. For the fixed flux method a constant heat flux is assigned to the red region and extracted from the blue region and the resulting temperature gradient, $\frac{dT}{dx}$, is measured after reaching steady state. For the fixed temperature method the temperatures of two regions are assigned and held fixed with the red region being hotter than the blue region and then the heat flow is measured after reaching steady state. The fixed temperature method was used for this analysis. The thermal conductivity is then calculated using the one dimensional form of the Fourier law

$$k = - \frac{J_x}{A \frac{dT}{dx}} \quad (17)$$

where J_x is the heat flux in the x direction, and $\frac{dT}{dx}$ is the temperature gradient in the sheet. The cross sectional area that the heat flux flows through is $A = w \cdot h$ as shown in Figure 77, where w is the width of the sheet and h is the thickness and was taken as 3.4\AA , which is equal to the interlayer spacing in graphite.

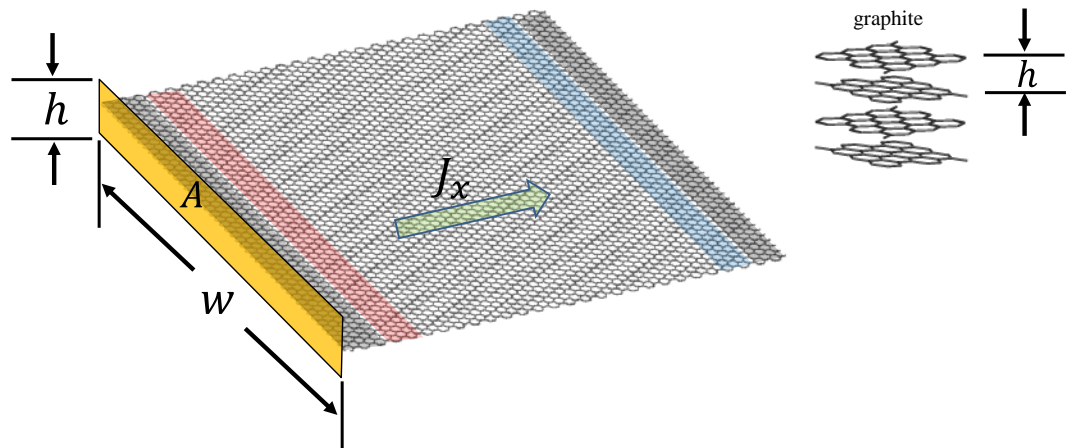


Figure 77. Image showing the cross sectional area that the heat flux flows through. h is the interlayer spacing in graphite.

Figure 78 shows the evolution of the cumulative energy over time, which is given by the following equation [55]

$$E(t) = (E_h(t) - E_c(t))/2 \quad (18)$$

where $E_h(t)$ is the cumulative energy supplied to the hot region and $E_c(t)$ is the cumulative energy extracted from the cold region. $E(t)$ is the average cumulative energy per width of the sheet.

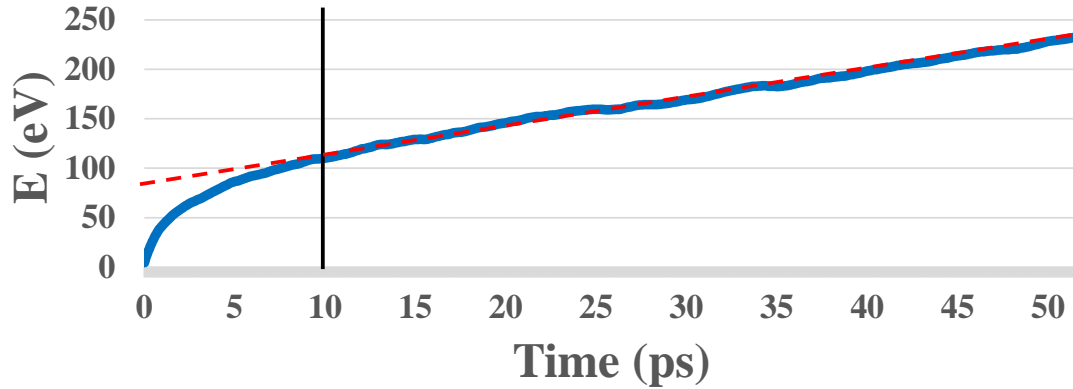


Figure 78. Cumulative energy that flows along the heat transport direction in graphene as a function of time. After reaching the steady state, the constant energy per time flows as shown by the linearly fit (red dashed) line and begins here at around 10ps.

After reaching steady state, which is around 10 ps in Figure 78, the cumulative energy linearly increases and the heat flux can be calculated from

$$J_x = \left(\frac{dE}{dt} \right) / (w \cdot h) \quad (19)$$

where w is the width of the sheet and h is the thickness. The calculated thermal conductivities of graphene using the fixed temperature or fixed flux method were 2360 and 2350 W/mK [54], which are very close. It is important to note that the gradient used in the

calculations is obtained from points in the interior of the sheet as opposed to using the fixed temperatures at the two ends and the total length of the sheet to calculate the gradient, since the resistance of the sheet will cause the interior gradient to be different. Figure 79 shows a typical temperature profile of a graphene sheet from a MD analysis where it is apparent that the interior gradient is different from the gradient that would be obtained using the temperature at the very ends of the sheet.

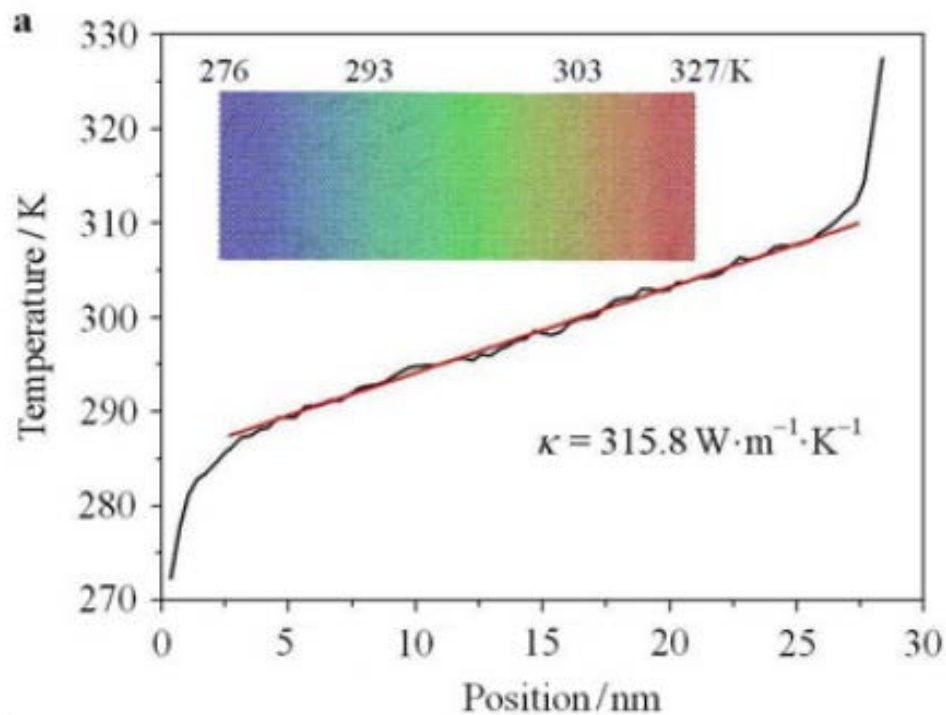


Figure 79. Typical steady state temperature profile for a graphene sheet. The inset shown is the temperature contour map [66].

To calculate the temperature gradient, $\frac{dT}{dx}$, the temperature profile is needed. This is determined by dividing the sheet of graphene into equally spaced slabs along its length. After achieving steady state, $J_x = \text{constant}$, the temperature profile of the system can be determined by computing the temperature of each slab using the following equation[67]

$$\frac{3N_{slab}k_bT_{slab}}{2} = \frac{1}{2} \left\langle \sum_i^{N_{slab}} m_i v_i^2 \right\rangle \quad (20)$$

where N_{slab} is the number of atoms in the slab, T_{slab} is the temperature of the slab, and k_b is the Boltzmann's constant. The brackets indicate the average over time.

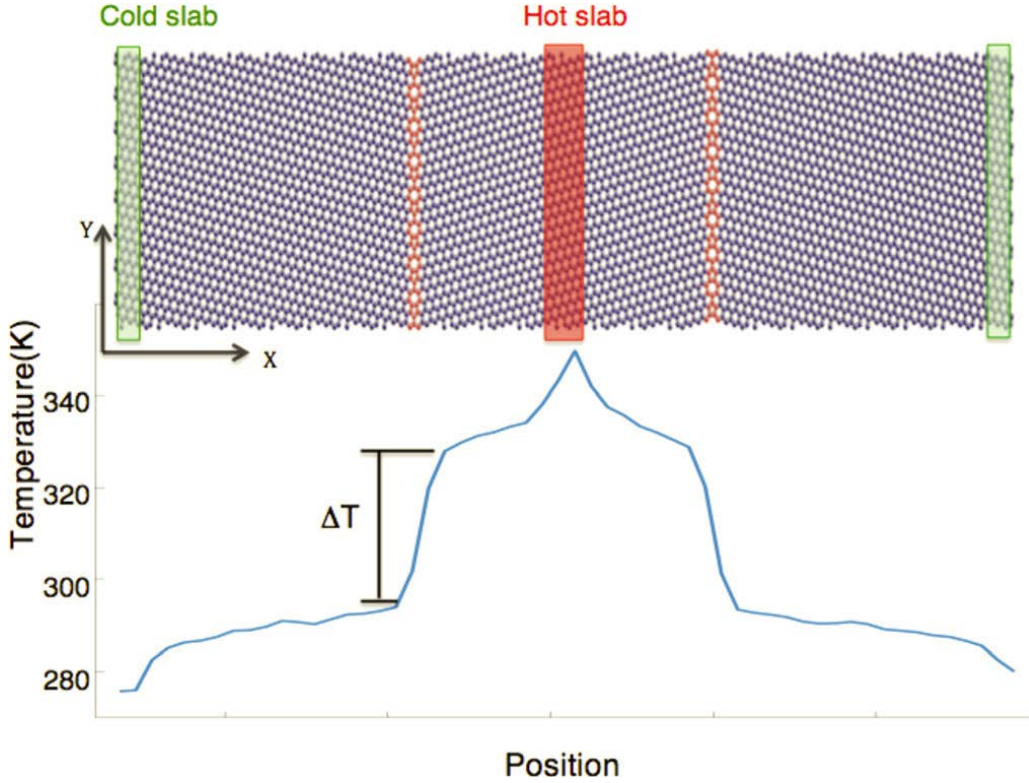


Figure 80. Graphene sheet with two GBs with GB misorientation angle of 21.7°. The cold slabs on either end of the sheet and the hot slab in the middle are shown using green and red colors, respectively. The bottom figure shows a temperature profile with a distinct temperature jump at the two grain boundaries [68].

Figure 80 shows another method of measuring the thermal transport in graphene which is the boundary conductance (Kapitza conductance) G_k of the grain boundary and is given by the following equation

$$G_k = -J/\Delta T \quad (21)$$

This is another method of analyzing the thermal transport of graphene sheets with GB.

3.3 Thermal effect from GB misorientation angle and loading angle

Just as the stress-strain and fracture behavior of graphene with different GB misorientation angles and loading angles were studied, the effect of varying these angles on the thermal conductivity was investigated.

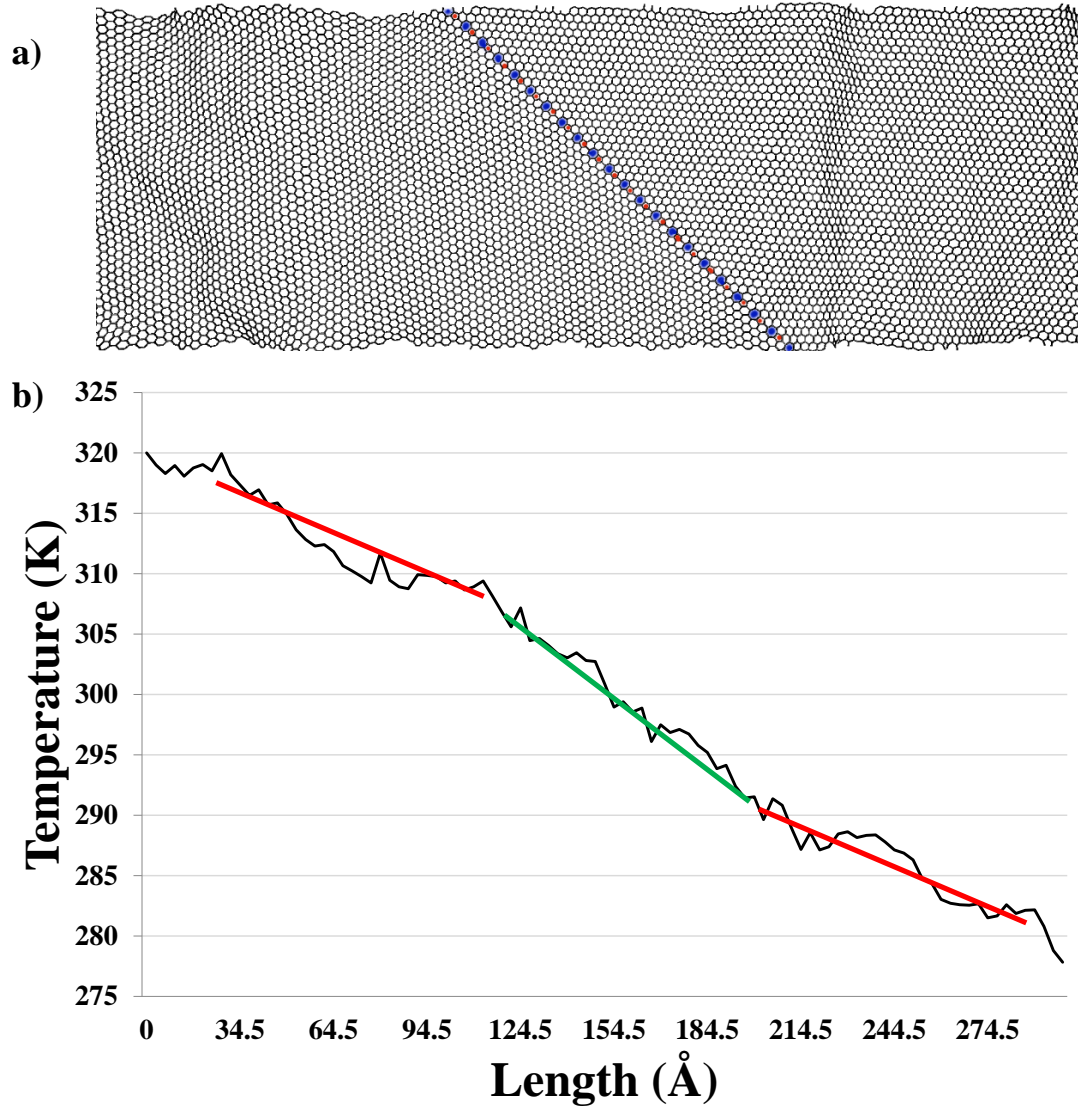


Figure 81. Plot of two temperature gradients for a sheet of graphene with a GB a) Atomic structure of graphene with a GB at a 45° loading angle b) Temperature profile for the graphene sheet in a) shown by the black line. The red line is temperature gradient fit to the data from the graphene region to the right and left of the GB. The green line is the temperature gradient fit to the region containing the GB.

Figure 81 shows the temperature profile for a sheet of graphene with a GB at a 45° loading angle. The temperature profile shown is for the entire width of the sheet and shows two different gradients indicated by the red and green lines. However, only one gradient can be used for the calculation of thermal conductivity. Therefore a linear fit of the temperature gradient of the entire sheet (excluding the very ends) was used instead.

Figure 82 shows another example of a temperature profile from a sheet of graphene with a GB. The points from this profile were then input to Matlab and a linear fit algorithm was used to get a best fit for all the points to get the temperature gradient as shown by the red line.

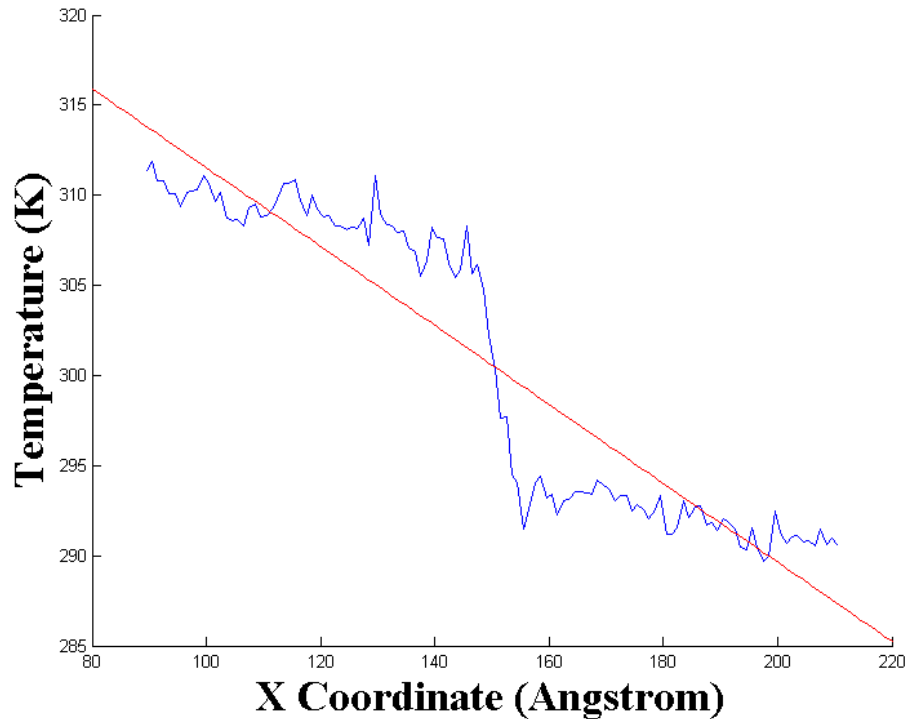


Figure 82. Plot of one temperature gradient for a sheet of graphene containing a GB. All points from the temperature profile were used to get a best fit to be used as the temperature gradient (red line) using a linear fit algorithm in Matlab.

This is in contrast to a previous study [51] that calculated the thermal conductivity of graphene that contained a GB using the gradient of only a pristine portion of the sheet as shown in Figure 83.

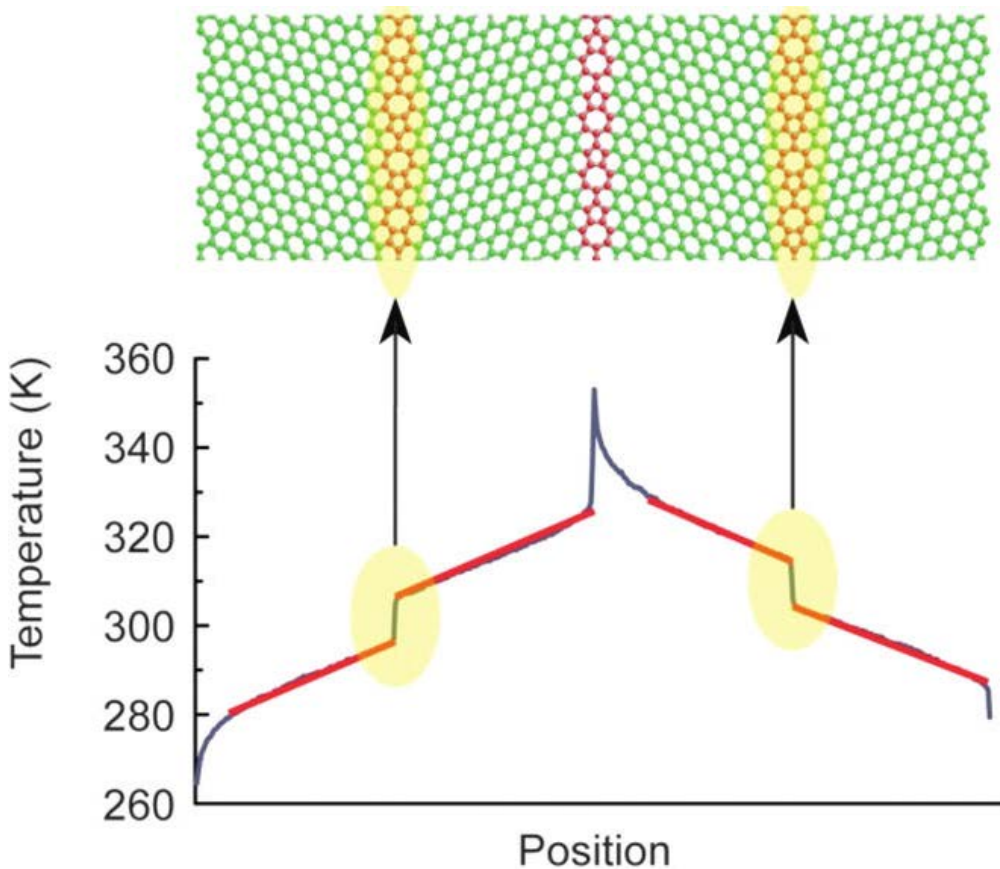


Figure 83. Temperature profile of a sheet of graphene and temperature gradients obtained from points in the pristine regions only [51].

Since the difference in temperature near one end of the sheet to the temperature near the other end of the sheet would be of interest in devices that use graphene like electronics the former method of calculating the gradient was used.

Figure 84 shows MD results for thermal conductivity vs. loading angle of the GB within graphene.

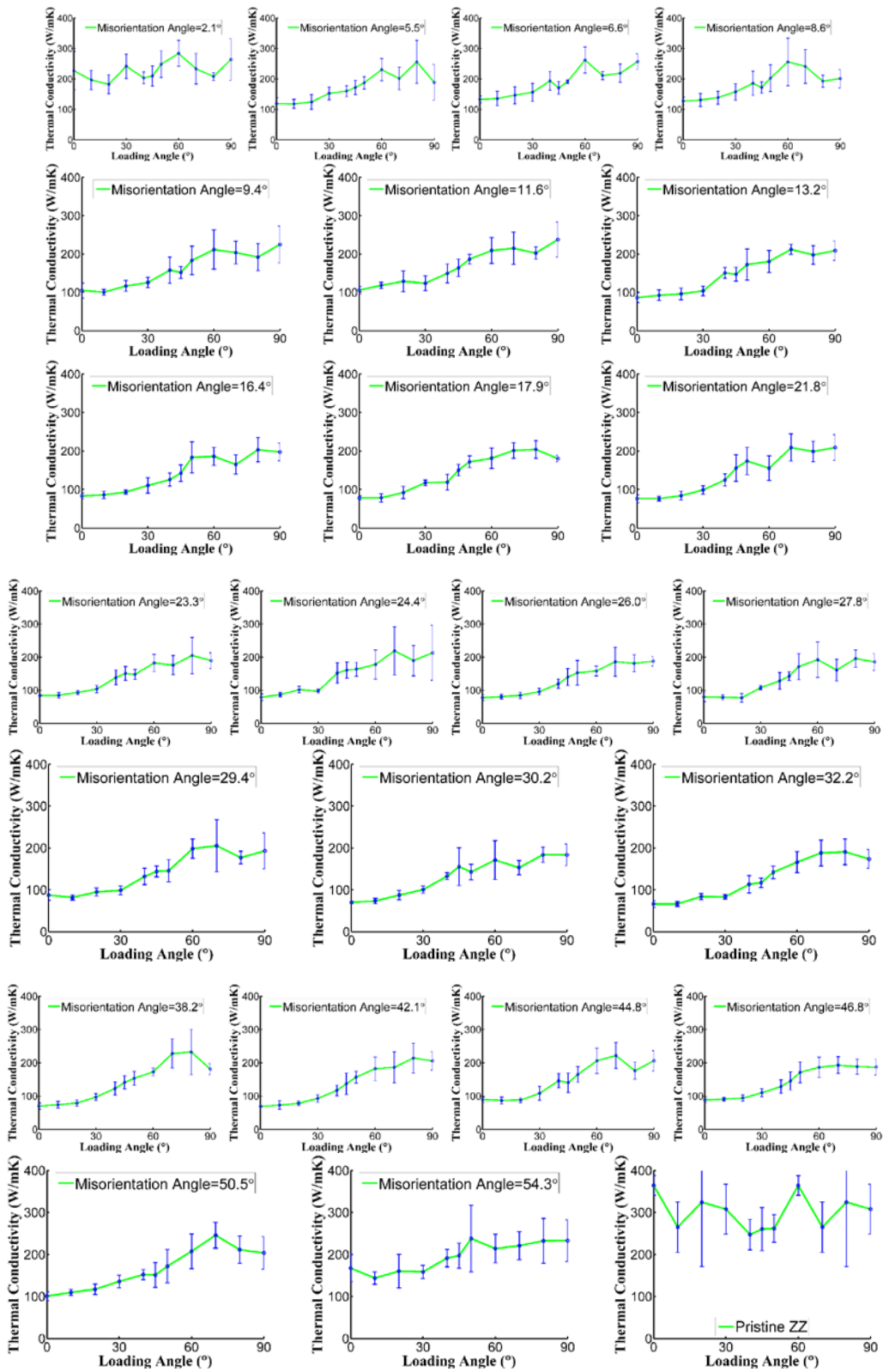


Figure 84. Thermal Conductivity vs. Loading Angle (error bars indicate standard deviation). Thermal conductivity increases with the loading angle as an overall trend.

From these figures it is shown that the overall trend is for the thermal conductivity to increase with the loading angle. One of the reasons for this is that when the loading angle is at 0° the graphene sheet is in a series resistance with the sheet being divided into a left and right hand region. This can also be considered to be two short and wide graphene sheets connected along their width as shown in Figure 85. When the loading angle is at 90° the sheet is in a parallel resistance where the sheet is divided into a top and bottom region. This can also be considered to be two long and narrow sheets connected along their length as shown in Figure 86. It was shown how the thermal conductivity of graphene was dependent on both the length and width of the sheet from previous studies [53]. Since the thermal conductivities of graphene with higher loading angles are higher it is clear that the length of the sheet has a greater effect on the thermal conductivity as opposed to its width.

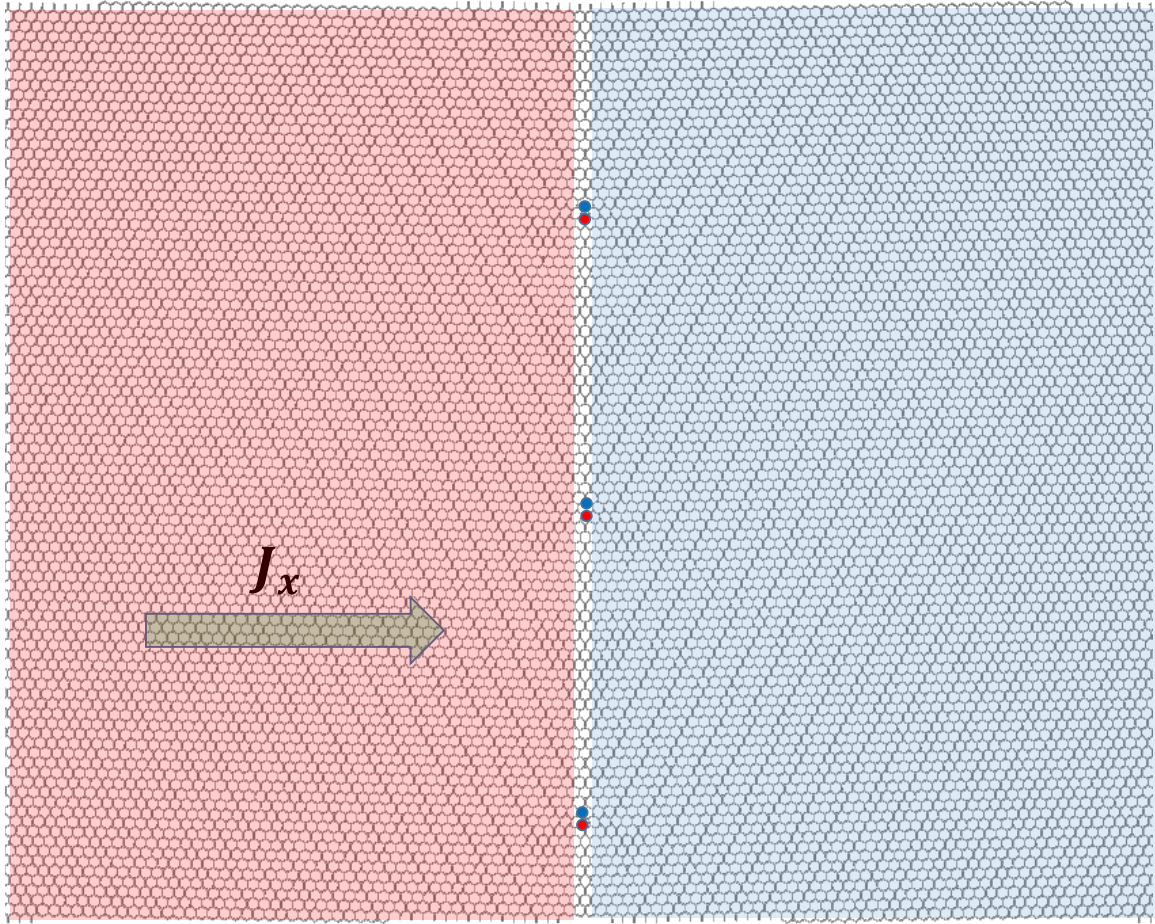


Figure 85. Graphene in series resistance from a GB.

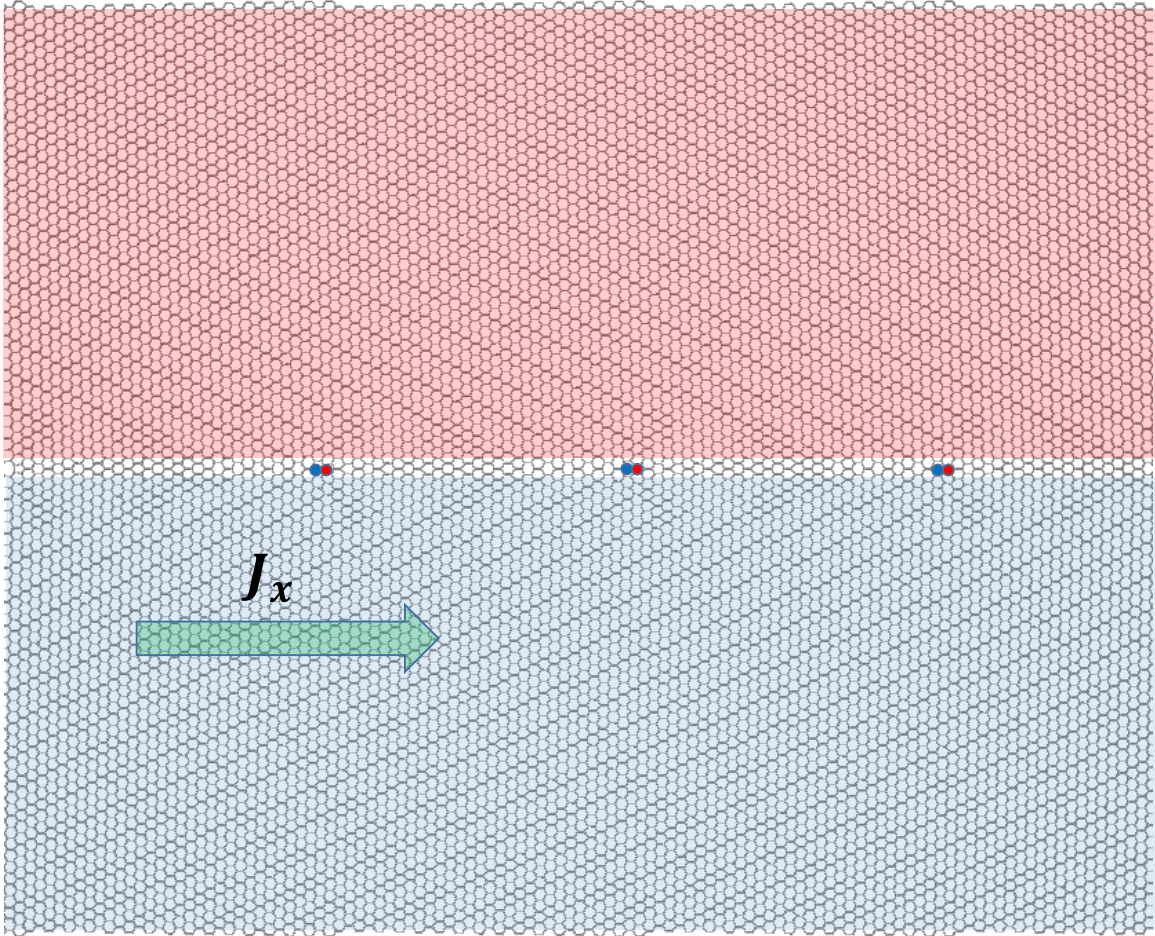


Figure 86. Graphene in parallel resistance from a GB.

From the results in Figure 84 it can be seen that the thermal conductivity saturates at around the 50° loading angle. Figure 87 shows that at this loading angle the sheet transitions from a series resistance to a parallel resistance.

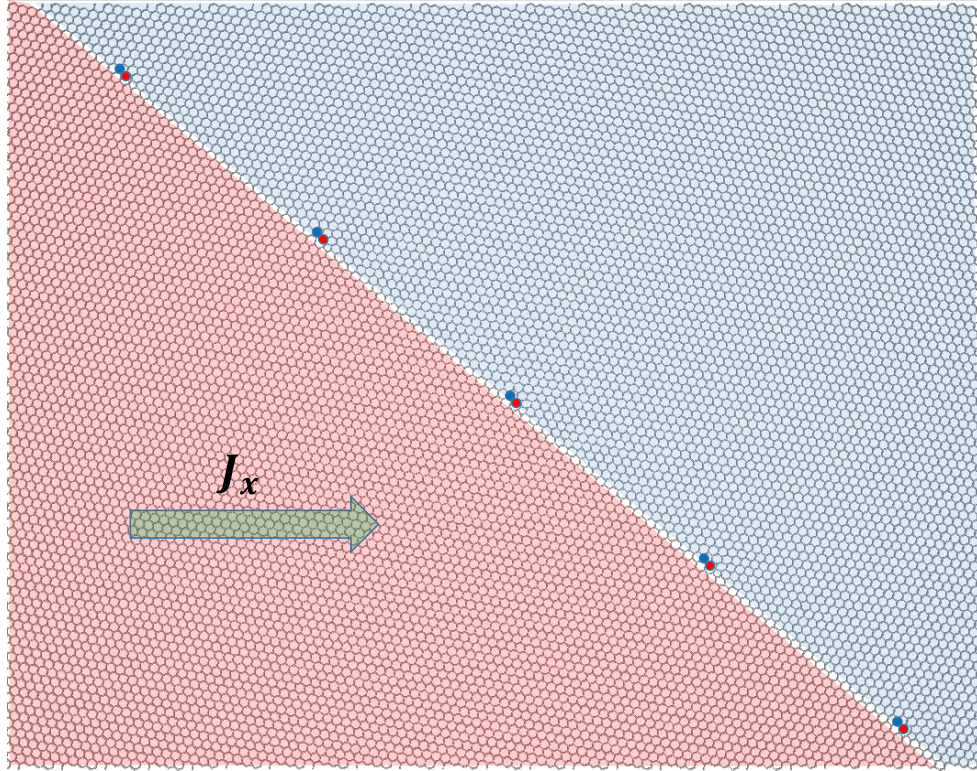


Figure 87. Graphene with a 50° loading angle. At this angle the graphene sheet is in between a series resistance and a parallel resistance and is where the thermal conductivity of the sheet starts to saturate as the loading angle is increased.

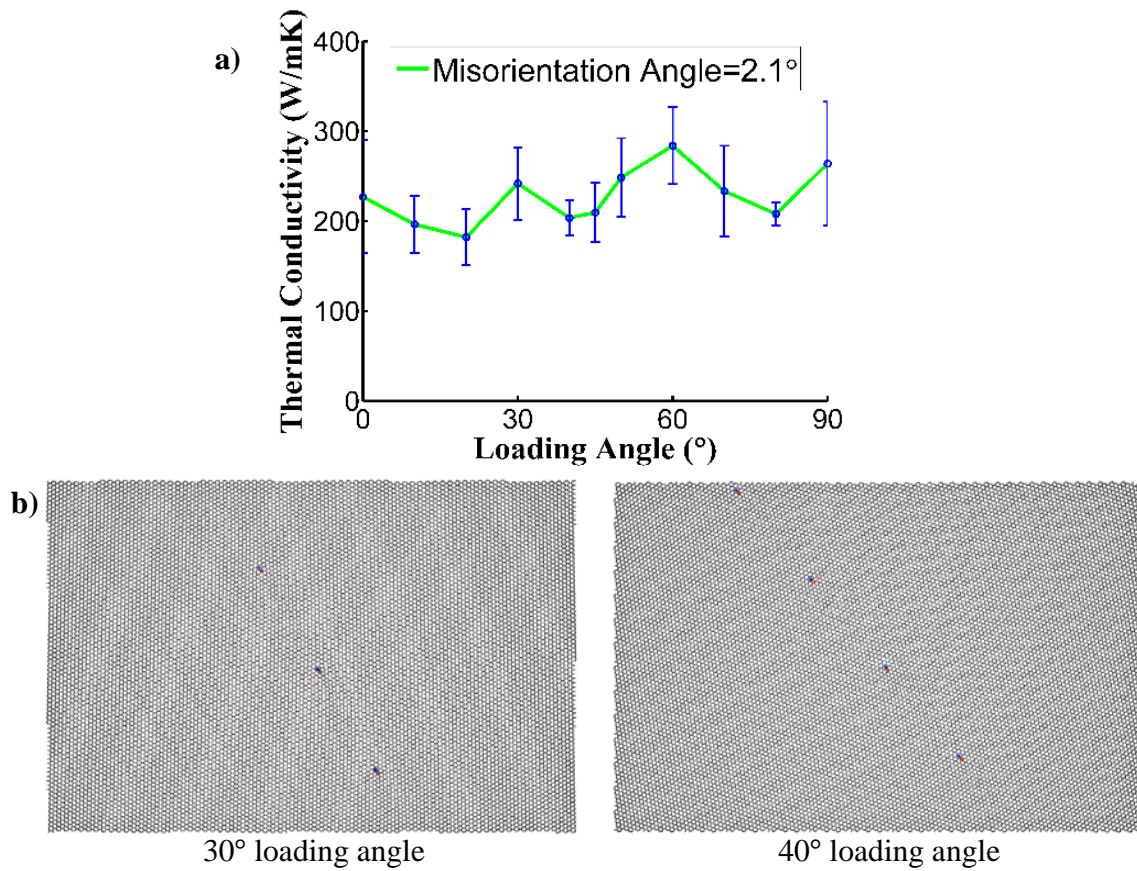


Figure 88. Fluctuation in the thermal conductivity vs. loading angle curves can be influenced by the number of defects in the sheets a) curve shows the thermal conductivity decreases as the loading angle is increased from 30° to 40° b) sheets show that for the 2.1° GB misorientation angle the number of defects increases from 3 to 4 as the loading angle is increased from 30° to 40°.

The trend for the curves in Figure 84 shows an increase in thermal conductivity with loading angle. However there is not a monotonic increase. One of the reasons for the fluctuation is that as the loading angle increases a longer portion of GB is included in the sheet and more defects are present. Figure 88 shows the curve for the thermal conductivity vs. loading angle for the 2.1° GB misorientation angle. The curve shows that as the loading angle increases from 30° to 40° the thermal conductivity is reduced. The reason that the thermal conductivity is reduced in this situation is that one more defect is included in the sheet. For the 30° degree loading angle there are only three defects along the GB. At the

40° degree loading angle the same three defects are present but there is also another one included at the top of the sheet for a total of four defects.

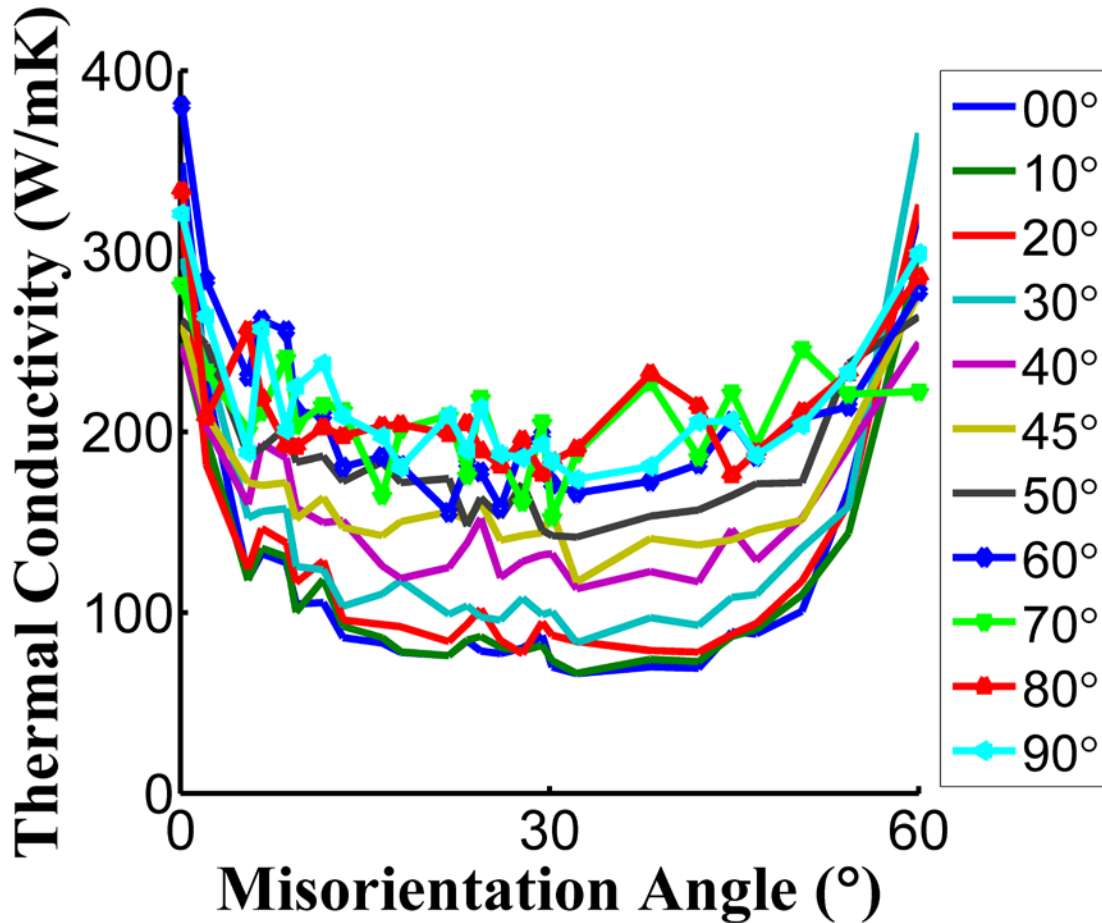


Figure 89. Thermal conductivity vs. misorientation angle for all loading angles. The graph shows the range of GB misorientation angles where the defect density is highest (~20°-30°) the thermal conductivity is lowest. This indicates that a GB with high defect density will reduce the thermal conductivity.

Figure 89 shows the thermal conductivity of graphene vs. GB misorientation angle. The dependence of defect density of GBs on the misorientation angle can be seen from the GBs structures shown in Figure 40. For the 0-60° range of misorientation angles analyzed in Figure 40 it is clear that the defect density is highest for the inner portion of this range.

Figure 89 shows the thermal conductivity is lowest when defect density is highest since the thermal conductivity is lowest for the same range of misorientation angles that have the highest defect density. A previous study [69] shown in Figure 91 also noticed this trend for the AC GBs and determined that a higher defect density results in more phonon-GB scattering which reduces the thermal conductivity. Figure 89 shows that while the GB misorientation angle increases for the ZZ GBs the thermal conductivity increases. Since the ZZ GBs defect density decreases with the GB misorientation angle this confirms the hypothesis from [69] of the effect of the defect density on thermal conductivity.

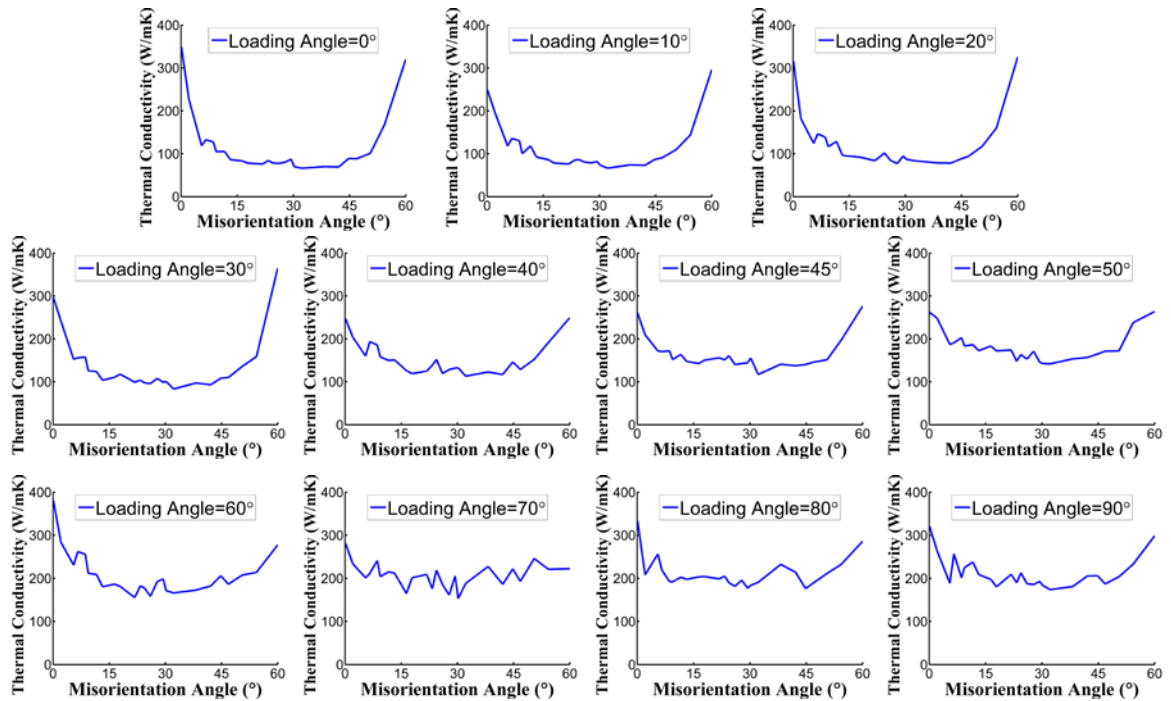


Figure 90. Thermal conductivity vs. misorientation angle for individual loading angles. For the higher loading angles the where the loading angle is parallel to the thermal transport direction the thermal conductivity does not drop as much compared to the lower loading angles. This indicates there is much less phonon-GB scattering.

Figure 90 shows the thermal conductivity vs. misorientation angle for each individual loading angle. It can be seen here that the thermal conductivity does not drop as much for

the higher loading angles. For the higher loading angles the thermal transport does not have to directly go through the GB and there is not as much phonon-GB scattering.

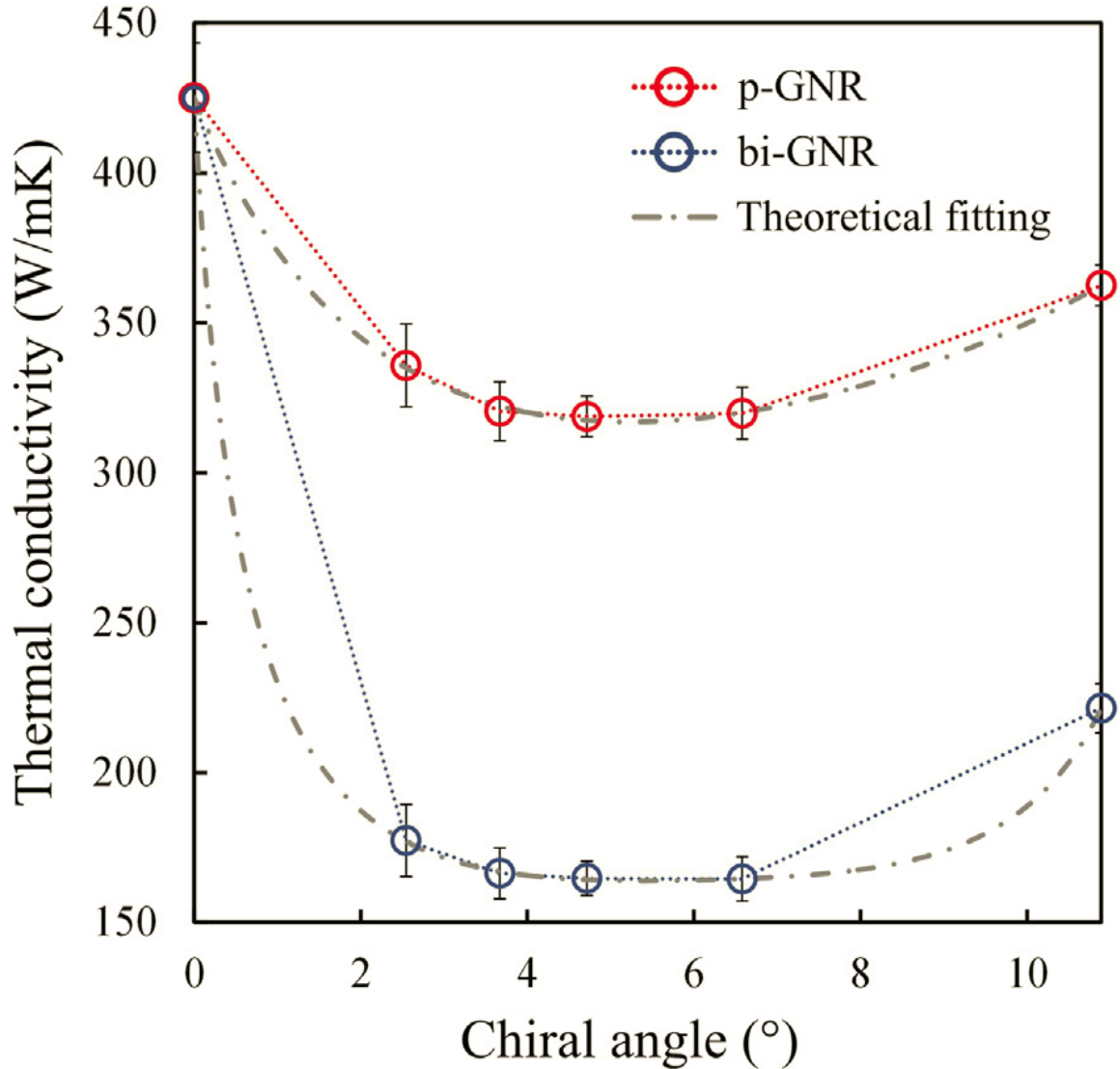


Figure 91. The thermal conductivity for the AC GBs (Chiral angle shown is half the value of the GB misorientation angle). The thermal conductivity is reduced as the GB misorientation angle increases except for the last point. The red and blue symbols represent the pristine GNRs and GNRs with GBs, respectively. Data points with the same chiral angles means that they have the same edge roughness. The difference of thermal conductivity is derived from the GB's effects for these points [69].

Figure 92 shows the results of the thermal conductivity vs. GB misorientation angle (labeled as chiral angle, which is half the value of the GB misorientation angle). The results

show the same trend in thermal conductivity for the AC GBs as shown in Figure 89 in that the thermal conductivity decreases with the GB misorientation angle and hence defect density. The last point however for a chiral angle of 10.89° the thermal conductivity increases while the defect density increases. One reason for this is shown in Figure 92. For all of the sheets with GBs the sheets buckles out of plane as a result of the stress induced from the GBs except for the one with a chiral angle of 10.89° . Therefore, the buckling of the graphene sheet along with the defect density has an influence on thermal conductivity.

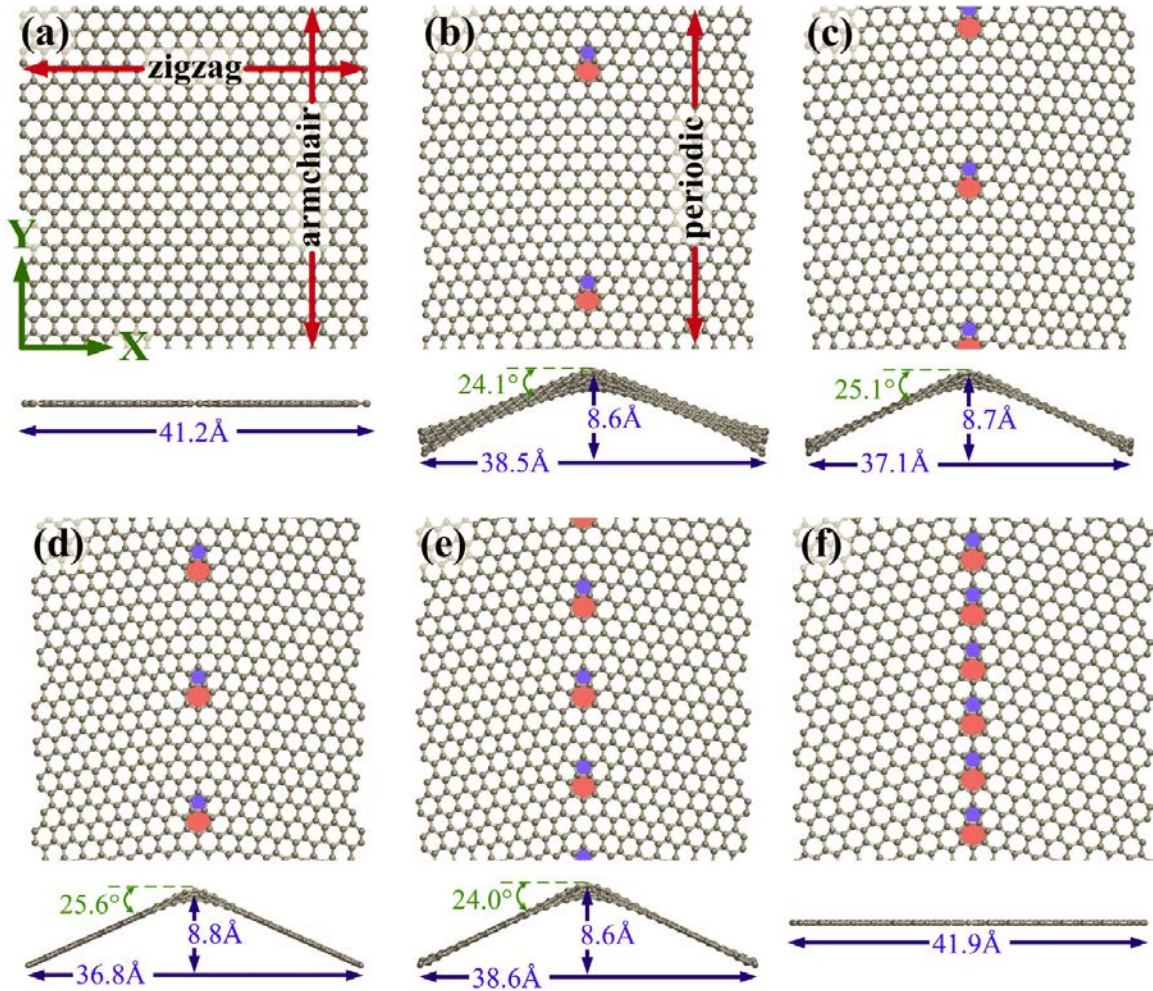


Figure 92. The top and side views of the GNRs with different GB misorientation angles θ . (a) and (f) show no out of plane buckling, (b)-(e) show the sheet buckling out of plane in the Z direction [69].

3.4 Conclusion

The results obtained from the MD analysis for how the thermal conductivity is dependent on the GBs loading angle can be beneficial in designing devices used in electronics. The results showed that for higher loading angles the thermal conductivity was higher. A critical loading angle was identified at 50° where the resistance of the graphene sheet transitions from a series resistance to a parallel resistance and the thermal conductivity

saturates to its highest value. It was also shown that GBs with high defect density will reduce the thermal conductivity more than GBs with low defect density, but that this trend is decreased as the loading angle increases. These results can be useful when designing devices that needed to use a material like graphene that need a high thermal conductivity to effectively dissipate heat that is generated during its operation.

Chapter 4: Summary and future work

4.1 Summary of major findings

It was found that the GB misorientation angle and loading angle have a significant effect on graphene's mechanical properties. Previous studies have considered various GB misorientation angles. By also analyzing various loading angles it was determined there were two critical loading angles that have a significant effect on the ultimate failure strength of graphene. These loading angles are orientated so that one of the critical bonds in the top of the disclination dipoles becomes parallel to the applied tensile load. When this occurs the ultimate failure strength is greatly reduced, since the full tensile load is applied directly along the bond. This occurs at the 25° loading angle where all of the AC GBs have their lowest failure strength and the 0° loading angle for the ZZ GBs.

A detailed analysis of how fracture of graphene with GBs occurs was also conducted. It was shown that bond breaking normally starts at the top of the disclination dipoles. These bonds are subjected to the highest initial tensile stress. The arrangement of these defects along the GB has a significant effect on how much initial stress is in these critical bonds. The breaking of these critical bonds are the points at which the ultimate failure strength of the graphene sheets occur. It was also found that as the loading angle of the GB is rotated the critical bond will normally switch to a bond that is near the top of a disclination dipole and most parallel to the loading direction.

A continuum model was developed to approximate this ultimate failure strength of graphene sheets containing GBs with different loading angles. It was shown that the continuum models results matched well with the results obtained from the MD simulations.

It was shown that the fracture process of polycrystalline sheets with multiple grains and GBs will start to fracture at points where GBs intersect. This is not always the case though and it was shown that the fracture can first start at points along the edge or within a single GB.

The same set of GB misorientation angles and loading angles were also used to analyze the effect they had on the thermal transport in graphene. It was shown that GBs with high defect density reduces the thermal conductivity more than GBs with low defect density. This trend is decreased however as the loading angle increases since the thermal transport does not have to directly go through the GB resulting in less phonon-GB scattering.

4.2 Scientific contributions

This results of the effect of the GB misorientation angle and loading angle on the failure strength and strain of polycrystalline graphene can be useful to improve the theory of two dimensional materials. For example it was shown that by using all stress components and a resultant stress vector along the direction of the critical bond an improvement was made on the prediction of the failure strength of graphene with GBs from previous studies.

Two critical loading angles were identified by analyzing both a range of GB misorientation angles and loading angles. These critical loading angles occur where the ultimate failure strength of the graphene sheets are greatly reduced.

It was shown from previous studies that the arrangement of defects in graphene can be manipulated by using electron beam irradiation. If a better understanding of how the arrangement of these defect takes place and easier methods of controlling their arrangement is developed the results obtained from above can be used to design patterns in graphene

that improve the mechanical properties of graphene that are superior to polycrystalline graphene with arbitrary GB misorientation angles and loading angles.

The findings from the fracture analysis led to an understanding for the discrepancy of the results from this dissertation and previous studies on the failure strength and critical strain of polycrystalline graphene.

The results for the thermal analysis confirmed the analysis from a previous study [69] of the effect of the defect density of GBs on the thermal conductivity of graphene. The study [69] stated the defect density of the GBs will reduce the thermal conductivity of graphene when the defect density is highest. It was shown in this dissertation the same is true for a different range of GB misorientation angles, therefore confirming their hypothesis.

These findings could potentially help in the implementation of graphene in many applications like flexible electronics, thin film solar cells, nanoresonators, etc.

4.3 Future work

For the analysis of the failure of triple junctions done here only the angle between the top two grains was controlled. More analysis could be done on the failure of triple junctions by also controlling the orientation of each individual grain so that each GB could have a controlled GB misorientation angle as well.

New algorithms to generate polycrystalline sheets could be developed, which could be used to control the GB misorientation angle and loading angle of all of the GBs within

polycrystalline graphene. This could be used to generate other grain patterns besides the arbitrary shaped and hexagonal grain sheets that were analyzed.

The largest graphene sheets analyzed for this dissertation were around 30 X 20nm. Larger sheets of graphene could be analyzed. These sheets would more closely model some of the experimental results that were mentioned in this paper that showed edges of around 200nm [8, 9]. Limitations due to the amount of time required to run simulations, time to move data, and space needed to store the data, etc. currently make it cost prohibitive to analyze sheets that were much larger than the ones that were analyzed here.

Thermal analysis has been done on polycrystalline sheets that are similar to the ones done for this dissertation. The same type of thermal analysis could be done on sheets with other well-defined grain patterns to see if they can produce sheets with higher thermal conductivities.

References

- [1] Novoselov KS, Geim AK, Morozov SV, Jiang D, Zhang Y, Dubonos SV, et al. Electric field effect in atomically thin carbon films. *Science*. 2004;306(5696):666-9.
- [2] Lee C, Wei XD, Kysar JW, Hone J. Measurement of the elastic properties and intrinsic strength of monolayer graphene. *Science*. 2008;321(5887):385-8.
- [3] Geim AK. Graphene: Status and Prospects. *Science*. 2009;324(5934):1530-4.
- [4] Balandin AA, Ghosh S, Bao WZ, Calizo I, Teweldebrhan D, Miao F, et al. Superior thermal conductivity of single-layer graphene. *Nano Letters*. 2008;8(3):902-7.
- [5] Haskins J, Kinaci A, Sevik C, Sevincli H, Cuniberti G, Cagin T. Control of Thermal and Electronic Transport in Defect-Engineered Graphene Nanoribbons. *Acs Nano*. 2011;5(5):3779-87.
- [6] Geim AK, Novoselov KS. The rise of graphene. *Nature Materials*. 2007;6(3):183-91.
- [7] Bae S, Kim H, Lee Y, Xu XF, Park JS, Zheng Y, et al. Roll-to-roll production of 30-inch graphene films for transparent electrodes. *Nature Nanotechnology*. 2010;5(8):574-8.
- [8] Huang PY, Ruiz-Vargas CS, van der Zande AM, Whitney WS, Levendorf MP, Kevek JW, et al. Grains and grain boundaries in single-layer graphene atomic patchwork quilts. *Nature*. 2011;469(7330):389-+.
- [9] Ruiz-Vargas CS, Zhuang HLL, Huang PY, van der Zande AM, Garg S, McEuen PL, et al. Softened Elastic Response and Unzipping in Chemical Vapor Deposition Graphene Membranes. *Nano Letters*. 2011;11(6):2259-63.
- [10] Lee GH, Cooper RC, An SJ, Lee S, van der Zande A, Petrone N, et al. High-Strength Chemical-Vapor Deposited Graphene and Grain Boundaries. *Science*. 2013;340(6136):1073-6.
- [11] Rasool HI, Ophus C, Klug WS, Zettl A, Gimzewski JK. Measurement of the intrinsic strength of crystalline and polycrystalline graphene. *Nature Communications*. 2013;4:7.
- [12] Grantab R, Shenoy VB, Ruoff RS. Anomalous Strength Characteristics of Tilt Grain Boundaries in Graphene. *Science*. 2010;330(6006):946-8.
- [13] Wang H, Wang GZ, Bao PF, Yang SL, Zhu W, Xie X, et al. Controllable Synthesis of Submillimeter Single-Crystal Monolayer Graphene Domains on Copper Foils by Suppressing Nucleation. *Journal of the American Chemical Society*. 2012;134(8):3627-30.
- [14] Yu Q, Jauregui LA, Wu W, Colby R, Tian J, Su Z, et al. Control and characterization of individual grains and grain boundaries in graphene grown by chemical vapour deposition. *Nature Materials*. 2011;10(6):443-9.
- [15] Zandiataashbar A, Lee GH, An SJ, Lee S, Mathew N, Terrones M, et al. Effect of defects on the intrinsic strength and stiffness of graphene. *Nature Communications*. 2014;5:9.
- [16] Zhang P, Ma LL, Fan FF, Zeng Z, Peng C, Loya PE, et al. Fracture toughness of graphene. *Nature Communications*. 2014;5:7.
- [17] Wei Y, Wu J, Yin H, Shi X, Yang R, Dresselhaus M. The nature of strength enhancement and weakening by pentagon–heptagon defects in graphene *NATURE MATERIALS* 2012.
- [18] Hao F, Fang D. Mechanical deformation and fracture mode of polycrystalline graphene: Atomistic simulations. *Physics Letters A*. 2012;376(24-25):1942-7.
- [19] Novoselov KS, Geim AK, Morozov SV, Jiang D, Katsnelson MI, Grigorieva IV, et al. Two-dimensional gas of massless Dirac fermions in graphene. *Nature*. 2005;438(7065):197-200.
- [20] Warner JH, Margine ER, Mukai M, Robertson AW, Giustino F, Kirkland AI. Dislocation-Driven Deformations in Graphene. *Science*. 2012;337(6091):209-12.
- [21] Ovid'ko IA, Sheinerman AG. Cracks at disclinated grain boundaries in graphene. *Journal of Physics D-Applied Physics*. 2013;46(34):9.

- [22] Kotakoski J, Meyer JC. Mechanical properties of polycrystalline graphene based on a realistic atomistic model. *Physical Review B*. 2012;85(19).
- [23] Wang B, Puzyrev Y, Pantelides ST. Strain enhanced defect reactivity at grain boundaries in polycrystalline graphene. *Carbon*. 2011;49(12):3983-8.
- [24] Wu J, Wei Y. Grain misorientation and grain-boundary rotation dependent mechanical properties in polycrystalline graphene *Journal of the Mechanics and Physics of Solids* 2013.
- [25] Song ZG, Artyukhov VI, Yakobson BI, Xu ZP. Pseudo Hall-Petch Strength Reduction in Polycrystalline Graphene. *Nano Letters*. 2013;13(4):1829-33.
- [26] Kim K, Artyukhov VI, Regan W, Liu YY, Crommie MF, Yakobson BI, et al. Ripping Graphene: Preferred Directions. *Nano Letters*. 2012;12(1):293-7.
- [27] Zhang J, Zhao J, Lu J. Intrinsic Strength and Failure Behaviors of Graphene Grain Boundaries. *Acs Nano*. 2012;6(3):2704-11.
- [28] Zhang JF, Zhao JJ. Structures and electronic properties of symmetric and nonsymmetric graphene grain boundaries. *Carbon*. 2013;55:151-9.
- [29] Banhart F, Kotakoski J, Krasheninnikov AV. Structural Defects in Graphene. *Acs Nano*. 2011;5(1):26-41.
- [30] Mortazavi B, Ahzi S. Thermal conductivity and tensile response of defective graphene: A molecular dynamics study. *Carbon*. 2013;63:460-70.
- [31] Carpenter C, Maroudas D, Ramasubramaniam A. Mechanical properties of irradiated single-layer graphene. *Applied Physics Letters*. 2013;103(1):4.
- [32] Zhu J, He M, Qiu F. Effect of Vacancy Defects on the Young's Modulus and Fracture Strength of Graphene: A Molecular Dynamics Study. *Chinese Journal of Chemistry*. 2012;30(7):1399-404.
- [33] Zhang T, Li X, Kadkhodaei S, Gao H. Flaw Insensitive Fracture in Nanocrystalline Graphene. *Nano Letters* 2012, p. 4605-10.
- [34] Sha ZD, Pei QX, Liu ZS, Shenoy VB, Zhang YW. Is the failure of large-area polycrystalline graphene notch sensitive or insensitive? *Carbon*. 2014;72:200-6.
- [35] Zhang H, Duan Z, Zhang XN, Liu C, Zhang JF, Zhao JJ. Strength and fracture behavior of graphene grain boundaries: effects of temperature, inflection, and symmetry from molecular dynamics. *Physical Chemistry Chemical Physics*. 2013;15(28):11794-9.
- [36] Sun YJ, Ma F, Ma DY, Xu KW, Chu PK. Stress-induced annihilation of Stone-Wales defects in graphene nanoribbons. *Journal of Physics D-Applied Physics*. 2012;45(30):5.
- [37] Bonilla LL, Carpio A. Driving Dislocations in Graphene. *Science*. 2012;337(6091):161-2.
- [38] Zhang P, Ma L, Fan F, Zeng Z, Peng C, Loya PE, et al. Fracture toughness of graphene. *Nature Communications* 2014.
- [39] Liu T-H. Effects of dislocation densities and distributions on graphene grain boundary failure strengths from atomistic simulations. *Carbon* 2012.
- [40] Yazyev OV. Polycrystalline graphene: Atomic structure, energetics and transport properties. *Solid State Communications*. 2012;152(15):1431-6.
- [41] Liu TH, Gajewski G, Pao CW, Chang CC. Structure, energy, and structural transformations of graphene grain boundaries from atomistic simulations. *Carbon*. 2011;49(7):2306-17.
- [42] Pei QX, Zhang YW, Shenoy VB. A molecular dynamics study of the mechanical properties of hydrogen functionalized graphene. *Carbon*. 2010;48(3):898-904.
- [43] Jhon YI. The mechanical responses of tilted and non-tilted grain boundaries in graphene. *Carbon* 2012.
- [44] Han J, Ryu S, Sohn D, Im S. Mechanical strength characteristics of asymmetric tilt grain boundaries in graphene. *Carbon*. 2014;68:250-7.

- [45] Li JCM. DISCLINATION MODEL OF HIGH ANGLE GRAIN-BOUNDARIES. *Surface Science*. 1972;31(1):12-&.
- [46] Cao AJ, Qu JM. Atomistic simulation study of brittle failure in nanocrystalline graphene under uniaxial tension. *Applied Physics Letters*. 2013;102(7):5.
- [47] Mortazavi B, Cuniberti G. Atomistic modeling of mechanical properties of polycrystalline graphene. *Nanotechnology*. 2014;25(21):8.
- [48] Seol JH, Jo I, Moore AL, Lindsay L, Aitken ZH, Pettes MT, et al. Two-Dimensional Phonon Transport in Supported Graphene. *Science*. 2010;328(5975):213-6.
- [49] Xu ZP, Buehler MJ. Nanoengineering Heat Transfer Performance at Carbon Nanotube Interfaces. *ACS Nano*. 2009;3(9):2767-75.
- [50] Ng TY, Yeo JJ, Liu ZS. A molecular dynamics study of the thermal conductivity of graphene nanoribbons containing dispersed Stone-Thrower-Wales defects. *Carbon*. 2012;50(13):4887-93.
- [51] Bagri A, Kim SP, Ruoff RS, Shenoy VB. Thermal transport across Twin Grain Boundaries in Polycrystalline Graphene from Nonequilibrium Molecular Dynamics Simulations. *Nano Letters*. 2011;11(9):3917-21.
- [52] Wang Y, Song Z, Xu Z. Characterizing thermal conduction in polycrystalline graphene. August 29, 2013.
- [53] Yang D, Ma F, Sun YJ, Hu TW, Xu KW. Influence of typical defects on thermal conductivity of graphene nanoribbons: An equilibrium molecular dynamics simulation. *Applied Surface Science*. 2012;258(24):9926-31.
- [54] Cao A. Molecular dynamics simulation study on heat transport in monolayer graphene sheet with various geometries. *Journal of Applied Physics*. 2012;111(8):9.
- [55] Park M, Lee SC, Kim YS. Length-dependent lattice thermal conductivity of graphene and its macroscopic limit. *Journal of Applied Physics*. 2013;114(5):5.
- [56] Chen J, Zhang G, Li BW. Substrate coupling suppresses size dependence of thermal conductivity in supported graphene. *Nanoscale*. 2013;5(2):532-6.
- [57] Yu CX, Zhang G. Impacts of length and geometry deformation on thermal conductivity of graphene nanoribbons. *Journal of Applied Physics*. 2013;113(4):4.
- [58] Zhang JC, Wang XW. Thermal transport in bent graphene nanoribbons. *Nanoscale*. 2013;5(2):734-43.
- [59] Yu CX, Zhang G. The underestimated thermal conductivity of graphene in thermal-bridge measurement: A computational study. *Journal of Applied Physics*. 2013;113(21):4.
- [60] Serov AY, Ong ZY, Pop E. Effect of grain boundaries on thermal transport in graphene. *Applied Physics Letters*. 2013;102(3):5.
- [61] Lindsay L, Broido DA, Mingo N. Flexural phonons and thermal transport in graphene. *Physical Review B*. 2010;82(11):6.
- [62] Thomas JA, Turney JE, Iutzi RM, Amon CH, McGaughey AJH. Predicting phonon dispersion relations and lifetimes from the spectral energy density. *Physical Review B*. 2010;81(8):4.
- [63] Liu TH, Pao CW, Chang CC. Thermal response of grain boundaries in graphene sheets under shear strain from atomistic simulations. *Computational Materials Science*. 2013;70:163-70.
- [64] Ikeshoji T, Hafskjold B. NONEQUILIBRIUM MOLECULAR-DYNAMICS CALCULATION OF HEAT-CONDUCTION IN LIQUID AND THROUGH LIQUID-GAS INTERFACE. *Molecular Physics*. 1994;81(2):251-61.
- [65] Lindsay L, Broido DA. Optimized Tersoff and Brenner empirical potential parameters for lattice dynamics and phonon thermal transport in carbon nanotubes and graphene. *Physical Review B*. 2010;81(20):6.
- [66] Wang P, Gong B, Feng Q, Wang HT. Simulations of thermal conductance across tilt grain boundaries in graphene. *Acta Mechanica Sinica*. 2012;28(6):1528-31.

- [67] Ng TY, Yeo JLL, Z.S. A molecular dynamics study of the thermal conductivity of graphene nanoribbons containing dispersed Stone–Thrower–Wales defects. *Carbon* 2012.
- [68] Tang SJ, Kulkarni Y. The interplay between strain and size effects on the thermal conductance of grain boundaries in graphene. *Applied Physics Letters*. 2013;103(21):4.
- [69] Liu TH, Lee SC, Pao CW, Chang CC. Anomalous thermal transport along the grain boundaries of bicrystalline graphene nanoribbons from atomistic simulations. *Carbon*. 2014;73:432-42.